

Rowan University

Rowan Digital Works

Theses and Dissertations

11-14-2022

INVESTIGATION OF FLEXIBLE AND WEARABLE DEVICES FOR THE ANALYSIS OF BIOLOGICAL SIGNALS

Muhammad Usman
Rowan University

Follow this and additional works at: <https://rdw.rowan.edu/etd>



Part of the [Biomedical Engineering and Bioengineering Commons](#)

Recommended Citation

Usman, Muhammad, "INVESTIGATION OF FLEXIBLE AND WEARABLE DEVICES FOR THE ANALYSIS OF BIOLOGICAL SIGNALS" (2022). *Theses and Dissertations*. 3071.
<https://rdw.rowan.edu/etd/3071>

This Dissertation is brought to you for free and open access by Rowan Digital Works. It has been accepted for inclusion in Theses and Dissertations by an authorized administrator of Rowan Digital Works. For more information, please contact graduateresearch@rowan.edu.

**INVESTIGATION OF FLEXIBLE AND WEARABLE DEVICES FOR THE
ANALYSIS OF BIOLOGICAL SIGNALS**

by

Muhammad Usman

A Dissertation

Submitted to the
Department of Mechanical Engineering
College of Engineering
In partial fulfillment of the requirement
For the degree of
Doctor of Philosophy
at
Rowan University
September 16, 2022

Dissertation Chair: Wei Xue, Ph.D., Associate Professor, Department of Mechanical
Engineering

Committee Members:

Adarsh K. Gupta, DO., Professor, School of Osteopathic Medicine
Behrad Koohbor, Ph.D., Assistant Professor, Department of Mechanical Engineering
Jeffrey Hettinger, Ph.D., Professor, Department of Physics and Astronomy
Rizwan Ghaffar, Ph.D., Principal Engineer, Broadcom Inc.

© 2022 Muhammad Usman

Dedications

I want to thank my parents Muhammad Anwar and Khalida Anwar for always giving me strength to achieve my goals. I would also like to thank my sister Rosheen Anwar for always being there for me.

Acknowledgments

I want to express thanks and gratitude to my advisor Dr. Wei Xue for the tremendous encouragement and guidance and for providing me the opportunity to gain more experience through research. I would also like to thank my research committee members, Dr. Adarsh Gupta, Dr. Jeffrey Hettinger, Dr. Behrad Koohbor, and Dr. Rizwan Ghaffar, for supporting and assisting me.

Abstract

Muhammad Usman
INVESTIGATION OF FLEXIBLE AND WEARABLE DEVICES FOR THE
ANALYSIS OF BIOLOGICAL SIGNALS
2021-2022
Wei Xue, Ph.D.
Doctor of Philosophy

The application potential for flexible and wearable electronics in the field of healthcare has received great interest in recent years. Flexible and wearable devices based on soft, biocompatible materials can be comfortably attached to the human skin for continuous health monitoring. In this work, we present two novel wearable bioelectrical impedance analysis (BIA) systems for body composition measurement. First, we developed a wearable ring-based BIA system for body fat monitoring. The wearable ring contains flexible copper electrodes to interface with the human body. The device is tested on 40 healthy volunteers and the results demonstrate a high correlation with an off-the-shelf body fat monitor. Second, we developed flexible BIA systems on paper and plastic substrates and compared their performance. The paper-based system demonstrates stronger adhesive contact with the electronic components while the plastic-based system provides lower power consumption and lower electrode impedance. Last, we proposed a novel temperature sensor on a polydimethylsiloxane (PDMS) substrate that can compensate for the deformation-induced resistance variation and measure temperature with minimum errors. The compensation method enhances the competence of flexible temperature sensors and increases their potential for applications in wearable electronics.

Table of Contents

Abstract	v
List of Figures	viii
List of Tables	xi
Chapter I: Introduction.....	1
1.1 Flexible Electronics Challenges and Opportunities	1
1.1.1 Introduction.....	1
1.1.2 Flexible Substrates	3
1.1.3 Interconnects for Flexible Electronics	5
1.1.4 Fabrication Methodologies	10
1.1.5 Applications in Bioelectronics	13
1.2 Bioelectrical Impedance Analysis (BIA)	14
1.2.1 Electrical Properties of Biological Tissues	14
1.2.2 Measurement and Analysis of Bioelectrical Impedance.....	17
1.2.3 Body Composition Estimation.....	21
1.2.4 Two-Electrode and Four-Electrode Measurement.....	23
1.2.5 State-of-the-Art Research and Commercial Devices	24
1.3 Research Motivation and Objectives.....	25
1.4 Overview of Dissertation	26
Chapter II: Wearable Ring BIA for Estimation and Monitoring of Body Fat	28
2.1 Introduction	28
2.2 System Architecture	30
2.2.1 Sensor Module	31
2.2.2 Controller Module.....	33
2.2.3 Smartphone Interfacing Application.....	35
2.3 Ring Design and Electrodes	35
2.4 Experimental Protocol.....	36
2.5 Results and Discussion.....	38
2.5.1 Hardware Verification	38
2.5.2 Electrode Characterization and Impedance Measurement.....	41

Table of Contents (Continued)

2.5.3	Body Fat Estimation and Equation Comparison.....	47
2.5.4	Conclusion	54
Chapter III: Flexible Bioimpedance Analyzer on Paper and Plastic Substrate		56
3.1	Introduction	56
3.2	System Architecture	57
3.3	Fabrication Procedure	59
3.4	Experimental Procedure	61
3.5	Results and Discussion.....	62
3.5.1	Mechanical Testing.....	62
3.5.2	Hardware Verification	65
3.5.3	Electrode Characterization.....	67
3.5.4	Bio-Impedance Measurement and Analysis	69
3.6	Conclusion.....	71
Chapter IV: Flexible Temperature Sensor with Compensation of Bending and Stretching		72
4.1	Introduction	72
4.2	Methodology	74
4.3	Sensor Fabrication.....	77
4.4	Hardware Architecture	79
4.5	Experiments, Results, and Discussion.....	83
4.5.1	Temperature Quantification while Bending the Sensor.....	83
4.5.2	Temperature Quantification while Stretching the Sensor.....	91
4.6	Physical State Determination	96
4.7	Conclusion.....	102
Chapter V: Conclusions and Future Work.....		103
5.1	Conclusions	103
5.2	Recommendations and Future Work.....	109
References.....		111

List of Figures

Figure	Page
Figure 1. Categories of Substrate Materials Used to Develop Flexible Electronics.....	4
Figure 2. Comparison of Materials Used to Develop Interconnects for Flexible Electronics.....	7
Figure 3. Interconnect Designs for Flexible Electronics	9
Figure 4. Fabricating Techniques Used to Deposit Electrically Conductive Materials onto Flexible Substrates	11
Figure 5. Cell Membrane Structure of the Biological Cell.....	15
Figure 6. Electrical Equivalent Model of the Biological Cell	16
Figure 7. Flow of Electrical Current at Low and High Frequency	18
Figure 8. Simplified 2R1C Electrical Model of the Biological Cell (Fricke's Model)	19
Figure 9. Schematic Diagram of Body Composition.....	22
Figure 10. Measurement Techniques for Bioelectrical Impedance	24
Figure 11. Simplified Block Diagram of the Designed Body Fat Analyzer.....	31
Figure 12. Complete System Architecture of the Designed Body Fat Analyzer	33
Figure 13. Photograph of the Sensor Module (left) and Controller Module (right) Interface	34
Figure 14. (a) Silicone Ring with Source (I+, I-) and Sense (V+, V-) Electrodes. (b) Wrist Wearable Hardware Enclosure and Ring Interface	36
Figure 15. Output Current (I_{out}) Against Load Resistance (R_L) for the Howland Current Source	39
Figure 16. Equivalent Electrical Model of the Human Body	40
Figure 17. Three-Electrode Measurement	42

List of Figures (Continued)

Figure	Page
Figure 18. Skin-Electrode Contact Impedance of Dry Copper Electrodes and Gel-Based Ag/AgCl Electrodes at 50 kHz.....	44
Figure 19. Four-Electrode Measurement	45
Figure 20. Linear Regression for Impedance Using Wet and Dry Electrodes.....	46
Figure 21. Body Fat Correlation Plot.....	51
Figure 22. Bland-Altman Plot.....	52
Figure 23. Simplified Block Diagram of Electrical Bio-Impedance Analyzer Interfacing with the Human Body.....	59
Figure 24. Flexible Printed Circuit Fabrication Procedure	60
Figure 25. Photograph of the Developed Bioimpedance Sensor Modules	61
Figure 26. Bio-Impedance Analysis Measurement.....	62
Figure 27. Cross-Sectional SEM-EDS Images of Silver Ink on (a) Paper (b) Plastic. Silver Sinks into Paper, Creating a Stronger Bond.....	64
Figure 28. (a) Resistance and (b) Reactance Plots Using the 2R1C Tissue Model for Hardware Calibration and Performance Evaluation	66
Figure 29. (a) Electrode-Skin Contact Impedance of Dry and Wet Electrodes. (b) Bio-Impedance Plot of One Subject Using all Three EBI Systems	68
Figure 30. Bio-Impedance Analysis of 12 Subjects at Selected Frequencies Using Paper and Plastic Sensor Module. (a) Resistance. (b) Reactance	70
Figure 31. Compensation Methodology	76
Figure 32. Fabrication Process of RTD Structures Using Stencil Printing and Silver Paste	78
Figure 33. Photograph of the Fabricated RTD Sensors	79

List of Figures (Continued)

Figure	Page
Figure 34. Block Diagram of the Designed Temperature Measurement System	81
Figure 35. Photographs of the Complete System.....	82
Figure 36. The Bending Experiment is Performed by Placing the Sensor on Cylinders with Varying Radii Ranging from 100 mm to 40 mm.....	85
Figure 37. Analysis of Changes in Resistance While Bending the Sensor.....	86
Figure 38. Sum of Change in Resistance of the Sensor Versus Temperature from 20°C to 40°C.....	88
Figure 39. Experimental Setup for Heating and Bending the Sensor	90
Figure 40. Analysis of Resistance Measurement Errors When the Sensor is Under Heating and Bending at the Same Time	91
Figure 41. Analysis of Resistance Changes While Stretching the Sensors	92
Figure 42. Subtraction of Change in Resistance of the Sensor Versus Temperature from 20°C to 40°C.....	94
Figure 43. Experimental Setup for Heating and Stretching the Sensor	95
Figure 44. Analysis of Resistance Measurement Errors when the Sensor is Under Heating and Stretching at the Same Time.....	96
Figure 45. Step-By-Step Analysis to Determine the Physical State of the Sensor, Apply the Necessary Compensation Technique, and Determine the Temperature Using the Sensor	101

List of Tables

Table	Page
Table 1. Anthropropic Measurement of the Study Group.....	37
Table 2. Performance Results	40
Table 3. Bioelectrical Impedance Analysis Equations for Fat-Free Mass (FFM) Estimation	49
Table 4. Comparison of the Designed Bioelectrical Impedance Analyzer with Similar Systems	53
Table 5. Comparison of the Designed RTD with Similar Systems	107

Chapter I

Introduction

1.1 Flexible Electronics Challenges and Opportunities

1.1.1 Introduction

The development of electronics on flexible substrates has recently received considerable attention as efforts in this area are ultimately expected to facilitate valuable device applications [1]. Although the concept of flexible electronics has been around for several decades, there has been a significant gap in performance, functionalities, and capabilities between flexible and conventional rigid electronics. The modern-day advancements in the development of novel materials and fabrication techniques have attracted great interest, as they allow for high-performance scalable electronic devices to be manufactured directly on flexible substrates [2]. Furthermore, the properties of some of the novel elastomer substrates have also been manipulated to extend beyond flexibility, and now include stretchability and healing ability [3, 4]. Similarly, biodegradability and biocompatibility have also been accomplished through polymers, which do not cause adverse effects to the body and can be decomposed into smaller constituent pieces after utilization [5]. These advancements are now enabling a new generation of electronic devices that can conform to dynamic and complex surfaces, such as those found in biological systems and bioinspired soft robotics [6].

Advancements in flexible electronics open the door for a wide range of exciting new applications such as wearable sensors, implantable electronics, conformable energy harvesting devices, and actuators that can extend the functionality of robots [7-10]. While conventional rigid electronics are already capable of these functions, flexible electronics

provide additional mechanical features to adapt to curved or irregular surfaces along with other benefits such as light weight, low cost, and being disposable [11]. Flexible devices must be able to undergo bending, folding, stretching, or twisting, and more importantly, they must be able to sustain the electronic performance and functions during the strain [12]. As the application range of flexible electronics is extremely broad, the strain conditions and flexibility requirements for each device can be very different. Extremely high strain is anticipated in sensing applications where the device is directly attached to skin, organs, or embedded in clothing or textile [13-15]; while for other applications, small but repetitive strain cycles are expected. In addition, some applications may only require moderate one-time strain. To quantify device performance under all these conditions, various techniques have been developed to evaluate the flexibility or strain tolerance, including cyclic bending test, cyclic stretching test, scratch test, and peel test. Each of these techniques reveals unique information about the mechanical reliability of the device and the material [16].

Although many advancements have been achieved and important innovations have been reported, the field of flexible electronics still faces many challenges before it can become a part of our daily life. Solving these challenges will need creative designs and extensive investigations, which present great opportunities for scientific research and development (R&D) to rapidly advance in this area. The upcoming sections explain the procedures and materials used for the development of flexible electronics. Detailed descriptions and explanations are provided regarding different categories of materials used as flexible substrates and those used to develop interconnects between spaced-out

components. Furthermore, major fabrication methodologies have been highlighted. Finally, the applications of flexible electronics in bioelectronics have been summarized.

1.1.2 Flexible Substrates

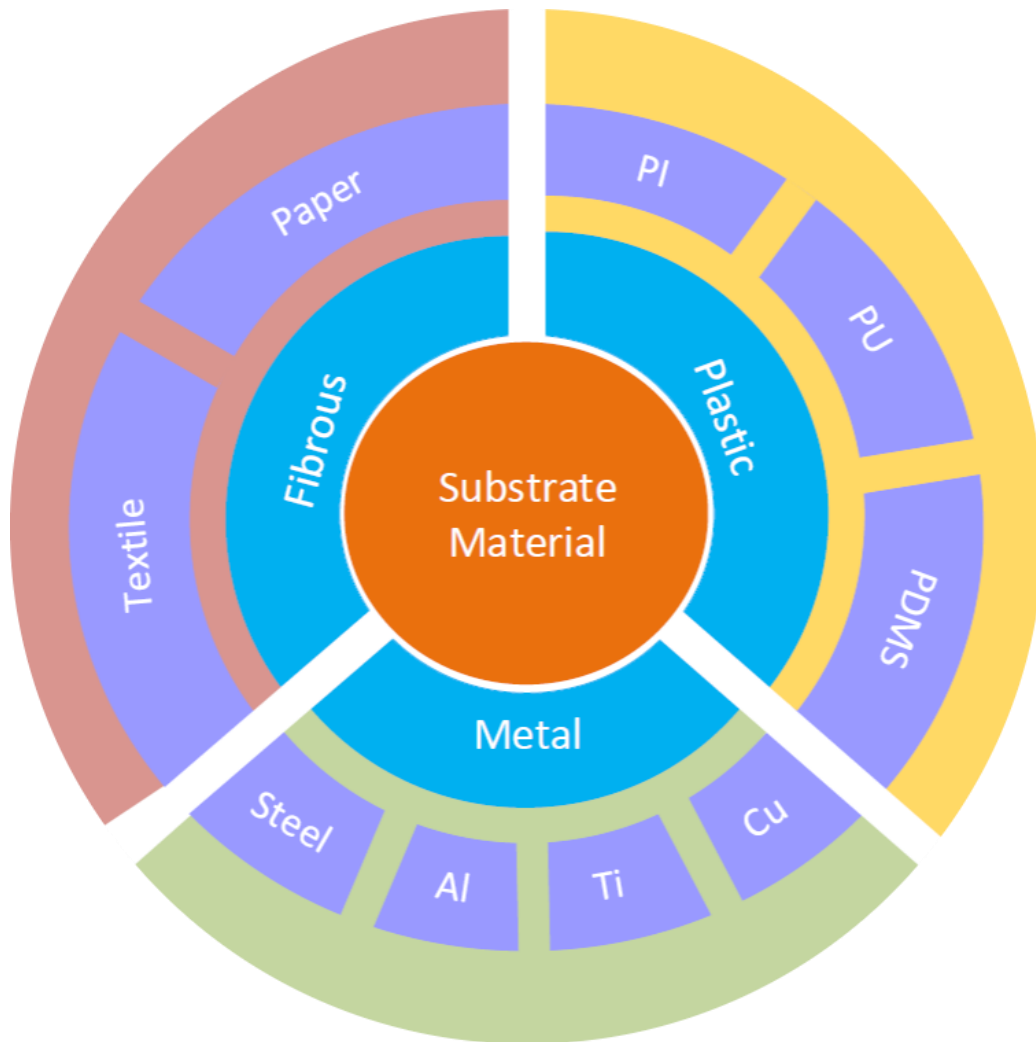
The selection of substrates is critical when designing flexible electronic devices, as the mechanical properties of the substrate tend to dominate the tolerance range of the overall device. Generally, the flexible substrate materials can be divided into three main categories: plastic materials, metal foils, and fibrous materials, as shown in Fig. 1.

Plastic films are the most common substrates used to fabricate flexible electronics due to their optical clarity, smooth surface, solvent resistance, and high mechanical and thermal stability [17-20]. The key materials used in plastic films include polyimide (PI) [21, 22], polyethylene terephthalate (PET) [23], and polyurethane (PU) [24]. In applications where stretchability is required, the most commonly used substrate is polydimethylsiloxane (PDMS), which is a highly compliant elastomer with excellent stretchability properties. PDMS has a Young's modulus of 3.7 MPa and can be stretched for more than 200% [25, 26].

Metal foil-based substrates are used when high-temperature processing is a requirement. Comparing to plastics, metals are temperature resistant and possess excellent thermal and electrical conductivity. Furthermore, metals are also a good barrier against humidity [17]. The commonly used metal substrates are stainless steel, titanium, aluminum, and copper foils [17, 27-30]. The main disadvantages of the metal foils are their high weight and high cost, making them ill-suited for high-volume manufacturing.

Figure 1

Categories of Substrate Materials Used to Develop Flexible Electronics



Note. Clockwise from top right: polyimide [21, 22], polyurethane (PU) [24], polydimethylsiloxane (PDMS) [25, 26], copper, titanium, aluminum, stainless steel [17, 27-30], textile (cotton, polyester, nylon, kevlar) [31], and paper [32, 33].

More recently, many researchers have started using paper as another substrate material for flexible electronics, because paper is eco-friendly and has an extremely low

cost [32, 33], e.g., paper costs about $\$0.1/\text{m}^2$ while commodity plastic costs $\sim\$2/\text{m}^2$. The main drawback of paper is that its fibrous structure tends to absorb moisture which may affect the electronic components both chemically and mechanically. Another fibrous substrate material that is being used in wearable electronics is textile [31]. Textile substrates enable devices to be embedded into clothing or textile-based network [34]. Economically, textile substrates are important as the market for electronic-integrated clothing is ultimately expected to grow significantly. However, there are numerous challenges when using textiles for flexible electronic applications. For example, textile is composed of numerous individual fibers which make the fabrication of surface-mount devices difficult. Textile is also capable of absorbing a large quantity of water that can affect the electronic components. Clothing must be washable, and therefore, the integrated components inside textiles should be sufficiently compliant such that they survive against water and mechanical deformation [35].

1.1.3 Interconnects for Flexible Electronics

Electrically conductive materials are needed as interconnects in flexible electronics. Nanomaterials of metals or carbon, conductive polymers, and polymer-nanomaterial composites can be used to create interconnects. A comparison of these materials is provided in Fig. 2.

Metals are among the most electrically conductive materials due to their high density of free electrons [36]. Metal nanoparticle-based inks have been used to create interconnects on flexible substrates, and the resulting patterns are more flexible and stretchable than conventionally fabricated solid conductors [37]. These metal inks can also reduce the weight, volume, and cost of the electronic device. Thin films of metal

nanoparticles can be created by easy, inexpensive, solution-based deposition techniques such as inkjet printing, spray printing, and spin coating [11]. The selection of materials is based on applications and fluid properties such as viscosity, density, and surface tension. Among all the material options, silver nanomaterials are arguably the most widely studied material due to their good stability and high electrical conductivity [38]. The selection of nickel ink is challenging as it is lower in price than silver and has good conductivity [11], but nickel [39] and copper [40] tend to oxidize even under regular ambient conditions, which can reduce their lifespan. Gold nanoparticles can also be used as they are stable and have excellent conductivity. However, they are expensive and using them can increase the cost of production significantly [41]. Overall, metal nanoparticles are highly conductive and can be produced in large quantities. However, they are prone to clustering, and the clustered particles can clog the nozzle of the printer [42]. There are organometallic inks that can eliminate the issue of nozzle clogging due to the surface functionalization of nanoparticles. The organometallic inks are available for gold, silver, nickel, copper, and platinum. Among them, the organometallic silver-based inks are preferred due to their lower resistivity of 2-3 $\mu\Omega\text{cm}$ in comparison to the others [11].

Carbon-based nanomaterials can also be used to develop sensors and interconnects on flexible substrates. Carbon nanotubes (CNTs) are electrically conductive and provide high sensitivity and fast response when used as sensors [43]. The main problem with CNTs is the dispersion process using inkjet printing. CNTs have strong van der Waals forces and large surface areas resulting in clumping, which potentially lead to clogging of the nozzle of the print head [44]. A stable CNT dispersion of inkjet printing

can be achieved using organic solvents or dispersants of water-based inks. However, water-based inks can cause high surface tension which can lead to inconsistent printing. This problem can be solved by using surfactants [45].

Another type of materials that can be used to develop flexible interconnects is conductive polymers due to their unique electrical, optical, and physical properties. Conductive polymers such as polyaniline (PANI) are flexible, wearable, and potentially washable. Furthermore, they are more resistive against fatigue failures as compared to metals. The electrical conductivity of polymers, however, is typically orders of magnitude lower than that of metals [46]. Conductive polymers possess a conjugated pi-electron system which gives them their conducting properties [47]. Polypyrrole (PPy) and PANI are common conductive materials that have been widely used in inkjet printing [47].

Figure 2

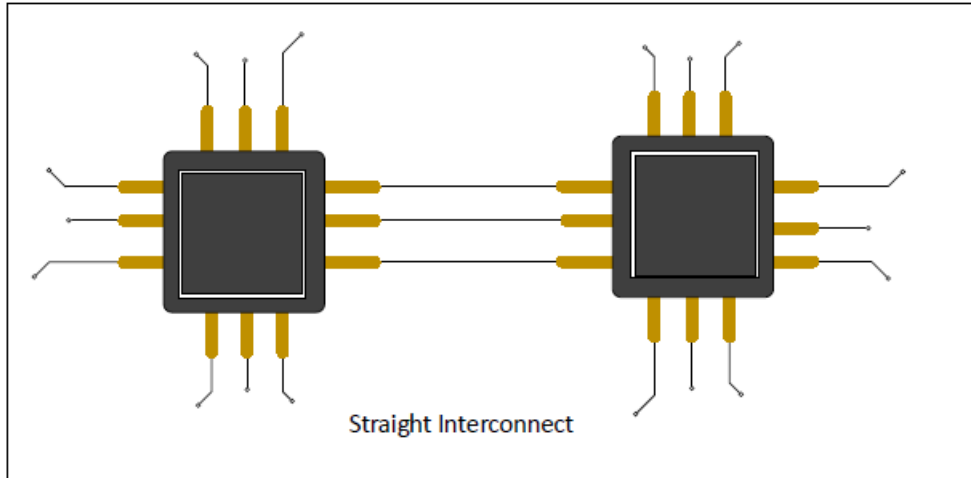
Comparison of Materials Used to Develop Interconnects for Flexible Electronics

Material	Conductivity	Flexibility	Price	Light Weight
Metal	● ● ●	● ○ ○	\$\$\$	● ○ ○
Carbon	● ● ○	● ● ○	\$\$	● ● ○
Polymer	● ○ ○	● ● ●	\$	● ● ●
Polymer Composite	● ● ○	● ● ●	\$\$	● ● ○

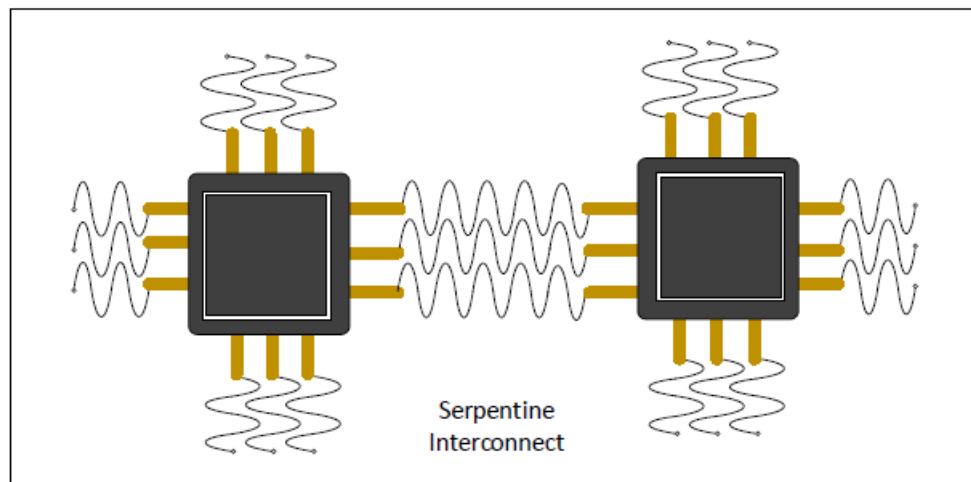
Fig.3. shows different types of interconnect designs that have been used to develop flexible electronics. The most common design for interconnects in electronics is straight lines since they provide the most efficient paths for current flow and impose the least amount of resistance, as shown in Fig. 3a. Straight line interconnects can also be used in designing flexible electronic devices as they provide good electrical and mechanical reliability under small stresses and strains [48-50]. However, in the application where a large strain of substrate is required, the conductive interconnects can fracture and fail. To combat the strain limitation, various geometrical designs have been proposed for making reliable, conductive interconnects on a wide range of materials. The most common design is the serpentine structure (Fig. 3b) which has received a significant amount of interest because it can deform to accommodate large tensile strains [51]. As a result, the stretchability of the serpentine structure is higher than that of straight line conductors. Beyond the 2-dimensional (2D) planar structures, 3-dimensional (3D) bridge designs (Fig. 3c) for the interconnects can provide further increased stretchability [52]. The bridges can move up or down to accommodate the mechanical deformation of the substrate when it is compressed or stretched. These bridges can also be twisted and sheared in ways that can withstand a more complex distribution of stress. However, such structures require complex and expensive fabrication techniques.

Figure 3

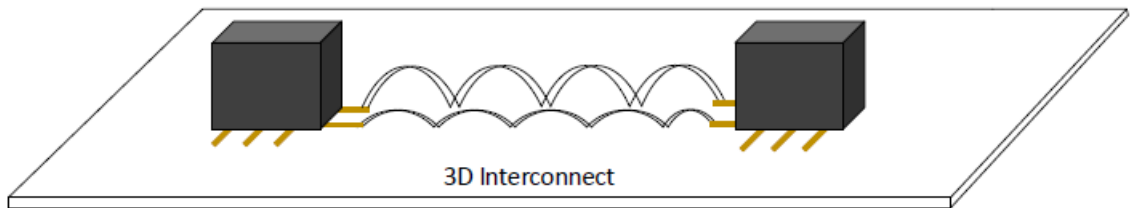
Interconnect Designs for Flexible Electronics



(a)



(b)



(c)

Note. Types of designs to develop interconnects for flexible electronics: (a) straight lines, (b) serpentine, and (c) 3D arc bridges.

1.1.4 Fabrication Methodologies

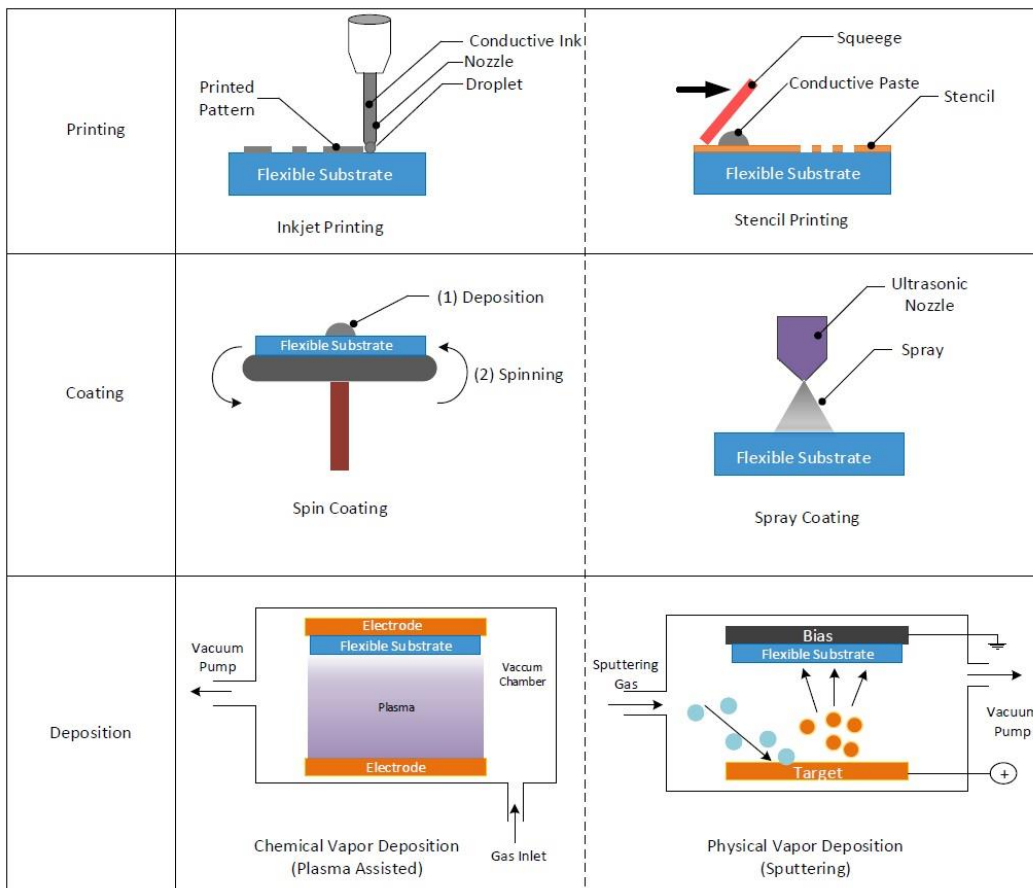
In order to produce flexible devices efficiently, fabrication techniques are required to be inexpensive, easy to use, and readily accessible. While conventional rigid electronic devices are fabricated through methodologies including photolithography, etching, and film deposition, flexible electronics is usually developed through printing, coating, and deposition techniques, as shown in Fig. 4.

Printing technology has recently gained much attention due to its low cost and easy-to-implement principles. It applies conductive inks or pastes onto flexible substrates in a controlled manner [53]. Common printing techniques include inkjet [54], gravure [55], and screen/stencil printing [56, 57]. The inkjet printing uses an inkjet nozzle head, which creates micrometer-sized patterns, to deposit a precise amount of droplets of conductive inks on a substrate [58]. This is a fast, inexpensive, and non-impact method to create small patterns. The droplet formation can be adjusted by surface tension and viscosity of the inks. Furthermore, the particle size of the ink needs to be less than 1 μm to avoid clogging the small channel nozzle [59]. Another technique used to print conductive inks on flexible substrates is gravure printing in which an ink is transferred through small, engraved cavities in the engraving cylinder. The major obstacle encountered by gravure printing is the high resolution of the print line which is typically less than 20 μm [60]. Furthermore, this technology is not able to produce uniform pattern lines with sharp edges which restricts the manufacturing of top layers on electronic devices. Finally, the most popular technique to print conductive features on flexible substrates is screen printing or stencil printing. This technology adds speed, simplicity, low cost, and adaptability to the manufacturing process. The main drawback with this

technology is that the printable ink should have a high viscosity. Conductive materials are mixed with additives to provide high viscosity to the ink; however, the presence of these additives can decrease the conductivity of the ink. Furthermore, the low resolution of the pre-made stencil/screen can limit the printing capabilities of small patterns and thin structures [58, 61, 62].

Figure 4

Fabricating Techniques Used to Deposit Electrically Conductive Materials onto Flexible Substrates



Coating and deposition techniques have been used to develop flexible and stretchable devices based on nanomaterials. Some of the leading techniques include spin coating, spray coating, drop casting, and dip coating [63]. In spin coating, the solution is spread on a rotating base and a thin film is formed after the solvent is evaporated [64]. The thickness of the deposited layer can be controlled by the speed of rotation and the concentration/viscosity of the solution. Spin coating is frequently used to deposit biomaterials, nanoparticles dispersions, and polymers. In spray coating, droplets are sprayed on the substrate using an ultrasonic nozzle [63, 65]. The substrate is rotated slowly while the nozzle passes through the substrate. The slow speed of the substrate reduces the centrifugal forces to a minimum. This method is well suited for sidewall coverage of micro and nanostructures on the substrate with a high aspect ratio. In drop casting, droplets are placed on the surface followed by controlled evaporation of the solvent [63, 66]. The thickness of the film can be varied by the concentration of the solution. However, this method does not always produce uniform films, therefore, its applications are relatively limited. In dip coating, the substrate is first dipped in a solution and then withdrawn at a fixed speed to produce a uniform layer [63]. The dip coating method has advantages over drop casting for higher film uniformity and process controllability [67].

Furthermore, common deposition techniques include chemical vapor deposition (CVD) and physical vapor deposition (PVD). CVD is a process in which a thin film is deposited on a substrate through controlled chemical reactions in a gas chamber at a high temperature [68]. CVD can be used to deposit metals, insulating films, and semiconductors. PVD is a vaporization coating technique in which material is converted

from the condensed phase to the vapor phase and then back to the condensed phase as a thin film [69]. The patterning is done by masking or lithography after the thin film deposition. In microelectronic and nanoelectronics devices, the electrical conductors are commonly deposited using the PVD process.

Textile electronics have different kinds of fabrication techniques which include braiding, weaving, and knitting using conductive fibers, wires, and yarns [70, 71]. The knitting technology is widely used to develop wearable devices due to the easy preparation process and the precise placement of direct contact devices. Yarn encapsulation technology is used to develop wearable sensors by attaching fine metal wires to a small sensor. In order to increase the mechanical strength, the encapsulated sensors and wires are often integrated within the carrier fibers [72, 73].

1.1.5 Applications in Bioelectronics

Flexible biomedical electronic devices have the potential to integrate with the human body seamlessly and maintain their stability and robustness under various strain conditions. These wearable devices can measure a variety of physiological signals noninvasively, such as heartbeats [74, 75], brain activities [76, 77], and muscle activities [78, 79]. The devices can measure these signals in real-time, providing updates to users and physicians about the health status. In recent years, flexible and wearable electronic devices have been extensively studied. In particular, they have made great progress as artificial electronic skin to closely mimic real interactions with the surrounding environment and resemble biological human skin [80]. The skin sensation functionalities include tactile sensing [81], strain sensing, as well as body temperature and humidity sensing [82]. Further research in this area could pave the way for novel soft robotics with

improved performance and functionalities [83, 84]. Flexible and stretchable electronic devices have also been developed for therapy and drug delivery platforms [85, 86]. Such medical devices can release the medicine once the system is triggered by an impulse, e.g., after a specific enzyme is detected or a preset level of strain is reached. The main purpose of these medical devices is to release the drug in a more controlled and efficient manner such that the patient receives an adequate dose [87].

Although much research has been done in flexible bioelectronics, the field is still new with many application areas requiring more extensive, in-depth studies. One such application area is bioelectrical impedance analysis (BIA), which is a method to estimate the composition of the human body. Developing flexible BIA devices face many challenges. The major obstacle is designing flexible dry electrodes and interfacing them with the human body to measure electrical signals accurately. Other challenges include biocompatibility, comfort level, and stable electronic behavior when the flexible device is under mechanical strain. The following section provides more details about the BIA methodology, research, and development.

1.2 Bioelectrical Impedance Analysis (BIA)

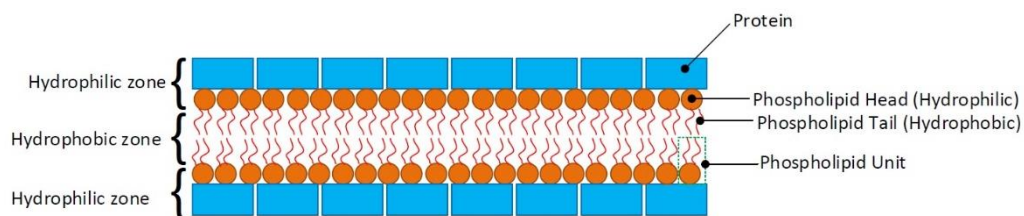
1.2.1 Electrical Properties of Biological Tissues

The human body is composed of various types of tissues, which are made of trillions of cells, with specific functions and structures, arranged in a complex 3D array [88]. These cells, made of intracellular fluid (ICF) and cell membrane (C_m), are suspended in an extracellular fluid (ECF) [89-91]. The ICF, ECF, and C_m are made of different materials that have distinctive electrical properties. When exposed to an alternating (AC) electric current, these three components respond differently due to their

distinctive physical, structural, and electrical properties. The intracellular fluids are composed of two constituents: nucleus and cytoplasm. The nucleus and cytoplasm are mostly made of a solution of salt, water, proteins, and different chemicals [92]. These materials are electrically conductive. Similarly, the extracellular fluids are also composed of electrically conductive materials. As a result, both ICF and ECF provide low resistive paths to the applied electrical signal [89-91]. By comparison, the membrane of the cells is composed of a unique layered structure. It contains a hydrophobic lipid bilayer that is sandwiched between two hydrophilic protein layers, as shown in Fig. 5 [93].

Figure 5

Cell Membrane Structure of the Biological Cell



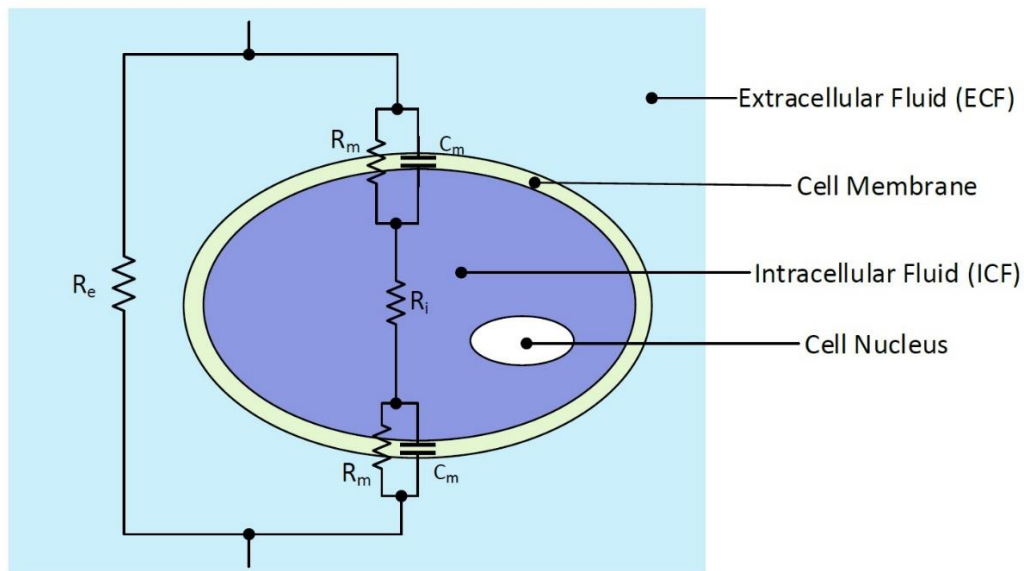
Note. Lipid bilayer having hydrophilic head and hydrophobic tail sandwiched between hydrophilic protein layers.

The hydrophobic lipid bilayer is electrically nonconductive, while the hydrophobic protein layers are electrically conductive. This structure of the membrane provides a capacitive response to the applied electrical current. Their combined responses to the alternating electrical current produce a complex electrical impedance called

bioelectrical impedance [89]. The complex bioelectrical impedance consists of two parts: a resistance (R) caused by the ICF/ECF and a negative reactance ($-X_c$) caused by the capacitive behavior of cell membranes [94]. Fig. 6 shows the electrical equivalent model of the biological cell where R_e is the extracellular fluid resistance, R_i is the intracellular fluid resistance, R_m is the trans-membrane ionic channel resistance, and C_m represents the cell membrane capacitance. The complex bioimpedance is different for each tissue and also varies with the change in the health status of the tissue. Therefore, the analysis of the complex bioimpedance can provide information regarding the anatomy and physiological status of the human body.

Figure 6

Electrical Equivalent Model of the Biological Cell



Note. R_e is the extracellular fluid resistance, R_i is the intracellular fluid resistance, R_m is

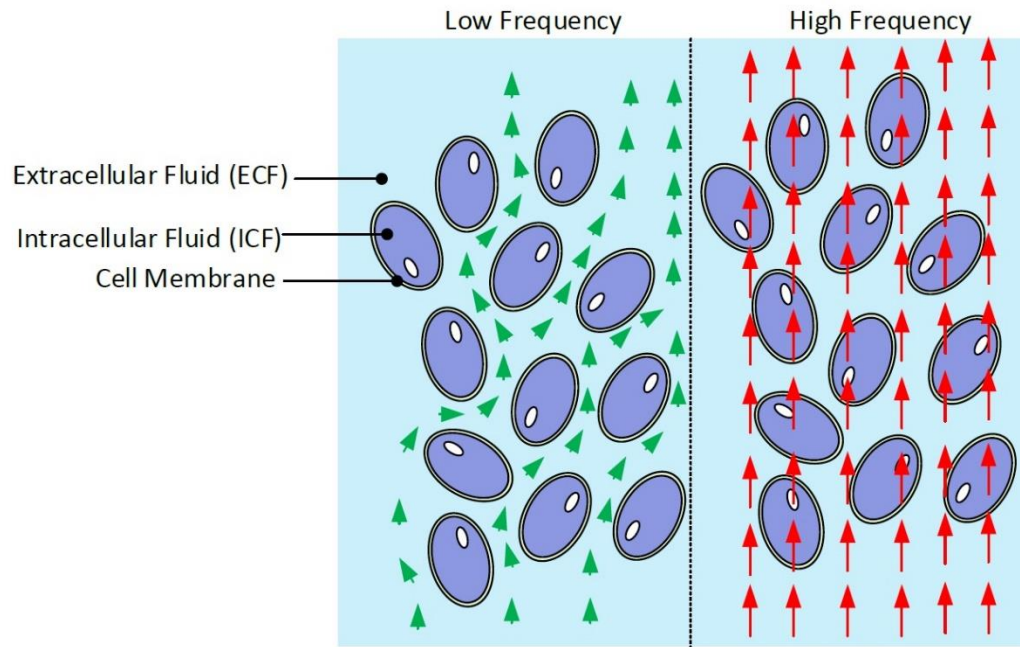
the trans-membrane ionic channel resistance, and C_m represents the cell membrane capacitance.

1.2.2 Measurement and Analysis of Bioelectrical Impedance

BIA is a widely used noninvasive, safe, and fast method to determine the complex electrical impedance of the human body and utilize that information to estimate the body composition [95]. It is an easy-to-conduct process that can be used to estimate fat-free mass, fat mass, and body water [96]. The process provides excellent consistency for repeated measurements. BIA can also be used to monitor the dynamics of the biological tissue. The bioelectrical impedance depends on the frequency of the applied signal and the composition of the tissues. Therefore, the overall response of the biological tissue to an applied AC signal produces a complex bioelectrical impedance which is a function of the composition, structure, and health status of the tissue as well as the frequency of the applied electrical signal [97, 98]. Fig. 7 shows the flow of electrical current through the body at low and high frequencies. When an AC signal of low frequency is applied, the impedance of the membrane is very high; as a result, only a small amount of electrical current flows through the cells, while most of the current flows through the extracellular fluids [93, 99]. Therefore, the overall impedance can be represented by R_e . At higher frequencies, the capacitive impedance of the cell membrane is reduced and the electrical current starts flowing through the intracellular as well as the extracellular fluids [93, 99].

Figure 7

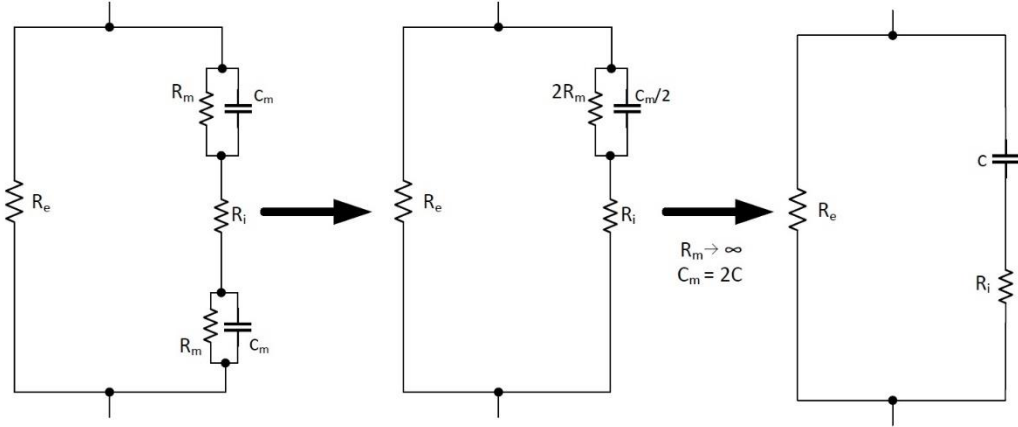
Flow of Electrical Current at Low and High Frequency



The equivalent electrical circuit model of the tissue can be represented as the capacitor C_m in series with the resistor R_i , and the combined C_m/R_i circuit is in parallel with the resistor R_e , as shown in Fig. 8. This simplified 2R1C model is also known as Fricke's model [100].

Figure 8

Simplified 2R1C Electrical Model of the Biological Cell (Fricke's Model)



Note. The simplified circuit representation of the biological cell. R_i is the intracellular fluid that is in series with the equivalent membrane capacitance C . R_e represents the extracellular fluid.

The bioelectrical impedance (Z) is measured by injecting a small amount of known alternating electrical current into the human body ($I_b \leq 1\text{mA}$, generally 50 kHz), and the voltage signal is measured across the body (V_b). The current injection and voltage measurement are performed by using an electrode interface. The magnitude of the impedance $|Z_b|$ is determined by dividing the measured voltage signal by the applied current signal (Ohm's law).

$$|Z| = \frac{V_b}{I_b} \quad (1)$$

The bioelectrical impedance is a complex quantity; therefore, it will have a phase angle difference between the applied and the measured signals depending on the tissue properties. As a result, the overall complex bioimpedance is represented as [101]:

$$Z = |Z|e^{j\theta} \quad (2)$$

where $|Z|$ represents the magnitude of the impedance while θ is the phase difference between the injected and measured signals. The complex impedance, in a Cartesian form, can be written as:

$$Z = R - jX_c \quad (3)$$

where R represents the resistance caused by the fluids (ICF and ECF) and $-X_c$ is the negative reactance imposed by the cell membranes. The relationship of $|Z|$, R , X_c , and θ can be expressed as:

$$|Z| = \sqrt{R^2 + X_c^2} \quad (4)$$

$$\theta = \tan^{-1}\left(-\frac{X_c}{R}\right) \quad (5)$$

BIA can be performed by using single as well as multiple frequencies depending on the application [102]. In single frequency (SF) BIA, an AC signal with a frequency of 50 kHz is applied and the impedance is measured. This frequency of 50 kHz is considered as the most optimum value to determine the fat-free mass (FFM) and total body water (TBW) [102-104] of the biological system. However, SF BIA cannot be used to determine the difference between ICF and ECF. By comparison, in multi-frequency

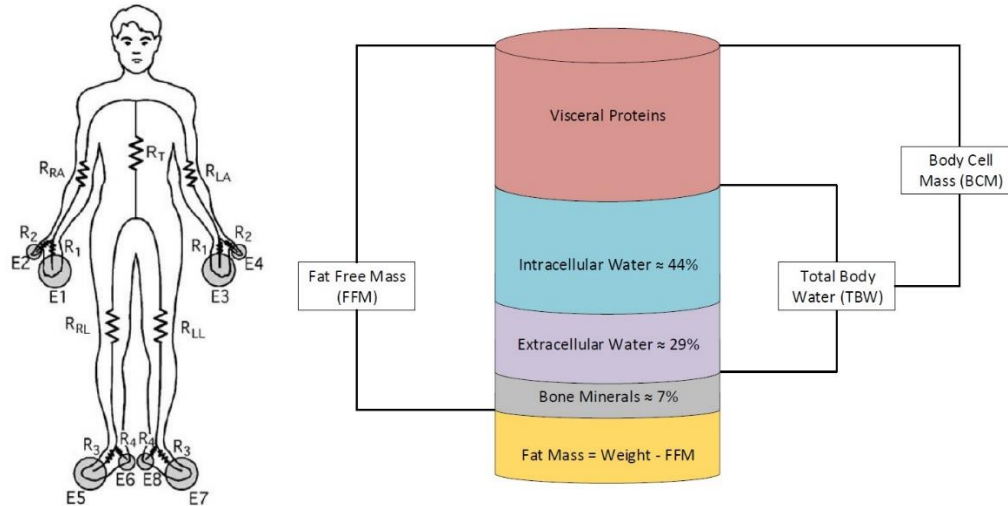
(MF) BIA, the impedance is measured by applying the signals of different frequencies, ranging from 5 kHz to 200 kHz in discrete steps [105, 106]. In MF BIA, the low frequencies are typically used to determine the extracellular water (ECW), while the high frequencies are used to measure the total body water (TBW) with higher accuracy as the capacitive reactance of the cell membranes is significantly reduced [107].

1.2.3 Body Composition Estimation

The human body is composed of different body tissues which are arranged in a very complex manner. The tissues consist of protein, water, minerals, and fat [94]. Fig. 9 shows the composition of the body. The fat tissue contains fat cells with low electrical conductivity. Therefore, it imposes a very high impedance against the electrical current [88]. The lean tissues or fat-free tissues contain electrolytes, extracellular fluid, and intracellular fluid, all of which have high conductivity and low impedance [88]. When an alternating current is injected into the body, it flows through the paths that contain more water. Therefore, the conductivity of the body is proportional to the body water content.

Figure 9

Schematic Diagram of Body Composition



Several empirical equations have been proposed to estimate the fat-free mass, fat mass, and total body water based on the measured impedance. The following equations have low standard errors for predicting FFM and TBW, and therefore, are used in this research.

Body Fat [108]:

$$\begin{aligned} \text{FFM}_{\text{kg}} = & -4.104 + 0.518 \times \frac{\text{Height}^2}{\text{Resistance}} + 0.231 \times \text{Weight} + 0.130 \times \text{Reactance} \\ & + 4.229 \times \text{sex} \end{aligned} \quad (6)$$

$$\text{FM}_{\%} = \left(1 - \frac{\text{FFM}_{\text{kg}}}{\text{Weight}} \right) \times 100\% \quad (7)$$

Body Water [88]:

$$\text{TBW}_{\text{kg}} = 0.377 \times \frac{\text{Height}^2}{\text{Resistance}} + 0.14 \times \text{Weight} - 0.08 \times \text{age} + 2.9 \times \text{Gender} + 4.65 \quad (8)$$

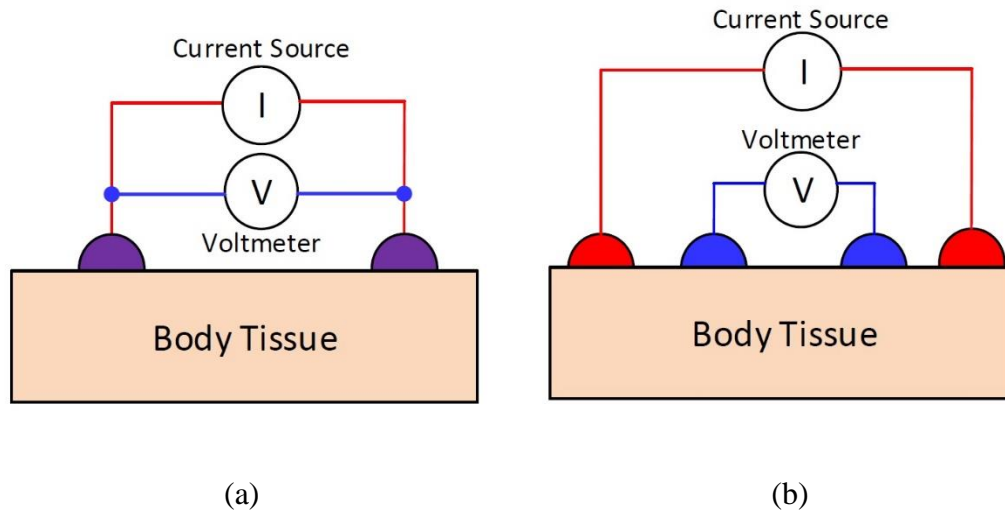
1.2.4 Two-Electrode and Four-Electrode Measurement

The result of the BIA is influenced by the number of electrodes used to perform the measurement. Fig. 10a shows the 2-electrode configuration, where both electrodes are used to simultaneously stimulate and sense the signal. The issue with this method is that it cannot distinguish between the tissue impedance and the skin-electrode contact impedance. Therefore, this technique is not frequently used to perform BIA [88, 109]. However, the 2-electrode method can potentially be used for single frequency applications where the variation of impedance with time is of interest.

In the 4-electrode method, shown in Fig. 10b, two electrodes are used to apply the current and two different electrodes are used to measure the voltage. This technique can eliminate the effects of skin-electrode contact impedance from the measurement [88, 109].

Figure 10

Measurement Techniques for Bioelectrical Impedance



Note. (a) 2-electrode method. (b) 4-electrode method.

1.2.5 State-of-the-Art Research and Commercial Devices

Multiple studies have been performed to evaluate the accuracy of BIA, especially for fat mass measurement. Xie *et al.* [96] examined the accuracy of BIA in analyzing different body composition parameters using dual-energy X-ray absorptiometry (DEXA) as a reference standard. Excellent agreements between both techniques were observed as BIA demonstrated a precision error of just 1% for fat mass measurement. Ling *et al.* [95] performed a similar experiment and demonstrated 97% accuracy for BIA in fat mass measurement. Pribyl *et al.* [110] compared the results from OMRON HBF with BOD POD® which was considered as the “gold standard” body composition tracking system.

Recently much research has been done in designing wearable or portable bioimpedance analyzers for various biomedical applications. Ferreira *et al.* [111] developed a bioimpedance analyzer, which was integrated with a textile-based electrode garment for total body fluid assessment. Choi *et al.* [112] presented a handheld bioimpedance analyzer for daily obesity management using a smartphone. Hersek *et al.* [113] designed a wearable impedance analyzer to assess knee injury and recovery by observing small changes in interstitial fluid volume. Konijnenburg *et al.* [114] developed a wristwatch that could monitor very sensitive changes in body impedance during respiration. These reports show that bioimpedance analyzers can be a valuable tool in biomedical applications, especially for long-term health monitoring.

1.3 Research Motivation and Objectives

Flexible electronics has recently become a rich area of research and development for researchers across different fields of science and engineering. However, several key aspects of this multidisciplinary area remain immature, and therefore, need further investigations. For example, the studies of BIA systems developed on flexible substrates are still rather limited. The selection of the substrates as well as their effects on the BIA's performance have not been fully explored. In addition, the influence of the substrate's mechanical deformations on the operation, performance, and accuracy of flexible devices should be investigated. This research aims to address some of these issues through a systemic examination of materials, designs, and devices in flexible electronics, especially when they are under mechanical deformations. In this project, the first objective is to investigate a wearable BIA system using small size flexible copper electrodes. This study

will explore benefits and issues when using small-size dry electrodes as compared to traditional gel-based Ag/AgCl electrodes. The second objective is to create and characterize wearable BIA systems on flexible substrates. This study will investigate the performance comparison of BIA systems fabricated on paper and plastic substrates. The study will also determine which substrate provides higher electrical and mechanical reliability. The third objective is to explore the challenges and solutions when using highly elastic substrates such as PDMS in flexible electronics and sensors. This study will analyze issues in a flexible-stretchable temperature sensor developed on a PDMS substrate, especially when it undergoes a substantial amount of mechanical deformation, as well as various methods that can minimize those issues in temperature sensing.

1.4 Overview of Dissertation

This work aims to develop and study flexible electronic devices on various flexible substrates using different fabrication techniques. The research involves designing, fabricating, and testing flexible BIA systems and flexible temperature sensors. Chapter 1 provides a detailed review of flexible electronics, covering critical sub-areas that include materials, fabrication techniques, and applications. In particular, BIA is introduced and reviewed as an example of flexible electronics in biomedical applications. In addition, the motivation and objectives of this work are outlined in this chapter. Chapter 2 presents a wearable ring-based bioelectrical impedance analyzer for body fat estimation. This chapter details the development of a lightweight, compact BIA device that contains flexible copper electrodes integrated into a wearable ring. The chapter also discusses the encountered challenges when interfacing dry flexible electrodes with the

human body. Chapter 3 examines BIA devices fabricated on paper and plastic substrates using a printing process. The chapter compares the electrical and mechanical reliability of the circuit developed on both substrates. Furthermore, a comparative analysis of the electrodes developed on paper and plastic substrates is presented. Chapter 4 explores the issues and solutions when the flexible substrate undergoes a substantial amount of mechanical deformation. A flexible temperature sensor is developed on a PDMS substrate using stencil printing. The behavior of the sensor is investigated while bending and stretching the substrate. A novel methodology is developed to provide compensation for the errors caused in the measurements due to mechanical deformations. Chapter 5 summarizes the critical conclusions from this research, and based on the current findings, lists recommendations for future research.

Chapter II

Wearable Ring BIA for Estimation and Monitoring of Body Fat

2.1 Introduction

Obesity is a serious health challenge in today's world, as it can lead to health complications such as stroke, diabetes, osteoarthritis, and coronary heart diseases. Therefore, methods that can precisely measure the body fat mass is crucial, not only for clinicians and patients to work together to improve individuals' health conditions, but also for reducing the risks of all these diseases for a larger population [115]. Over the past few years, both industrial and academic sectors have promoted smart health technology, leading to a wide spectrum of products for clinical applications. Simultaneously, a great number of mobile applications are being developed for direct health management by end users, which then further promote communities focused on electronic health (e-health) [116]. In health management, one particular interest of consumers is on weight monitoring, as evidenced by numerous weight loss methods and diet plans on the market [112]. Due to the urgent needs in obesity prevention and weight management, the significance of body fat monitors has been drastically increased in e-health today. However, most bioelectrical impedance analyzers currently available on the market are cumbersome and expensive. For example, the full-sized body fat analyzers used in clinics and hospitals can weigh more than 35 kg and occupy over 1 m³ of space [117, 118]. Such analyzers are also very expensive and can easily cost more than \$12,000. Furthermore, they are not designed for people with disabilities, especially for those who wear prosthetic legs. Even the off-the-shelf handheld devices (e.g., OMRON body fat monitor HBF 306C) are still relatively large with limited portability (8.75 × 2.5 × 6 in³). Even

though continuous measurement may not be considered absolutely necessary for everyday users, recent research shows that frequent recording of body impedance has a significant impact on patients with effective results for lymphedema treatment [119], hydration content in critically ill patients [120], and daily obesity management [112].

This chapter discusses a novel bioelectrical impedance analyzer for estimating fat mass [121-123]. The objective is to develop a wearable body fat analyzer that is lightweight, inexpensive, accurate, and can communicate wirelessly with smartphones. The designed analyzer consists of a silicone ring with four copper electrodes attached as two pairs. A high-frequency alternating current of 50 kHz is delivered to the body through one pair of electrodes while the voltage across the upper body is measured from the other pair. The measurement is done by a user wearing the ring on one hand and then placing two fingers of the other hand on the outer ring. In addition, the study provides a comparison of skin-electrode contact impedance of small, dry copper electrodes with gel-based Ag/AgCl electrodes by using a three-electrode method. The analyzer is designed to provide compensation for the high contact impedance as well as the parasitic effects caused by the dry electrodes. The device calculates the body impedance and wirelessly transmits this information to a smartphone via Bluetooth. An Android application is developed to calculate the body fat based on the measured impedance and the user profile which includes weight, height, and sex. The fat-free mass equations proposed by four groups, Kyle *et al.* [108], Deurenberg *et al.* [124], Heitman *et al.* [125], and Lohman *et al.* [126], are compared using the results from the designed analyzer; the equation that yields the most correlated result is deployed in the system. The ring BIA device shows comparable performance to a commercial handheld analyzer in estimating the fat mass of

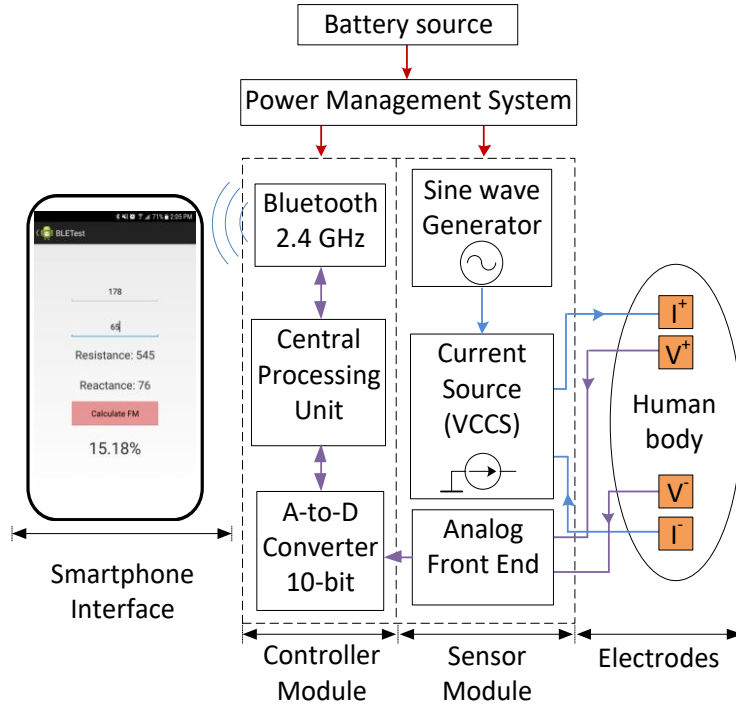
40 human subjects. The novel ring-based wearable device opens new opportunities for future health monitors.

2.2 System Architecture

Fig. 11 illustrates the simplified block diagram of the ring-based analyzer with four primary components: electrodes, a sensor module, a controller module, and a smartphone interface. The electrodes on the ring are used to interface the sensor module with the human body. The microcontroller computes the body impedance by processing the data acquired from the sensor module. The calculated impedance is then transmitted to a connected smartphone via Bluetooth for body fat estimation. Fig. 12 illustrates the detailed architecture of the designed system.

Figure 11

Simplified Block Diagram of the Designed Body Fat Analyzer



Note. The system consists of four main parts, sensor module, controller module, smartphone application, and electrodes for interfacing the body.

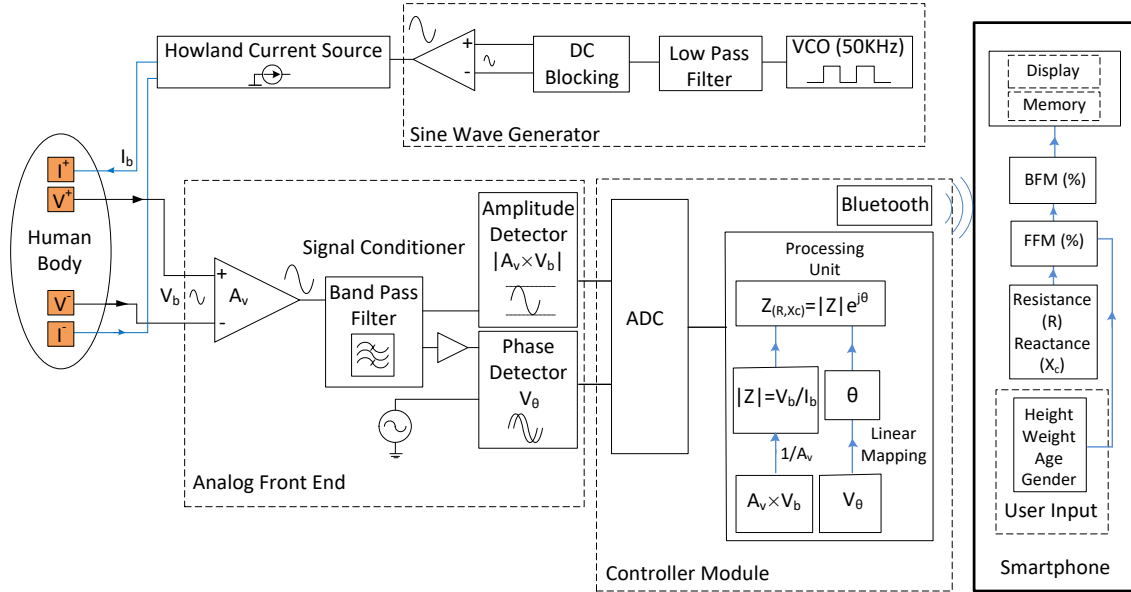
2.2.1 Sensor Module

The designed sensor module contains a wave generator to provide a 50 kHz sinusoidal signal, which is a common frequency used in BIA measurement. The 50 kHz frequency is selected for two reasons: first, it is close to the characteristic frequency of biological tissues, at which the reactance reaches its maximum value [127]; second, it is a robust frequency against various measurement artifacts [128]. A voltage-controlled current source is designed to convert the sine wave voltage signal into a 900 μ A current

signal. The current source is of great significance due to safety reasons, as human safety is assured in vivo by limiting the magnitude of the applied current instead of voltage [129]. In bioimpedance analysis, $I \leq 1$ mA is considered as a safe and widely accepted range for electrical current [130]. The current source uses a Howland circuit design due to its simple principle and comparable performance with other more complicated sources [131]. The sensor module delivers the electrical current and measures the voltage across the body by using four electrodes attached to a wearable ring. A detailed explanation concerning the ring and the electrodes is provided in Section 2.4. The analog front end acquires the voltage signal from the human body for further analysis. The analog front end consists of an instrumentation amplifier which measures the voltage across the human body (V_b), amplifies it, and rejects common mode noises. The next stage of the analog front end is the signal conditioner which is used to remove interfering signals such as electrocardiogram (ECG), electromyogram (EMG), and high-frequency noises caused by electrical activities in the body. The filtered signal is then passed through a high precision amplitude detector to compute the amplitude of the signal ($|A_v \cdot V_b|$) obtained from the body. The filtered signal is simultaneously fed into a phase detector which calculates the phase difference induced by the negative reactance of the body. A phase-locked loop device, CD4046 from Texas Instruments, is used to generate the sinusoidal signal due to its built-in phase comparator and a voltage-controlled oscillator (VCO).

Figure 12

Complete System Architecture of the Designed Body Fat Analyzer



Note. A square signal of 50 kHz is generated by a voltage-controlled oscillator (VCO) and then converted into a sine wave signal. The Howland current source provides a 900 μ A current to the human body via electrodes. The signal acquired from the body is processed by an analog front end for amplitude and phase detection. The microcontroller computes the body impedance and transmits to a connected smartphone via Bluetooth. The smartphone application calculates body fat based on user profile and body impedance.

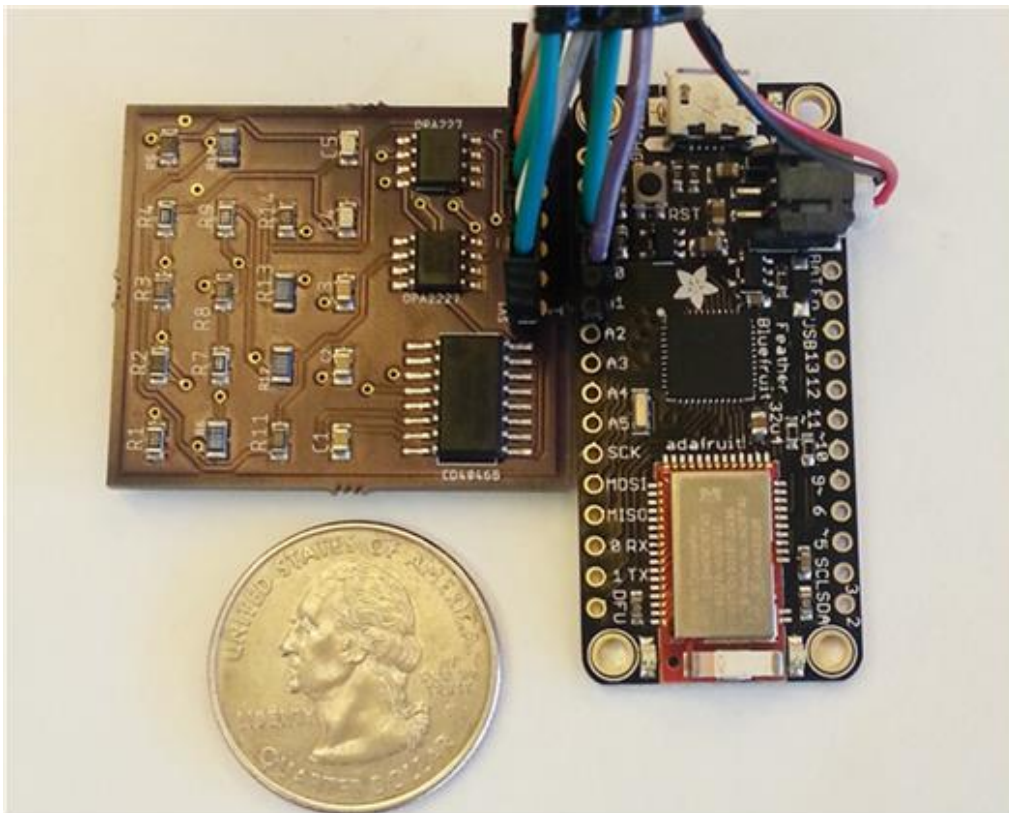
2.2.2 Controller Module

The controller module, responsible for digital signal processing and wireless communication, is built on Adafruit Feather 32u4 which consists of an ATmega32u4 microcontroller (8 MHz and 3.3 V logic) integrated with a Bluetooth module (2.4 GHz).

Fig. 13 depicts the photograph of the microcontroller interfaced with the designed sensor module. The microcontroller has a built-in 10-bit analog-to-digital converter (ADC) to digitize the signal acquired from the analog front end. The collected signals are then processed by the microcontroller to compute the body impedance. The impedance magnitude is calculated by dividing the measured voltage (V_b) by the injected current (I_b).

Figure 13

Photograph of the Sensor Module (left) and Controller Module (right) Interface



2.2.3 Smartphone Interfacing Application

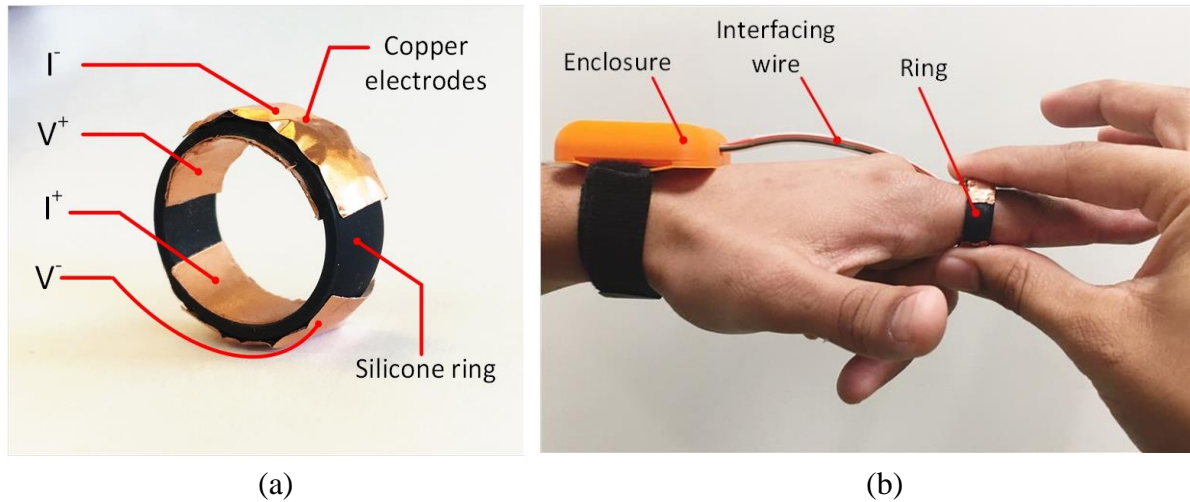
Android Studio is used to develop the smartphone application and the interface for body fat calculations, data management, and tracking of user records. The equations (6 & 7) proposed by Kyle *et al.* for fat-free mass is utilized for estimating the fat mass using the measurement data from the user [108].

2.3 Ring Design and Electrodes

The copper electrodes attached to the wearable ring are shown in Fig. 14a. The major challenge of working with small, dry electrodes is that the recorded bio-signals are often affected by adverse factors such as motion artifacts, electrical noises, and skin-electrode contact impedance [128, 132]. These effects cause an error in the measured value and hence lead to another error in body fat calculations. Generally, the four-electrode method can be used in measuring bio-signals to reduce the skin-electrode contact impedance [133]. In the four-electrode method, one pair of electrodes is used to inject the current ($I+$, $I-$), while the voltage is measured from the other pair ($V+$, $V-$). For our device, all four electrodes on the ring are equal in size and provide a conductive area of 260 mm^2 ($26 \text{ mm} \times 10 \text{ mm}$). The electronics of the ring is placed inside a 3D printed enclosure (with 100% fill), as shown in Fig. 14b, to protect it from dust, moisture, and other harsh environmental conditions. A Velcro strap is attached to the enclosure for the user to wear the device on the wrist. The wires connecting the ring with the hardware are sealed as one bundle. The entire prototype is manufactured with less than \$50. However, the price will reduce drastically if the device can be mass produced.

Figure 14

(a) Silicone Ring with Source (I^+ , I^-) and Sense (V^+ , V^-) Electrodes. (b) Wrist Wearable Hardware Enclosure and Ring Interface



2.4 Experimental Protocol

An Institutional Review Board (IRB) approved protocol was applied to all volunteer subjects in this study. Initially, the weight and height of each subject were measured and recorded by the study coordinator, and later used for calculating the body fat. After screening, the skin-electrode contact impedance was measured for both the dry copper electrodes and the Ag/AgCl electrodes by using a three-electrode method. The details of this method are provided in Section 2.5.2. Afterward, a commercial analyzer OMRON HBF 306C was used to collect the body fat data of each subject. Thereafter, the wearable ring device was used to measure the body impedance and fat mass of the subject. Both the OMRON analyzer and the ring device measure the upper body fat mass; this ensures the collected results are examined in a meaningful way so that they can be used for direct comparison. During the data collection, the subject wore the ring on the

left-hand index finger and then placed the right-hand thumb and index finger on the outer electrodes. As a result, the path of electrical current is established from the left to the right hand through the upper body. An average result of three measurements was made for each subject and utilized for analysis.

Furthermore, although the wearing position might have an impact on the measurement, this impact is negligible when compared to the impedance of the overall upper body. The same experiment was repeated by using large (40.6 mm × 33.02 mm), gel-base Ag/AgCl patches as the electrodes. The Ag/AgCl electrodes, placed on the wrists of both arms, were set up following the four-electrode method. A total of 40 healthy human subjects, all over 18 years old, were recruited for this study. Table 1 shows the statistics of the 40 participated subjects. To eliminate any potential concerns over passing an electrical current through the human bodies, the study excluded pregnant women and subjects with cardiac pacemakers or other types of medical implants. All the subjects were asked not to exercise, eat, or drink for at least 2 hours before the experiment.

Table 1

Anthropic Measurement of the Study Group

Parameters	Mean ± SD	Range
Age (yr)	23.55 ± 4.74	21 – 42
Height (cm)	175.5 ± 7.4	163 – 191

Parameters	Mean \pm SD	Range
Weight (kg)	71 \pm 14	57 – 117
BMI	24.78 \pm 5.11	17.6 – 40
Body fat (%)	16.12 \pm 6.53	5.8 – 35.7
Total subjects = 40	Male = 35	Female = 5

2.5 Results and Discussion

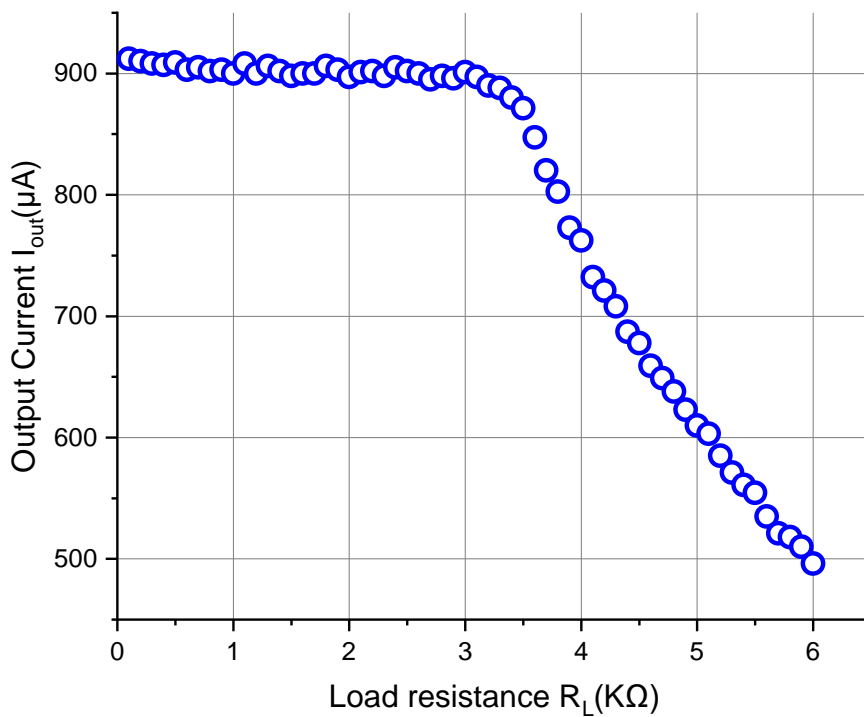
2.5.1 Hardware Verification

Because the body impedance varies from person to person, it is crucial to minimize the effect of subject-specific impedance on the electronics and the final results. To ensure that our device can accommodate different body types, the voltage-controlled current source limitation on body impedance was measured by increasing the load resistance from 10 Ω to 6 k Ω . Fig. 15 demonstrates that the current source can deliver a consistent current of 900 μ A in a wide range, from 10 Ω to 3.3 k Ω . As a result, the system can work properly and accurately for almost all human subjects because the body impedance of most people is less than 1 k Ω [134]. Fig. 16a illustrates a human body tissue model, represented by discrete electrical components (R_e for extracellular fluids, R_i for intracellular fluids, and C_m for cell membranes), that can help evaluate the performance of the BIA system [100]. For a single frequency of 50 kHz, the overall model can be further simplified as an effective capacitor C_{eff} in a series connection with an effective resistor R_{eff} , as illustrated in Fig. 16b. The values of $R_{eff} = 530 \Omega$ and $C_{eff} = 47 \text{ nF}$, obtained through a full-scale Seca Medical Body Composition Analyzer,

correspond to the impedance data of a 31-year old healthy male. The current consumption of the designed sensor module is measured as 21.28 mA when it is supplied with a battery source of 3.7 V. The power consumption of the entire system is 102.64 mW in the active mode while communicating to a smartphone via Bluetooth. The performance results of the designed bioelectrical impedance analyzer are summarized in Table 2.

Figure 15

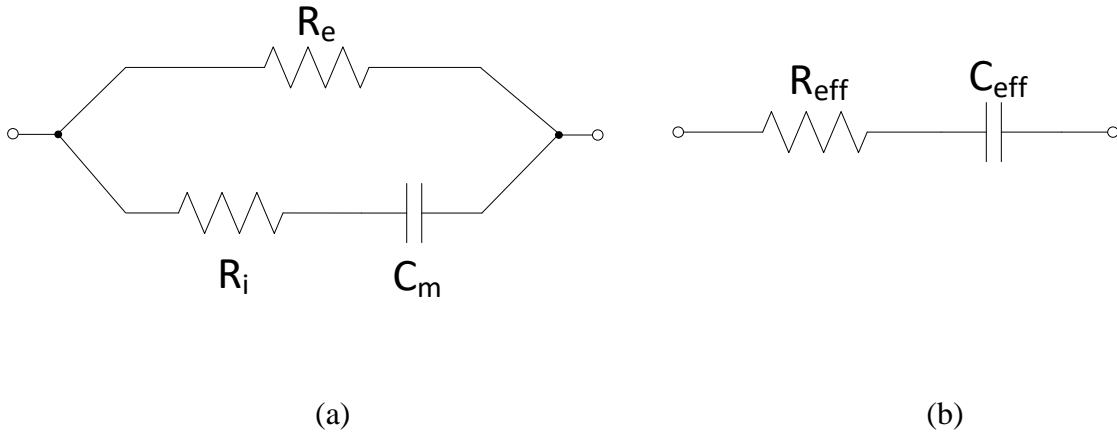
Output Current (I_{out}) Against Load Resistance (R_L) for the Howland Current Source



Note. The current source can provide a consistent 900 μ A current for a load up to 3.3 k Ω .

Figure 16

Equivalent Electrical Model of the Human Body



Note. (a) R_e and R_i are body fluid resistances. C_m is the cell membrane capacitance. (b) In case of single frequency, the model can be simplified as a series combination of effective resistance R_{eff} and capacitance C_{eff} .

Table 2

Performance Results

Parameters	Value
Supply voltage	3.7 V
Power consumption	78.73 mW (sensor) 102.64 mW (system)
Electrode size	26 mm × 10 mm
Sensor module size	50 mm × 48 mm

Parameters	Value
Impedance range	$10\Omega \leq Z \leq 3.3\text{ K}\Omega$
Phase range	$0^\circ \leq \theta \leq 90^\circ$
Impedance measurement error	1.6%
Phase measurement error	1.9%

2.5.2 Electrode Characterization and Impedance Measurement

There are some major challenges in designing bioimpedance analyzers while using small-sized, dry electrodes. These electrodes provide unique benefits for wearable devices: their dimensions are well suited for small spaces; no frequent electrode replacement is needed; they are sturdy and can last a long time to ensure device operation; they do not contain chemicals that may cause skin irritation or discomfort. However, the problem arises when these electrodes have an initial contact with the skin and cause the contact impedance. The skin-electrode contact impedance is important in BIA as higher contact impedance decreases the amplitude of the signal obtained from the body, which can lead to measurement errors. In order to study the performance of electrodes, the contact impedance was measured for both Ag/AgCl electrodes (40.6 mm × 33.02 mm) and dry copper electrodes (26 mm × 10 mm) by using the three-electrode method proposed by Spach *et al.* [135]. In this method, three electrodes are placed on the arm as shown in Fig. 17 and the impedance of the middle electrode is calculated. Electrodes 1 and 2 are connected to a sine wave generator (50 kHz) and the voltage is

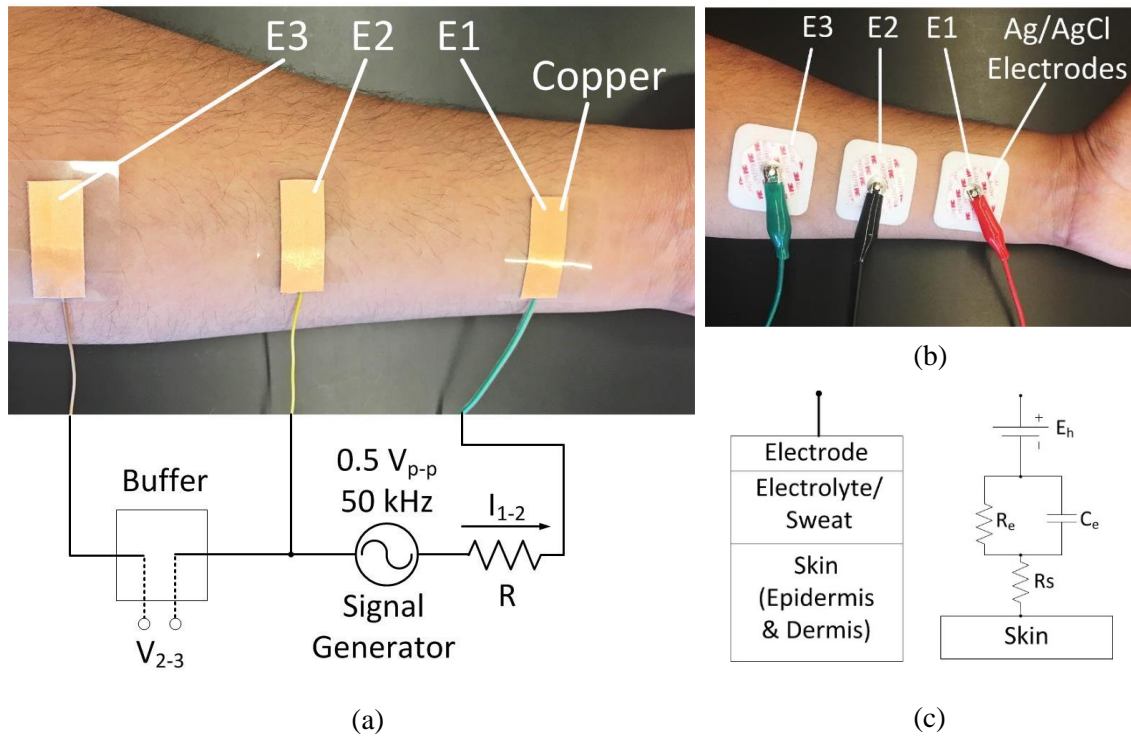
measured across electrodes 2 and 3. The contact impedance of electrode 2 can be calculated by using the following equation:

$$Z_2 = \frac{V_{2-3}}{I_{1-2}} \quad (9)$$

where Z_2 is the skin contact impedance of electrode 2, I_{1-2} is the electrical current through electrodes 1 and 2, and V_{2-3} is the voltage measured across electrodes 2 and 3. The three-electrode method was performed by using a function generator and an oscilloscope.

Figure 17

Three-Electrode Measurement



Note. Three-electrode method is used to measure the skin-electrode contact impedance of

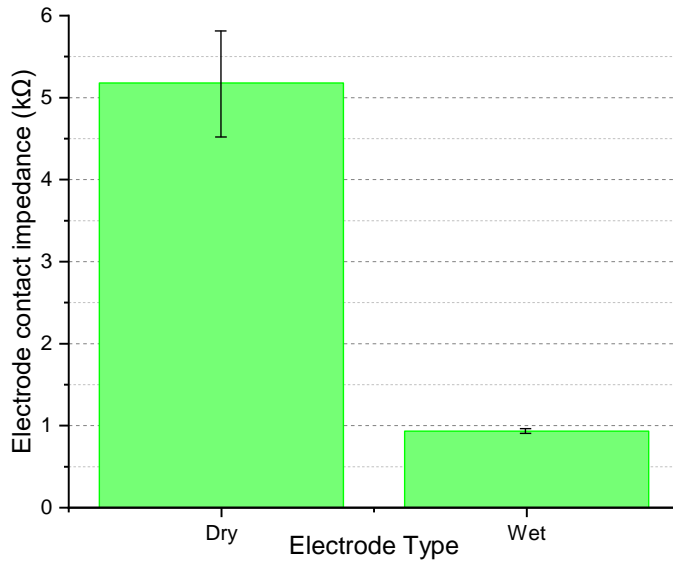
(a) dry copper electrodes (26 mm × 10 mm) and (b) Ag/AgCl electrodes (40.6 mm × 33.02 mm). (c) Skin-electrode contact model where E_{hc} is the half cell potential, R_e and C_e are electrode resistance and capacitance, respectively, and R_s is the electrolyte/sweat resistance.

Fig. 18 shows that the contact impedance of dry copper electrodes (5.18 ± 0.66 k Ω) is much higher than that of wet electrodes (933.37 ± 40.06 Ω). This is mainly due to the absence of conductive gel and the smaller area of skin contact with the dry electrodes. Thus, in order to eliminate the skin-contact impedance, the four-electrode method is used for bioelectrical impedance measurement. This technique allows removing the electrode contact impedance from the body impedance, given that the measurement circuit has a sufficiently high input impedance [136]. However, the small size of dry electrodes constricts the injected current, creating a constricting zone which leads to a higher impedance. The four-electrode method is unable to eliminate the higher impedance caused by the current constricting geometry [128]. The average impedance caused by the current constriction of the dry electrodes is calculated to be $R_p = 25.37$ Ω and $X_p = -15.8$ Ω , obtained through a set of control experiments in which dry and wet electrodes are used at the same locations with the same four-electrode setup for BIA measurements. One way to reduce this impedance is by increasing the size of the electrodes [137]. The large electrodes will provide a wider path for the electrical current to go through the body.

Figure 18

Skin-Electrode Contact Impedance of Dry Copper Electrodes and Gel-Based Ag/AgCl

Electrodes at 50 kHz

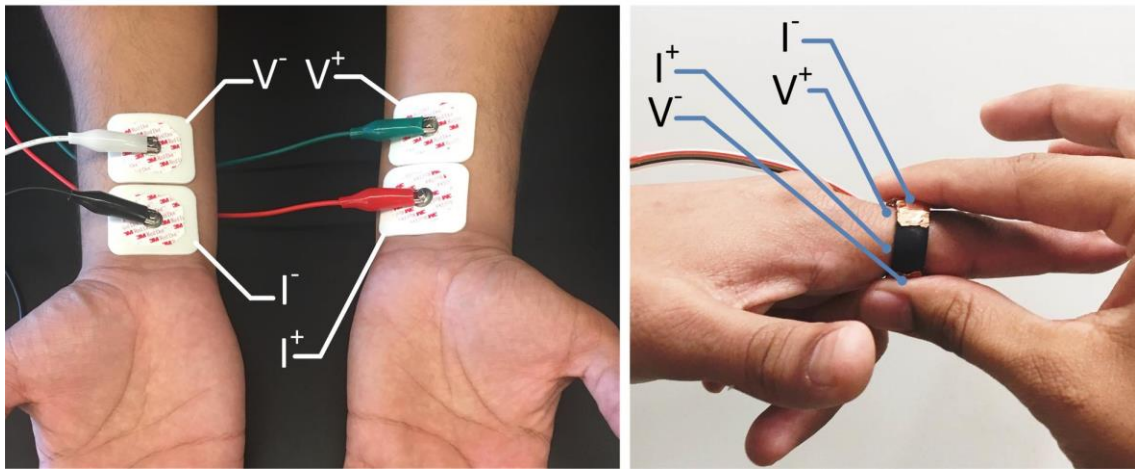


Most commercial body fat analyzers use large electrodes to minimize the effect of the contact impedance, e.g., the OMRON HBF 306C has an electrode size of 95 mm × 50 mm. However, such a size is not possible for a wearable ring device; therefore, other compensation methods are needed. Another problem is that the human hands, including fingers, impose a great amount of impedance despite the fact that they only represent a very small portion of the human body. For our subject group, the average wrist-to-finger resistance and reactance components are calculated as $R_{\text{hand}} = 71.88 \Omega$ and $X_{\text{hand}} = -29.62 \Omega$, respectively. This can cause an error in the estimation of fat-free mass and thus fat mass. In order to compensate for these problems, the body resistance/reactance measured using the small, dry copper electrodes on the ring are compared with gel-based Ag/AgCl

electrodes placed on the wrists. Fig. 19 shows the four-electrode method to measure body impedance. This measurement is performed on all 40 subjects by using the designed bio-electrical impedance analyzer.

Figure 19

Four-Electrode Measurement



(a)

(b)

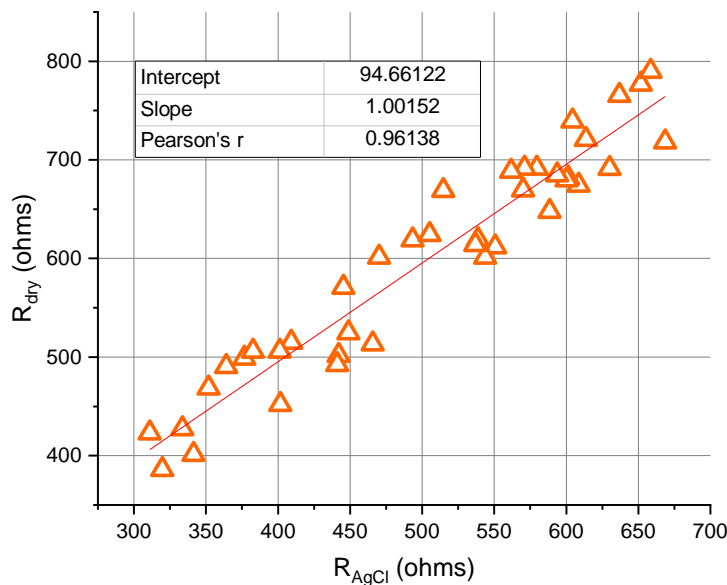
Note. Four-electrode method is used to eliminate the electrode impedance and measure only the body impedance. (a) Wrist-to-wrist measurement using Ag/AgCl electrodes. (b) Finger-to-finger measurement using dry copper electrodes.

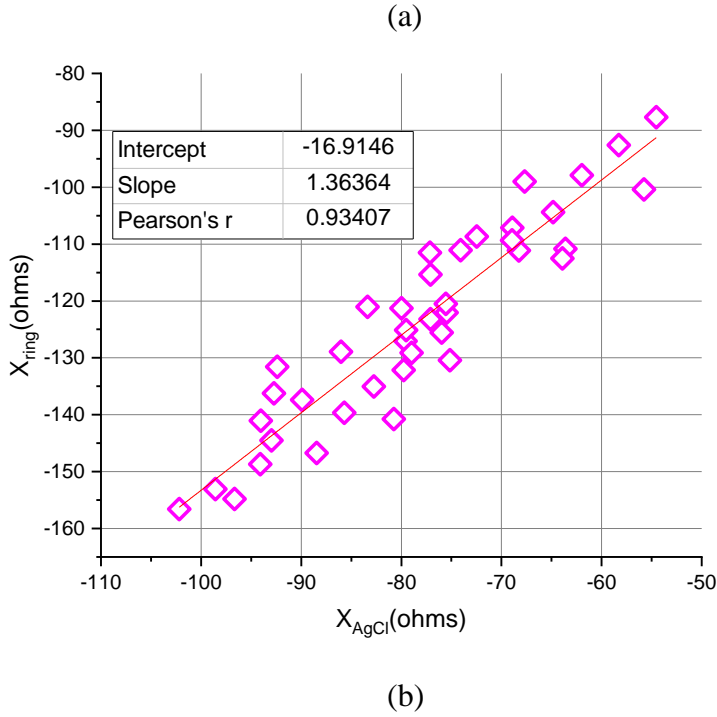
Fig. 20a compares the body resistance data R_{ring} measured from the ring electrodes against the results R_{AgCl} from the Ag/AgCl electrodes. The comparison shows a highly correlated linear regression with a correlation coefficient $r = 0.96$ for the two types of electrodes. The results also show that the body resistance obtained from the ring

electrodes is higher than that from the gel-based Ag/AgCl electrodes, due to the high impedance of hands and parasitic effects. Fig. 20b shows the correlation plot of the body reactance measured from both types of electrodes, X_{ring} for the ring electrodes and X_{AgCl} for the gel-based electrodes. Similarly, the correlation coefficient for the reactance is also high with $r = 0.93$ and the ring electrodes impose larger negative reactance. These high correlation coefficients indicate that the variation in body impedance can be reliably measured by the ring analyzer. The difference of impedance can be obtained by subtracting the absolute average of the ring electrode measurement from the absolute average of the Ag/AgCl electrodes ($R_d = R_{hand} + R_p = 97.25 \Omega$, $X_d = X_{hand} + X_p = -45.42 \Omega$). The microcontroller firmware is then programmed to compensate for these values, resulting in accurate readings of the body fat data.

Figure 20

Linear Regression for Impedance Using Wet and Dry Electrodes





Note (a) Linear regression for resistance using Ag/AgCl electrode (R_{AgCl}) and dry electrodes on ring (R_{dry}). (b) Linear regression for reactance using both electrodes X_{AgCl} and X_{ring} .

2.5.3 Body Fat Estimation and Equation Comparison

The designed ring analyzer was compared with a reference device, handheld OMRON HBF 306C, in terms of its performance for body fat mass measurement. In this study, four different FFM equations proposed by Kyle *et al.* [108], Deurenberg *et al.* [138], Heitman *et al.* [125], and Lohman *et al.* [126] were compared using the designed device for body fat assessment by linear regression and Bland-Altman plots. Table 3 shows the correlation in descending order as well as the differences in mean and standard deviation (SD) for the two devices using the selected FFM equations. The OMRON monitor has the strongest correlation with the designed ring analyzer when the equation

proposed by Kyle *et al.* was utilized ($r = 0.90$, $1.63 \pm 3.41\%$). The Deurenberg FFM equation demonstrates the second highest correlation ($r = 0.89$) and a mean difference of $2.88 \pm 4.93\%$. The Heitman equation demonstrates an intermediate correlation ($r = 0.84$); however, its standard deviation from the mean difference is the highest ($2.16 \pm 6.08\%$). Finally, the equation proposed by Lohman *et al.* shows the weakest correlation ($r = 0.76$) and a high standard deviation from the mean difference $2.70 \pm 5.98\%$. Although all four FFM equations are correlated and can therefore be used for further analysis, the equation proposed by Kyle *et al.* yields results that are most correlated to the OMRON analyzer ($r = 0.90$). Therefore, this equation has been utilized in data analysis for our device.

Fig. 21 shows the linear regression between our designed ring and the reference monitor, with the x-axis representing the body fat (%) measured by the reference monitor and the y-axis representing the data measured by the ring device. The correlation coefficient for the linear regression is $r = 0.9$ (maximum correlation $r = 1$) which demonstrates a strong correlation for body fat measurement between both devices. This high value of correlation coefficient shows that the measurements obtained from the reference monitor can also be reliably obtained from the designed ring device. The Bland-Altman plot for the designed device and the reference monitor is shown in Fig. 22, with the x-axis representing the average fat mass values from both analyzers and the y-axis showing the difference between them. The solid red line in the middle indicates the difference in mean of 1.63% and the two dashed lines indicate the range of $\pm 6.82\%$ ($\pm 2 \times$ SD). The plot shows that only 2 out of 40 subjects lie outside the 95% limit of agreement.

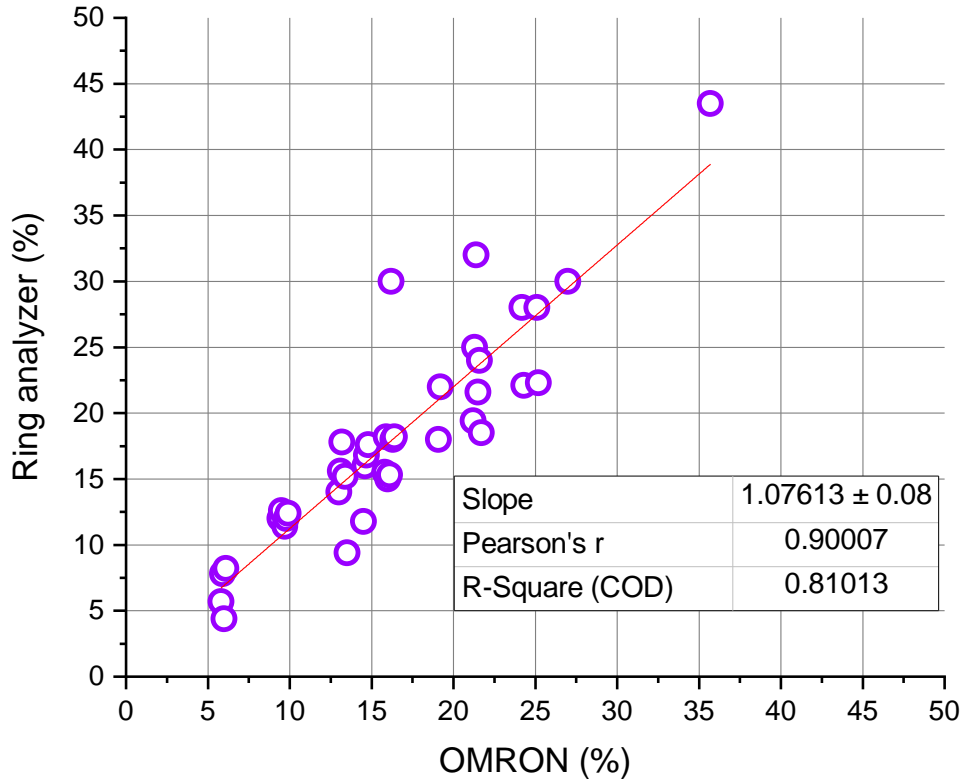
Table 3*Bioelectrical Impedance Analysis Equations for Fat-Free Mass (FFM) Estimation*

Source	Equation	r-value	Difference in Mean \pm SD
Kyle <i>et al.</i> [108]	$FFM_{kg} = -4.104 + 0.518 * \frac{(height)^2}{resistance}$ $+ 0.231 * weight + 0.130$ $* reactance + 4.229 * sex$	0.90	1.63 \pm 3.41%
Deurenberg <i>et al.</i> [124]	$FFM_{kg} = -12.44 + 0.34 * \frac{(height)^2}{resistance}$ $+ 0.153 * height + 0.273$ $* weight - 0.127$ $* age + 4.56 * sex$	0.89	2.88 \pm 4.93%
Heitman <i>et al.</i> [125]	$FFM_{kg} = -14.94 + 0.279 * \frac{(height)^2}{resistance}$ $+ 0.181 * weight + 0.231$ $* height + 0.064$ $* sex - 0.077 * age$	0.84	2.16 \pm 6.08%
Lohman <i>et al.</i> [126]	$FFM_{kg} \text{ for Men}$ $= 5.32 + 0.485 * \frac{(height)^2}{resistance}$ $+ 0.338 * weight$ $FFM_{kg} \text{ for Women}$ $= 6.34 + 0.474 * \frac{(height)^2}{resistance}$ $+ 0.180 * weight$	0.76	2.70 \pm 5.98%

The variations in the calculated r-values for different equations may come from the population differences under different studies. The anthropometric body fat estimation equations may have been derived from a test group that is very different from our study. For example, Heitman *et al.* derived the FFM equation by conducting an experiment on elderly Dane population which were 36-65 years old. Although the results from the designed device and the OMRON analyzer are highly correlated, there is still a variation of 10% in the linear regression for the body fat percentage. This variation is mainly caused by two outlier subjects falling outside of the 95% limit of agreement, as shown in Fig. 22. One of the subjects is obese and has a body fat of 37% while the other subject has a muscular athletic build. Furthermore, the equation for calculating the body fat and skin impedance compensation methodology deployed in the OMRON analyzer is not revealed by the manufacturer. Last, besides the average value subtraction method used in this research, there are other methods that can be used to compensate for the parasitic capacitance due to large electrode impedance such as linear mapping [113] and additional compensating circuitry [137].

Figure 21

Body Fat Correlation Plot

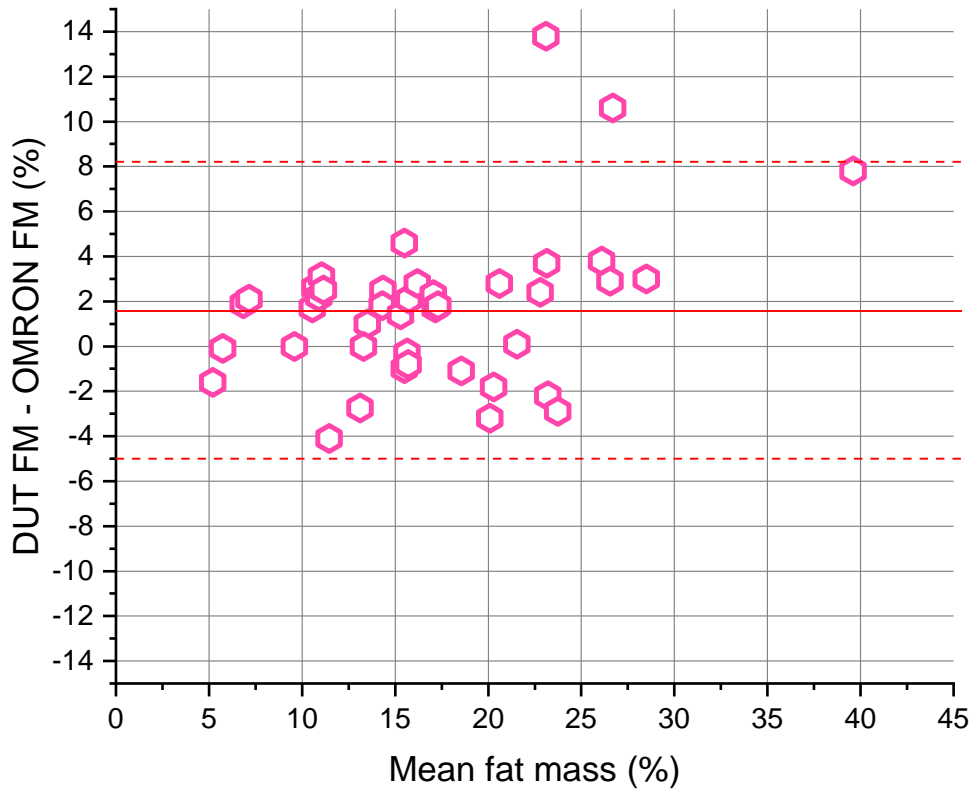


Note. Body fat correlation plot between OMRON and the designed ring wearable device.

The linear regression demonstrates a strong correlation with $r = 0.90$ (Kyle *et al.* FFM equation).

Figure 22

Bland-Altman Plot



Note. Bland-Altman plot with mean difference and 95% limit of agreement. 38 out of 40 subjects lie within the limit (Kyle *et al.* FFM equation).

Table 4 shows the comprehensive comparison of other previously reported bioimpedance systems with this work. The architecture of the systems can be categorized as (i) PCB design using discrete components, (ii) computer interfaced designs, and (iii) applications specific integrated circuits (ASIC). The systems designed using ASIC architectures are small-sized and consume low power, but they are expensive to fabricate. Computer interfaced analyzers cannot be considered as completely wearable. Custom

PCB circuits using discrete components provide a low-cost solution for the rapid development of electronic systems. These devices consume sufficiently low power and can achieve small size to be implemented in wearable bioimpedance analyzers. The proposed system is developed using discrete components which makes it low cost, as compared to ASIC and computer interfaced designs. The designed device is compact enough to be comfortably worn on the hand. Furthermore, the device is tested against a standard commercial handheld body fat analyzer OMRON HBF 360 and demonstrates a strong positive linear relationship ($r = 0.90$).

Table 4

Comparison of the Designed Bioelectrical Impedance Analyzer with Similar Systems

Source	Technology	Size	Correlation/Accuracy	Form factor
[111]	Discrete components	$90 \times 50 \times 17 \text{ mm}^3$ (Device)	$r = 0.96$ (Body fluid estimation)	Wearable textile
[112]	Discrete components	$142 \times 72 \times 6 \text{ mm}^3$ (Device)	$r = 0.95$ (Body fat estimation)	Handheld/portable
[113]	Analog front end + computer	$20.32 \times 20.32 \text{ mm}^2$ (Analog front end)	$r = 0.85$ (Body impedance)	Wearable on legs
[114]	ASIC	$6.5 \times 5.8 \text{ mm}^2$ (IC Die)	-	Wristwatch

Source	Technology	Size	Correlation/Accuracy	Form factor
[139]	Discrete components	48 × 30 × 20 cm ³ (Sensor + controller)	92.8% (Accuracy for RC circuit measurement)	Wearable/compact
This work	Discrete components	50 mm × 48 mm (Sensor module)	r = 0.9 (Body fat estimation)	Wearable ring

2.5.4 Conclusion

In this chapter, we introduced a novel ring-based wearable bioelectrical impedance measurement device and demonstrated its ability to acquire significant physiological measurements from the human body, especially the fat mass. The wearable analyzer provides a comfortable, easy, and reliable method to monitor body fat in a home-based environment. The developed system minimizes the electrode placement error, and at the same time, compensates for the parasitic impedance caused by the small, dry electrodes. Furthermore, the electrode analysis demonstrated that although the dry electrodes led to higher impedance and lower signal-to noise ratio, these factors could be quantified and compensated for. After compensation, these dry electrodes demonstrated comparable performance to commercial Ag/AgCl electrodes while providing an inexpensive solution for long term health monitoring in wearable medical devices. The designed analyzer was tested on 40 volunteer subjects and demonstrated comparable performance to a commercial body fat analyzer OMRON HBF 306C. The correlation plot and the Bland-Altman plot are obtained using the measured data for both devices. The

compact design, along with the small electrodes and accurate measurements, allow for potential integration of the ring with ASIC (application-specific integrated circuit) based impedance analyzer in the future. This would allow us to further miniaturize the hardware so that the entire device can be encapsulated on the ring. The next iteration of this device will include capabilities for body hydration content, skeletal mass, and muscle mass estimation. Due to its accuracy, wearability, small size, and convenience, the developed device demonstrates great potential to replace and/or complement commercial analyzers, especially in smart health applications.

Chapter III

Flexible Bioimpedance Analyzer on Paper and Plastic Substrates

3.1 Introduction

Recently much attention has been paid to the development of flexible electronic sensors, as this area has great potential in future healthcare applications [140]. Current commercial wearable healthcare devices such as smartwatches from Fitbit and Apple are typically fabricated on small rigid circuit boards. Tech companies are continuously working towards developing devices that are more compact and easier to wear with better functionalities. At the same time, building electronics directly on flexible substrates provides an alternative route with unique advantages for future wearable devices; for example, the flexible devices will be lightweight, inexpensive, biocompatible, and can be easily fit onto various curved surfaces for long-term use [141]. However, despite all these advantages, flexible sensors are vulnerable to electrical and mechanical failures due to humidity, corrosion, and extreme folding [142]. Therefore, the substrate can be coated with a soft gel material, such as silicone epoxy resin, to protect the electronic module and provide a uniform stress distribution during bending [143]. It should be noted that the term “flexible” refers to the tolerance ranges of different mechanical deformation modes. Plastic substrates are chosen to develop flexible electronics based on their characteristics, e.g., chemical and thermal properties, transparency, and high glass transition temperature [144]. Paper is another flexible substrate that has various attractive properties e.g., biocompatibility, biodegradability, and breathability [145]. Paper is composed of entangled cellulose fibers which tend to absorb moisture. Interestingly, this porous

property can also provide a unique advantage of enhanced bonding strength between the paper substrate and the mounted electronic components by absorbing part of the bonding material into the fibrous structure.

In this work, we have developed multi-frequency electrical bio-impedance analyzers on two flexible substrates, paper (Whatman cellulose chromatographic grade 1 paper) and plastic (3M transparency film for overhead projectors), and evaluated their performance against a similar system developed on a conventional rigid printed circuit board (PCB) [146]. Electrical bio-impedance (EBI) is a technique widely used in medical electronics for body composition analysis [94]. In EBI, a small sinusoidal electrical current is injected into the human body at a single (50 kHz) or multiple frequencies (5 kHz – 200 kHz). The voltage and phase signals across the body are measured to compute the complex impedance values with the real part representing resistance (R) and the imaginary part reactance (X_c). Furthermore, electrode analysis is performed by fabricating dry electrodes on flexible substrates and comparing them with commercial gel-based Ag/AgCl electrodes. The measurement results on 12 subjects demonstrate that both paper- and plastic-based flexible analyzers show comparable performance to the rigid PCB devices. The novel bio-impedance analyzers presented in this work, with high flexibility and enhanced wearability, can open new opportunities for future wearable health monitors.

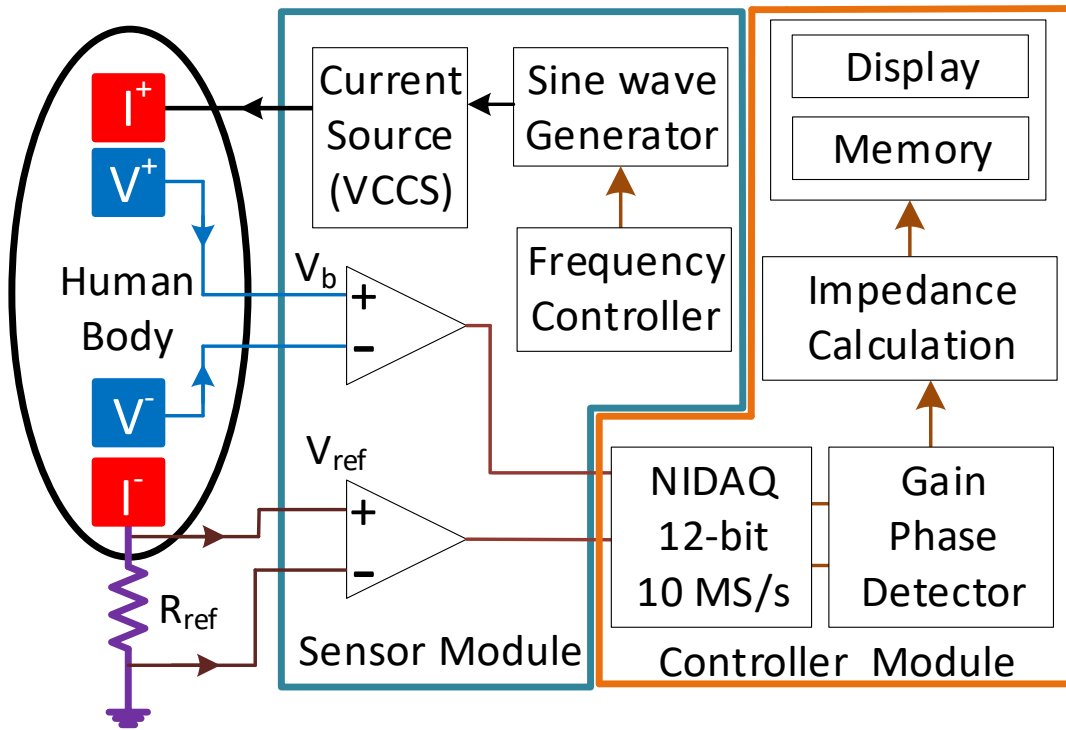
3.2 System Architecture

The developed EBI system relies on magnitude-ratio-detection to estimate the body impedance [147]. The platform consists of a flexible wrist wearable sensor module interfaced with a data acquisition device NIDAQ (PCI-6115) and LabVIEW for signal

analysis. Fig. 23 shows the simplified block diagram of the designed EBI system. The sensor module consists of a multi-frequency sinewave generator with frequencies ranging from 5 kHz – 200 kHz in 20 discrete steps. The sensor module interfaces with the human body via four electrodes. A controlled current of 900 μA flows through the source electrodes (I+, I-) to stimulate the body tissue. The voltage across the body is measured using two sense electrodes (V+, V-). The current also flows through a reference resistor ($R_{\text{ref}} = 150 \Omega$) which is connected in series with the body. Two separate amplifiers are used to measure the voltages across the body and the reference resistor. These signals are analyzed by LabVIEW to compute the body impedance.

Figure 23

Simplified Block Diagram of Electrical Bio-Impedance Analyzer Interfacing with the Human Body



3.3 Fabrication Procedure

The fabrication procedure of the flexible device is shown in Fig. 24. Initially, the flexible substrate was prepared by removing unwanted dust particles from the surface. The circuit, along with the electrodes, was printed on the substrate by dispensing a conductive silver ink (Alfa Aesar 45661) via a Voltera V-one fluid dispensing system. Afterward, the silver was cured at 90°C for 30 min in a furnace (Thermolyne FD1530M). In order to create strong bonding between the electronic components and the wire traces, an additional layer of silver was dispensed on the bonding pads. The components were

placed on the substrate and the bonding pads were cured. Fig. 25 shows the photographs of EBI sensor modules developed on flexible paper and plastic substrates.

Figure 24

Flexible Printed Circuit Fabrication Procedure

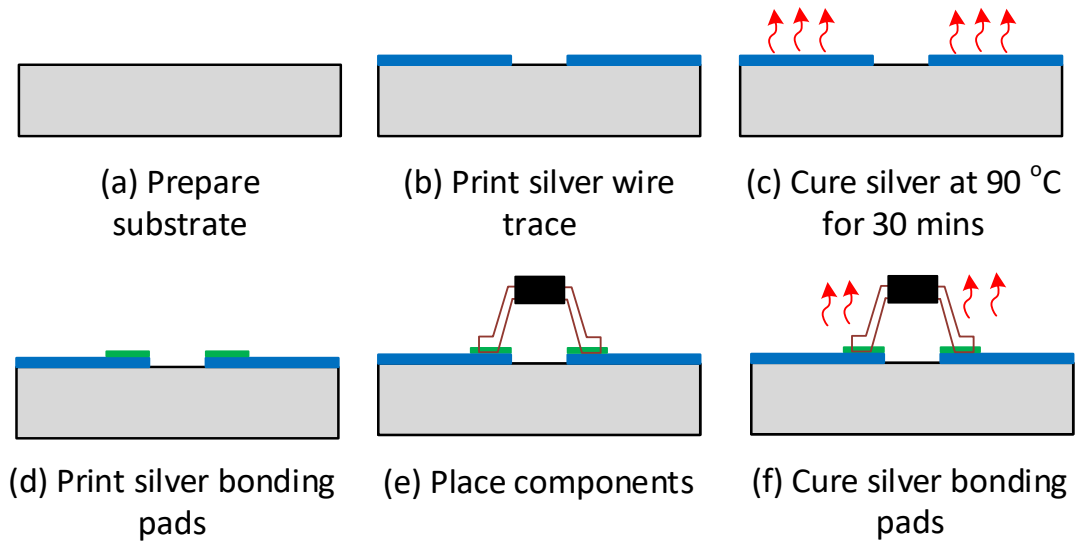
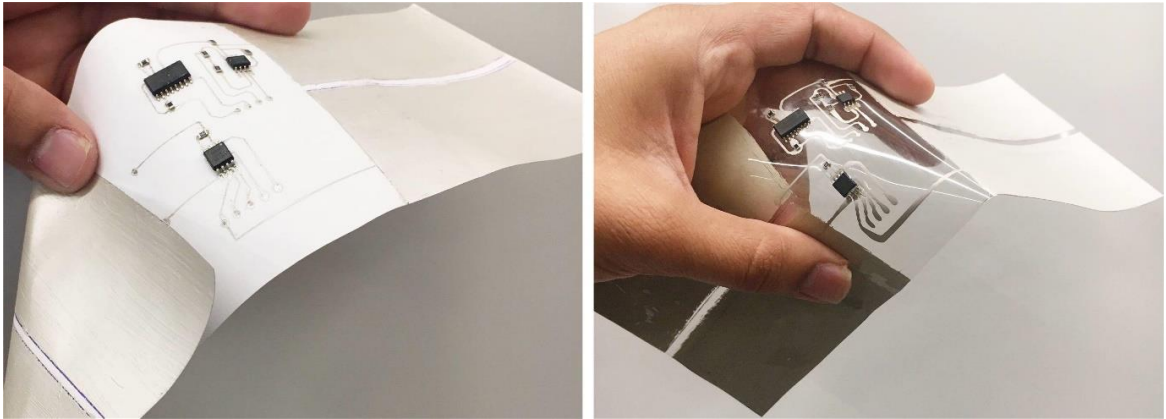


Figure 25

Photograph of the Developed Bioimpedance Sensor Modules



(a)

(b)

Note. The bio-impedance sensor modules with integrated electrodes fabricated on (a) paper and (b) plastic.

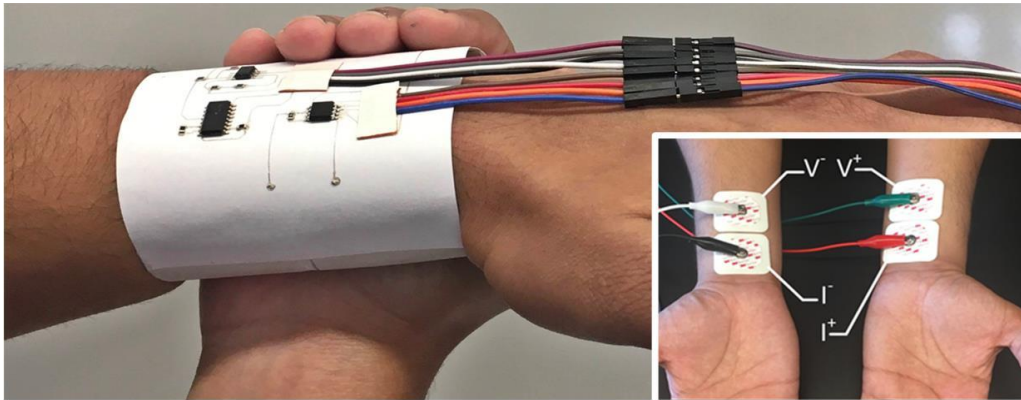
3.4 Experimental Procedure

The EBI measurements were conducted on 12 subjects, following an approved protocol by the Rowan University Institutional Review Board (IRB). The height, weight, age, and sex of all subjects were noted. After the initial screening, the first round of EBI analysis was performed by using gel-based Ag/AgCl electrodes interfaced with the sensor module developed on a rigid PCB. The wet electrodes were attached to both wrists of the subject. The second round of EBI analysis was based on the flexible paper-based device. Each subject was asked to wear the paper EBI sensor on the wrist of the left hand and then place the right-hand palm on the outer electrodes as shown in Fig. 26. This resulted in a complete electrical current path through the upper body during the EBI measurement.

The same experiment was repeated for the plastic-based EBI system in the third round of experiment.

Figure 26

Bio-Impedance Analysis Measurement



Note. The measurement is performed by wearing the flexible sensor on one hand and placing the palm of other hand on outer electrodes. Inset: ECG electrodes are placed on wrists.

3.5 Results and Discussion

3.5.1 Mechanical Testing

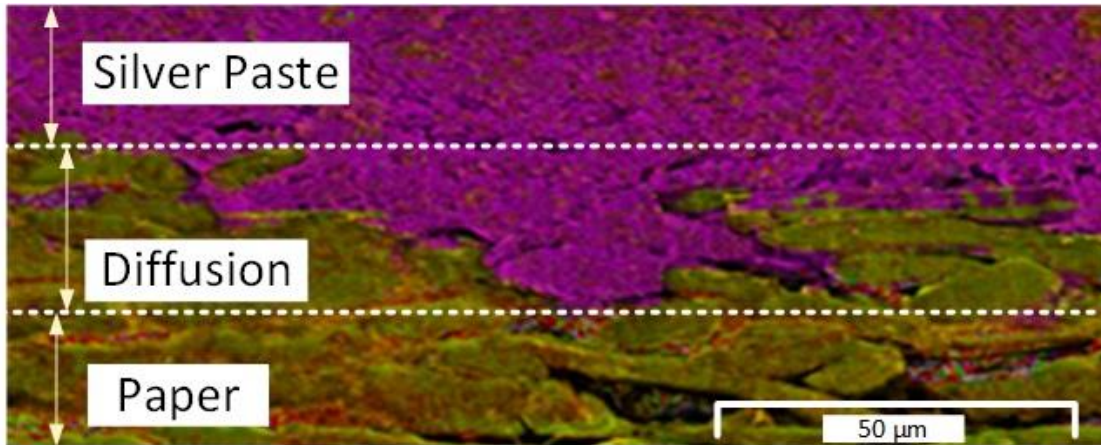
In general, the bonds between the electronic components and the flexible substrate are the most vulnerable structure to mechanical deformation out of an entire flexible device. For this reason, the components are placed on the areas of the substrate that experience the least amount of bending. However, these components will still face some tensile strain during device operation; device failure may occur due to small cracks if not

handled properly. Failure analysis is therefore performed in order to determine the maximum bending angle at which the electrical bond breaks. Five samples on both substrates (paper and plastic) are prepared with electrical components bonded using silver. The substrates are slowly bent to the angle at which the electrical connection at one of the bonding pads breaks. The mean failure angles for the paper and plastic substrates are $53^\circ \pm 4^\circ$ and $42^\circ \pm 3^\circ$, respectively, showing that the paper-based circuits are mechanically stronger. The stronger bonds for the paper substrate are a result of its fibrous, porous structures. The results from these failure measurements can serve as indicators for sensor placement on human bodies, as the skin-mountable devices and sensors undergo different levels of strain when placed at different parts of the body. A wearable electronic device attached to the wrist faces a strain of 0.44%, on the elbow 1.13%, and on the shoulder 1.5%. The sensors attached to joints such as the knee and finger undergo a high strain of 16% when the joints are flexed [148].

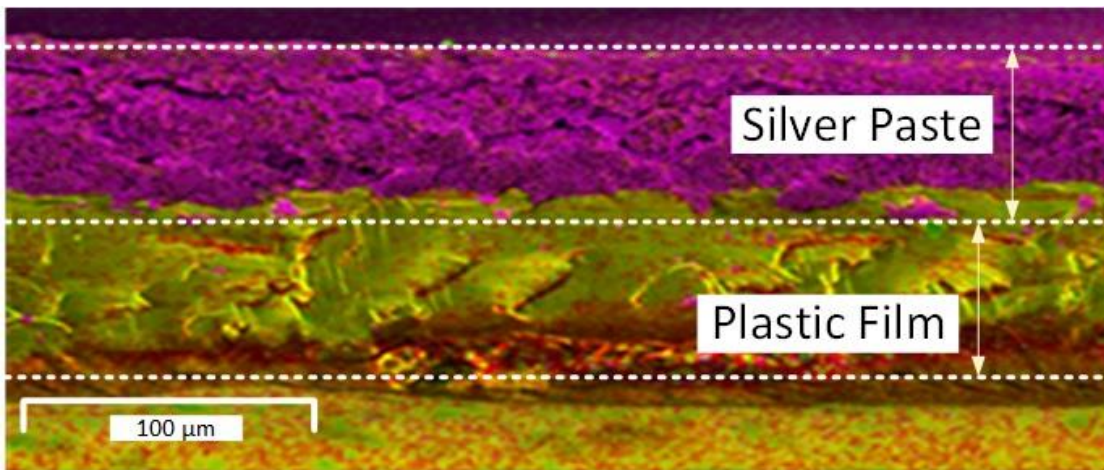
Fig. 27 shows the cross-sectional views, based on the energy-dispersive X-ray spectroscopy (EDS) elemental maps on a scanning electron microscope (SEM), of the printed silver on paper and plastic substrates. The pores in the fibrous structure allow the uncured silver to diffuse into the paper substrate, which strengthens the bond between the two materials. By comparison, the plastic is a nonporous material; all the printed silver traces are coated on the surface without providing additional adhesion.

Figure 27

Cross-Sectional SEM-EDS Images of Silver Ink on (a) Paper (b) Plastic. Silver Sinks into Paper, Creating a Stronger Bond



(a)



(b)

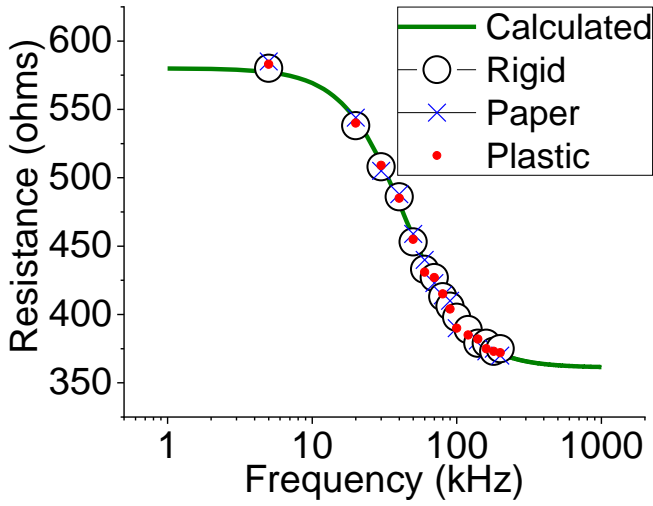
3.5.2 *Hardware Verification*

The performance evaluation of all three EBI systems is carried out using a 2R1C parallel electrical model (shown in Fig. 8) which represents biological tissues in a human body [149]. The model consists of a resistor $R_i = 1100 \Omega$ connected in series with a capacitor $C_m = 1.5 \text{ nF}$, both in parallel with a resistor $R_e = 560 \Omega$. The resistors R_i and R_e represent the intracellular and extracellular fluids, respectively, and the capacitor C_m represents the cell membrane. The analyzers are then configured to perform the measurement on the test model circuit in 20 discrete steps from 5 kHz to 200 kHz. Fig. 28a shows the calculated vs. measured resistance for all three EBI systems, while Fig. 28b shows the reactance data. The results show that all the impedance analyzers demonstrate a high accuracy with an error of less than 1% for both resistance and reactance. It is worth noting that the power consumptions of these systems vary despite their comparable electrical performance. The sensor modules developed on the paper (83.3 mW) and plastic (65.7 mW) substrates consume more power than the rigid device (53.42 mW). The difference comes from the higher resistance of the silver traces on the flexible substrates. For example, a silver trace on plastic has a resistance of $0.3 \Omega/\text{cm}$ while on paper it is increased to $0.5 \Omega/\text{cm}$.

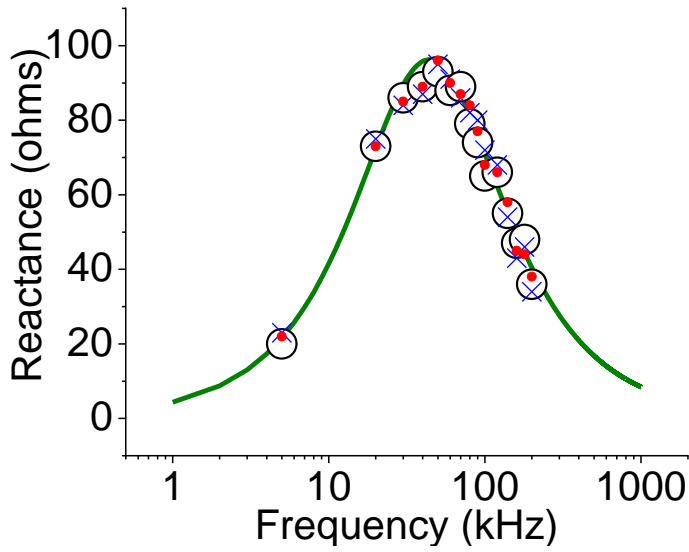
Figure 28

(a) Resistance and (b) Reactance Plots Using the 2R1C Tissue Model for Hardware

Calibration and Performance Evaluation



(a)



(b)

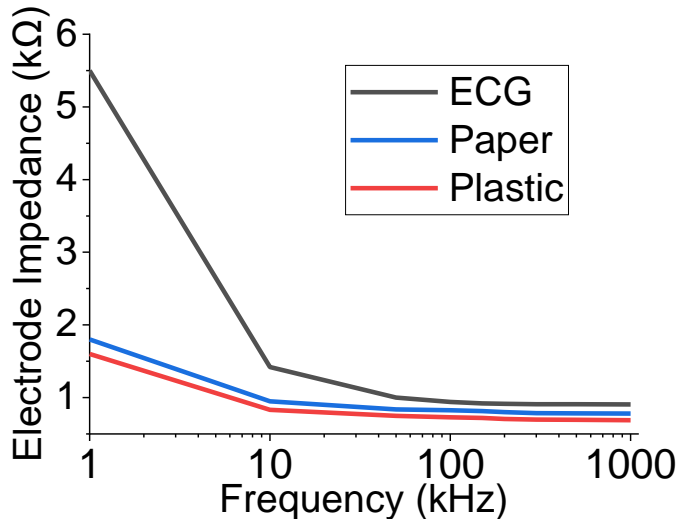
3.5.3 Electrode Characterization

Dry electrodes are more suitable for wearable medical devices due to their durability and reusability. Wet electrodes, on the other hand, are uncomfortable and sometimes cause irritation on the skin. The major challenge working with dry electrodes is that they have higher electrode-skin contact impedance, which tends to degrade the strength of the physiological signal received from the body. The contact impedance values of all three types of electrodes are measured using a previously reported three-electrode method [135]. Fig. 29a shows the contact impedance magnitude plots of gel-based Ag/AgCl electrodes (40.6 mm × 33.02 mm) as well as paper and plastic-based dry electrodes (85 mm × 50 mm). The results show that the contact impedance of the flexible dry electrodes is much smaller than that of the wet electrodes throughout the frequency spectrum, the reason being that the dry electrodes have a surface area 3.26 times larger than the wet electrodes, providing a wider path for the electrical current to go through the body [113]. Between the two flexible substrates, the paper-based electrodes demonstrate higher impedance. This is because the silver ink sinks into the fibers of the paper, hence decreasing the uniformity, thickness, and eventually the conductivity of the silver layer on the surface.

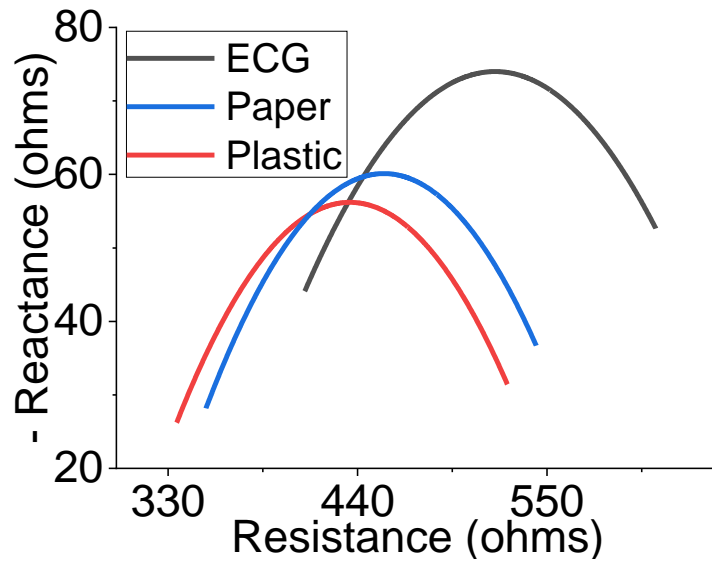
Figure 29

(a) *Electrode-Skin Contact Impedance of Dry and Wet Electrodes. (b) Bio-Impedance*

Plot of One Subject Using all Three EBI Systems



(a)



(b)

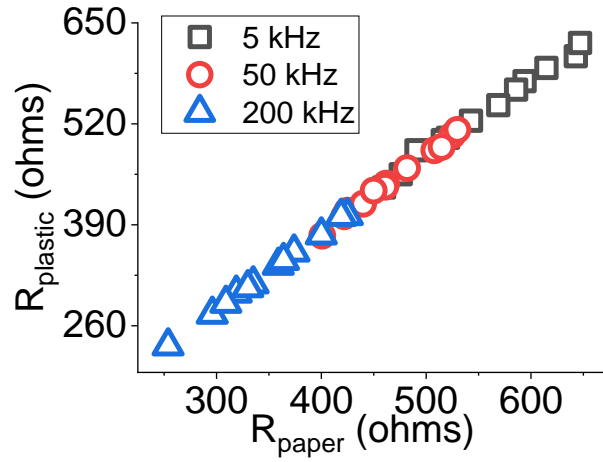
3.5.4 Bio-Impedance Measurement and Analysis

Fig. 29b shows the typical bio-impedance plots of resistance vs. reactance of the subjects, in this particular case, a 25-year-old healthy male, using the three devices. The measurement is based on the four-electrode method in order to eliminate the electrode skin contact impedance [133]. Although the four-electrode method eliminates the electrode impedance from the measurement, other problems still arise [128]. It is clear that the rigid sensor module with the Ag/AgCl electrodes shows larger values over the entire frequency range. This is because the electrical current injected from the smaller electrodes is not uniformly distributed in the biological tissues. There are selected areas of higher current densities, known as constriction zones, that contribute to the larger bio-impedance [150]. In the case of flexible sensor modules, the larger integrated electrodes can eliminate the constriction zones, resulting in more uniform distribution of the current density. Fig. 30 shows the bio-impedance data for the 12 subjects at selected frequencies using the paper and plastic based sensors. The results show that all the subjects demonstrate a similar trend of bio-impedance throughout the frequency spectrum for both paper and plastic sensor modules.

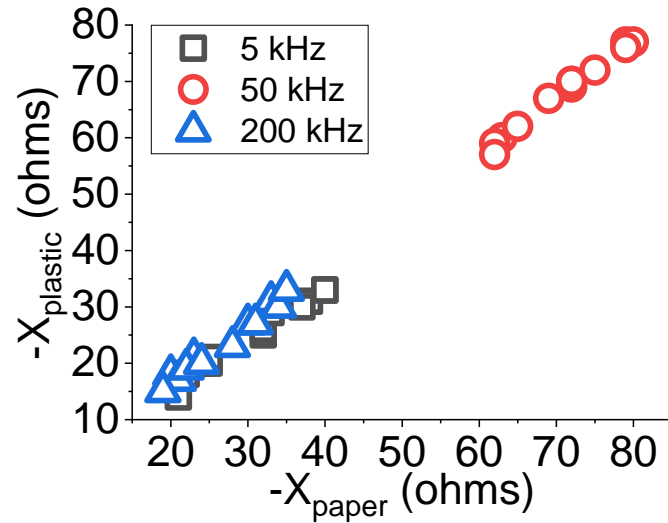
Figure 30

Bio-Impedance Analysis of 12 Subjects at Selected Frequencies Using Paper and Plastic

Sensor Module. (a) Resistance. (b) Reactance



(a)



(b)

3.6 Conclusion

In this chapter, we presented two flexible electrical bio-impedance analyzers developed on paper and plastic substrates. Both flexible analyzers exhibit comparable measurement performance to the rigid analyzer. The paper-based sensor demonstrated robust mechanical deformations while plastic-based sensor provided lower power consumption and lower electrode-skin contact impedance. The integrated dry electrodes on the flexible sensors offer a reliable method to perform repeated measurements to collect human physiological signals. Our current mechanical testing of the flexible sensors using extreme bending angles is primitive. We plan to conduct a thorough investigation of the mechanical behaviors of the flexible sensors in the near future. Our preliminary results of flexible sensors show that they have great potential for future wearable, healthcare applications.

Chapter IV

Flexible Temperature Sensor with Compensation of Bending and Stretching

4.1 Introduction

Continuous measurement of human body temperature plays a significant role in health monitoring [151]. An increase in the body temperature could be an indication of fever, which is the most important symptom of many severe diseases including COVID-19 [152]. Therefore, early detection of an increase in body temperature can help identify and quarantine infected patients before the virus spreads to other people. Furthermore, body temperature measurement can be used to monitor sophisticated cardiovascular diseases [153]. Current commercial temperature sensors lack the characteristics desired for wearable applications. An ideal wearable device should be soft, lightweight, biocompatible, and most importantly, able to adapt to non-planar skin surfaces over a large area for high-accuracy measurement. Recently, much attention has been paid to the development of flexible and stretchable temperature sensors as they can be used in a wide range of applications including health monitoring [63], robotics [154], as well as artificial electronic skin [155-157]. Flexible temperature sensors can adapt to curved or irregular surfaces, and perform long-term measurements with high accuracy and stability, as compared to conventional temperature sensors that are fabricated using silicon technology [158]. These silicon chips are rigid and usually bulky, cannot measure data with sufficient accuracy when attached to non-planar surfaces, and can be uncomfortable to wear when used in long-term wearable applications. Flexible temperature sensors are typically fabricated by depositing temperature sensitive conductors such as metals (e.g., silver [159], aluminum [160], and gold [161]), carbon-based materials (graphene, reduced

graphene oxide, carbon nanotubes (CNTs), etc.) [162, 163], or conductive polymers [46] on flexible substrates. The common substrates used to develop flexible sensors include polydimethylsiloxane (PDMS) [164], polyimide (PI) [165], polyurethane (PU) [166], and fabrics [167]. The fabrication of flexible sensors can be done through different techniques including printing (inkjet, screen, gravure, etc.), coating, and deposition techniques. Out of all these options, the selection of the substrate, deposition material, and fabrication method depends heavily on the application of the sensor.

Resistive temperature detectors (RTDs) are one of the most commonly used sensors for temperature measurement due to their simple design, fast response, high accuracy, and high linearity [168, 169]. These features make the RTDs more preferable in wearable applications in comparison to other types of temperature detectors such as thermocouples [11]. RTDs based on temperature-sensitive conductors or inks on flexible substrates have been reported [170-172]. However, the challenge with flexible RTDs is that their resistivity is not only sensitive to temperature, it also varies with mechanical deformation (e.g., bending and stretching) of the substrate. When the film is under tension, which could be caused by either bending or stretching, the effective length of the RTD is increased, resulting in an increase in resistance; while on the other hand, compression on the film leads to a decrease in resistance for the RTD. This deformation-induced resistance variation can cause significant errors in temperature measurement. To minimize this effect, flexible RTDs with stress compensation have been developed using CNTs [154], gold [173], and E-textile [167]. However, the existing techniques for stress compensation are often complex, expensive, and time-consuming. A differential compensation technique has been presented by Ali *et al.* and validated by printing silver

RTDs on polyethylene terephthalate (PET) [174]. However, the technique is only designed for bending compensation without considering the stretching effect. Therefore, new compensation techniques should be developed to accommodate the complex mechanical deformation conditions.

In this chapter, we present a novel, low-cost, and simple flexible temperature sensor that provides compensation to resistance changes caused by both bending and stretching. The sensor, made of two RTDs, is easy to fabricate and does not require complicated methods or tools. It can measure the temperature on a curved or irregular surface with minimum errors as compared to conventional RTDs. The sensor is interfaced with a Bluetooth-integrated microcontroller, which is programmed to detect the physical change of the sensor (bending or stretching), provide compensation against mechanical deformation, and quantify the temperature with high accuracy. The following sections of this chapter describe the compensation methodology, fabrication process, system architecture, and experimental results of the wearable flexible temperature sensor.

4.2 Methodology

Fig. 31 illustrates the methodology used for compensating for the mechanical deformation. The sensor configuration consists of two RTDs which are fabricated back-to-back on both sides of the substrate through stencil printing. The pattern printed on the top side is labeled as RTD_1 and the one on the bottom side is RTD_2 . Silver paste is used to print RTD patterns on the PDMS substrate. When the sensor is bent on a curved surface, the RTD facing outward experiences tension, as the average gap between the silver particles in the printed pattern increases. This causes an increase in electrical resistance of the RTD. On the other hand, the RTD that is bent inward faces compression

and the gap between the silver particles decreases, leading to a reduction in resistance. Upon sensor bending in either direction, the sum of the measured resistance of both RTDs remaining almost a constant, with one RTD observing $+\Delta R$ whereas the other RTD observing $-\Delta R$. Therefore, the resistance variations caused by bending can be canceled out using this design. The sum of resistance, R_{sum} , is calculated using Equation (10) with the initial resistances normalized for the two RTDs.

$$R_{sum} = \frac{\Delta R_1}{R_1} + \frac{\Delta R_2}{R_2} = \frac{R'_1 - R_1}{R_1} + \frac{R'_2 - R_2}{R_2} \approx 0 \quad (10)$$

where R_1 and R_2 represent the initial values of the RTD₁ and RTD₂, respectively. R'_1 and R'_2 are the resistance values of the RTDs after the sensor is mechanically deformed. With the compensation for bending in place, the resulting change in the sum of resistance is only caused by a change in temperature, regardless of the *bending* status of the substrate.

When a sensor is stretched, its length L increases, and the cross-sectional area A decreases. Thus, the resistances of both RTDs will increase according to $R = \rho L/A$. In cases where conductive adhesives (instead of pure metals) are used as the sensor elements, this increase in resistance can also be caused by other factors such as the change in resistivity ρ and grain connections within the cured adhesive when the sensor is stretched. If both RTDs are stretched equally, they will experience a comparable amount of tension with a similar resistance change of $\Delta R_1 \approx \Delta R_2$. Therefore, the subtraction of resistances of the two RTDs, R_{sub} , is almost zero under stretching, as expressed in Equation (11).

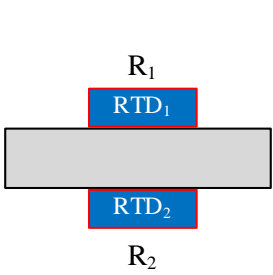
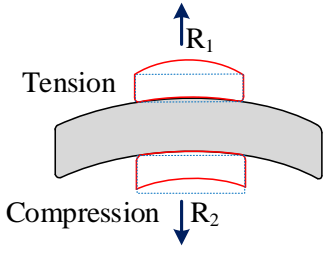
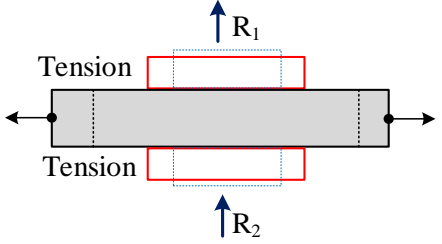
$$R_{sub} = \left| \frac{\Delta R_1}{R_1} - \frac{\Delta R_2}{R_2} \right| = \left| \frac{R'_1 - R_1}{R_1} - \frac{R'_2 - R_2}{R_2} \right| \approx 0 \quad (11)$$

With this second compensation, analogous to the bending compensation, a change in R_{sub} can only be caused by a change in temperature, regardless of the *stretching* status of the substrate.

When used for temperature sensing, the physical state of the sensor, whether it is under bending or stretching, should be determined automatically without needing the direct input from the user. This can be done by using algorithms to monitor the trends of resistance change of both RTDs. A detailed explanation is provided in Section 4.6.

Figure 31

Compensation Methodology

Flat	Bending	Stretching
		
$R_1 \approx R_2$	$\Delta R_1 \approx -\Delta R_2$ $\Delta R_1 + \Delta R_2 \approx 0$	$\Delta R_1 \approx \Delta R_2$ $\Delta R_1 - \Delta R_2 \approx 0$

Note. While bending the sensor, the resistances of both RTDs change differentially; therefore, the sum of resistances remains a constant. When stretching the sensor, the

resistances of both RTDs change linearly, hence, the subtraction of resistances is almost zero. $R_1 \approx R_2$ is used here for the purpose of simplification.

4.3 Sensor Fabrication

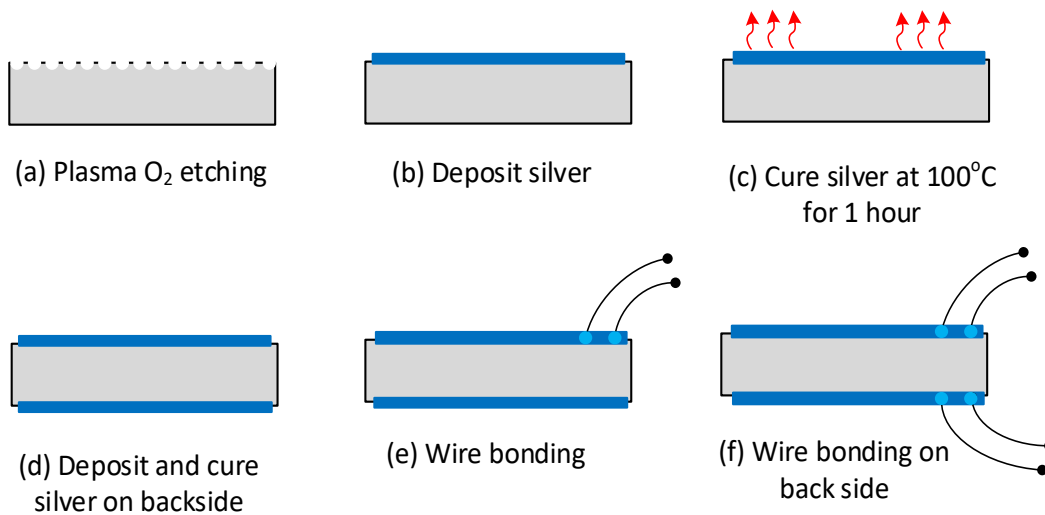
Fig. 32 shows the detailed fabrication process of the designed sensor. PDMS is used as the flexible substrate for the RTD sensor due to its flexibility, stretchability, and excellent electrical and thermal insulation properties. Initially, a PDMS solution was prepared by mixing a 5:1 ratio of the base polymer and the curing agent. The solution was then coated on a 4-inch silicon wafer using a spin coating machine, set as 150 rpm for 30 s. The coated silicon wafer was then baked at 100°C for 30 min until the PDMS solution solidified.

The ability of a substrate to anchor silver is determined by its surface energy. Pristine PDMS is hydrophobic with low surface energy, leading to relatively weak bonding between the substrate and the silver paste used for the wires. To increase adhesion, O₂ plasma etching was performed on the PDMS with 100 W power at a pressure of ~500 torr for 3 min. Afterward, silver epoxy from MG chemicals (9410) was used to print the RTD structures on the PDMS substrate via stencil printing. Stencil printing (or screen printing) methodology adds simplicity, speed, adaptability, and low cost to the manufacturing process. It is faster and more versatile than other printing tools [175]. The main requirement for stencil printing is that the printable paste should have a high viscosity so it does not spread out easily after being printed. The chosen silver is a thixotropic paste with a high viscosity due to the presence of additives. It is a 1-part

adhesive that can be cured at 100°C for 1 hour after being printed. Afterward, the wires are bonded to the RTD electrodes using the same silver epoxy, resulting in low contact resistance. A similar RTD is developed on the opposite side of the PDMS using the same process.

Figure 32

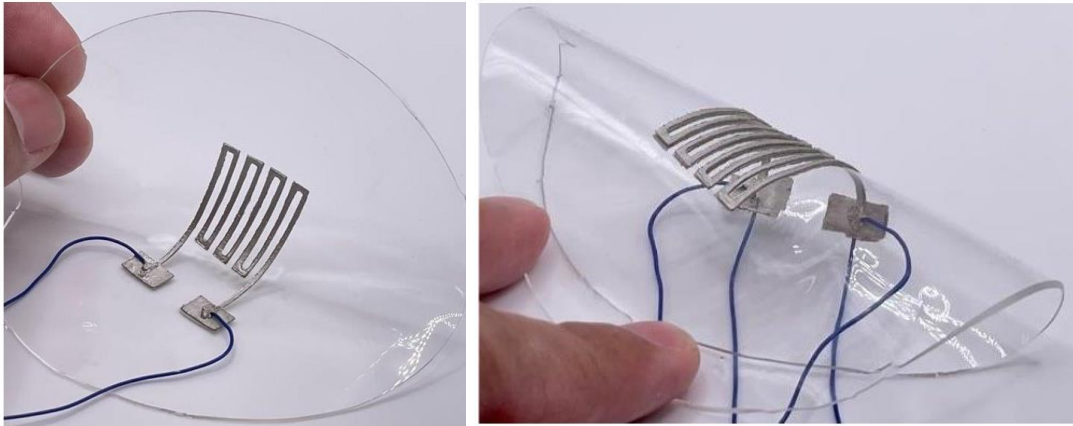
Fabrication Process of RTD Structures Using Stencil Printing and Silver Paste



The fabricated temperature sensors on PDMS are shown in Fig. 33, with each sensor containing two identically shaped RTDs. The RTD has an overall dimension of 37 mm × 19 mm and consists of a 1-mm wide meander trace for the resistive element. The thickness of the meander trace is approximately 0.2 mm. The electrode pads of the RTDs are bonded to 30 AWG connecting wires to provide a connection for the external interface.

Figure 33

Photograph of the Fabricated RTD Sensors



(a)

(b)

Note. (a) Front RTD printed on PDMS by depositing silver paste using a stencil mask.

Wires bonded on the pads using the same silver adhesive. (b) Identical RTD fabricated on the back side of the substrate.

4.4 Hardware Architecture

Fig. 34 shows the overall architecture of the designed system. The flexible sensors are interfaced with a controller module via 30AWG wires. A Bluno Beetle board is used as the controller module which contains built-in Bluetooth (2.4 GHz) and an ATmega 328p microcontroller working at a maximum frequency of 16 MHz. Each RTD is connected to a known resistor to create a voltage divider with a source voltage applied across them. A 3.7 V rechargeable lithium-ion polymer (LiPo) battery is used to power the microcontroller and provide the source voltage to the voltage divider circuit. The

microcontroller measures the voltage across the known resistors and the flexible RTDs using a built-in ADC converter. The resistances of both RTDs, R_1 and R_2 , can be calculated using the following equations:

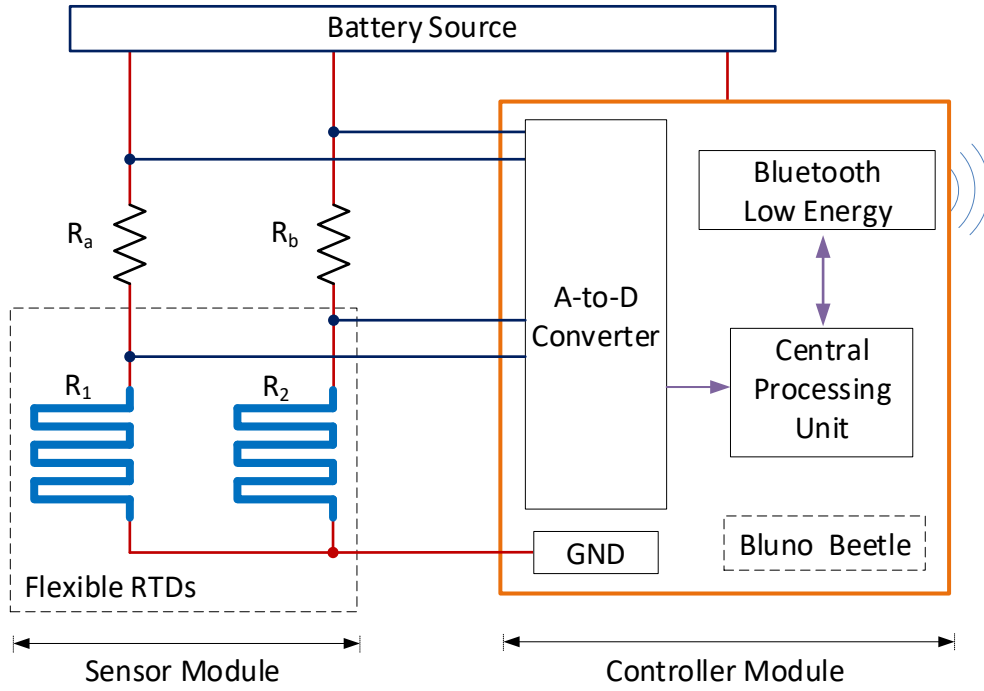
$$R_1 = \frac{R_a \times V_1}{V_a} \quad (12)$$

$$R_2 = \frac{R_b \times V_2}{V_b} \quad (13)$$

where V_1 and V_2 are the voltages across the flexible RTDs, R_a and R_b are the known reference resistors, and V_a and V_b are the voltages measured across these known reference resistors.

Figure 34

Block Diagram of the Designed Temperature Measurement System



Note. The system consists of two main parts, the flexible sensor module and the controller module.

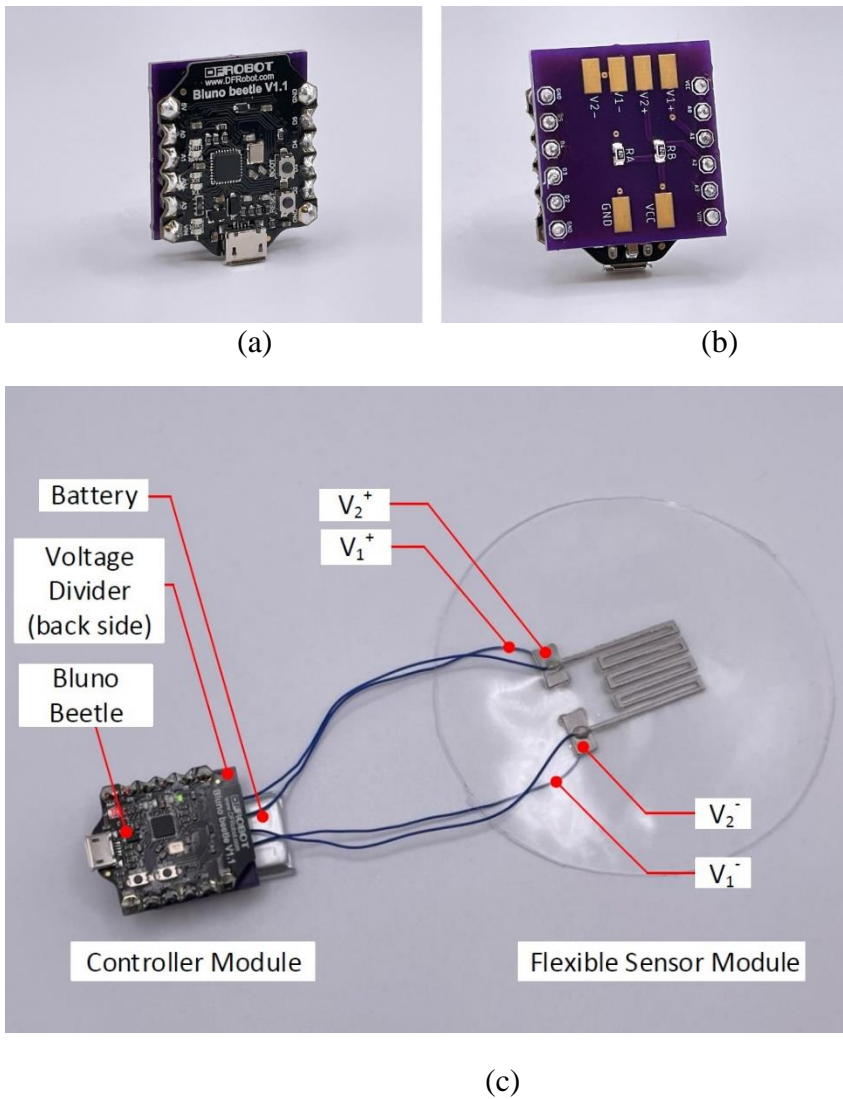
Based on the computed values of R_1 and R_2 , the microcontroller determines the physical state of the sensor, provides necessary compensation for the mechanical deformation, and quantifies the temperature accordingly. The data can be transmitted wirelessly to a connected smartphone or a computer via Bluetooth. Further explanation is provided in the next section. Photographs of the complete device are shown in Fig. 35.

After fabrication and connection to the controller module, each flexible sensor module is characterized through a series of controlled measurements to (1) quantify the

effects of bending and stretching on temperature sensing, (2) use proper methods to compensate for these effects, and (3) implement a post-data-collection correction step, labeled as calibration, to accommodate the variations from devices and testing.

Figure 35

Photographs of the Complete System



Note. (a) Bluno Beetle is used as the controller module. (b) Voltage divider circuit board attached to the back side of the controller module. (c) The controller module interfaced with the flexible sensor module.

4.5 Experiments, Results, and Discussion

4.5.1 Temperature Quantification while Bending the Sensor

In the initial quantification process, the sensor module is kept on a flat surface and the initial resistances of RTD₁ and RTD₂ are measured. Afterward, the sensor module is bent at different curvatures using 3D printed half cylinders with various radii, ranging from 100 mm to 40 mm. Fig. 36 shows the experimental setup to test the sensor for bending, which is carried out at room temperature of ~20°C. The resistance depends on the bending radius, as shown in Fig. 37. Since both RTDs are aligned on the two sides of the substrate with a nearly identical sensor pattern, their resistances should change differentially ($\frac{\Delta R_1}{R_1} \approx -\frac{\Delta R_2}{R_2}$). It is observed that the sum of resistance can successfully compensate for the bending effect when compared to the individual RTDs, reducing the deformation-induced resistance change $\Delta R/R$ from 30.1% (black line, for RTD₁) and -22.5% (green line, for RTD₂) to 8.5% (red line, R_{sum}) under the most significant bending.

However, the compensation does not completely remove the bending effect. The non-zero readings of R_{sum} are considered as errors which may be caused by three readily identifiable factors. First, the two RTDs are not 100% identical in terms of conductivity and dimensions with differences resulting from the manual fabrication process. Second, there may be a stress difference on the two RTDs due to the off-center neutral plane when

the substrate is deformed by bending. Third, there may be a small temperature difference on the two RTDs during testing. The RTDs' self-heating under the applied voltage and their different heat dissipation rates, as one RTD is exposed to air while the other is trapped between the half cylinder and PDMS, lead to the temperature difference. The power dissipation ($P = I^2R$) across the top RTD is about 27% higher (due to the increased resistance) than the bottom RTD when the sensor is bent on the curvature of 40 mm. The higher power dissipation causes a higher self-heating effect which contributes to a greater increase in the resistance value of the top RTD.

Therefore, post-data correction, or calibration, is required to reduce the importance and influence of these errors. The calibration is performed by introducing an adjustment factor X, which is calculated using the following equations:

$$\left(\frac{\Delta R_1}{R_1}\right)_{40mm} + X \cdot \left(\frac{\Delta R_2}{R_2}\right)_{40mm} = 0 \quad (14)$$

$$X = -\frac{\left(\frac{\Delta R_1}{R_1}\right)_{40mm}}{\left(\frac{\Delta R_2}{R_2}\right)_{40mm}} \quad (15)$$

where $(\Delta R_1/R_1)_{40mm}$ and $(\Delta R_2/R_2)_{40mm}$ are the relative resistance changes of the two RTDs at the bending curvature of 40 mm. With the calibration applied, the errors can be effectively reduced, as shown by the blue line in Fig. 37. The calibration method is

further validated by repeating the experiment 5 times, and the results show that the maximum bending error is reduced from $8.1 \pm 1.1\%$ to $2 \pm 0.7\%$. This shows that the effect of mechanical deformation due to bending can be significantly reduced by combining compensation and calibration, and the device can now be used to perform temperature measurements under deformation with higher accuracy.

Figure 36

The Bending Experiment is Performed by Placing the Sensor on Cylinders with Varying Radii Ranging from 100 mm to 40 mm

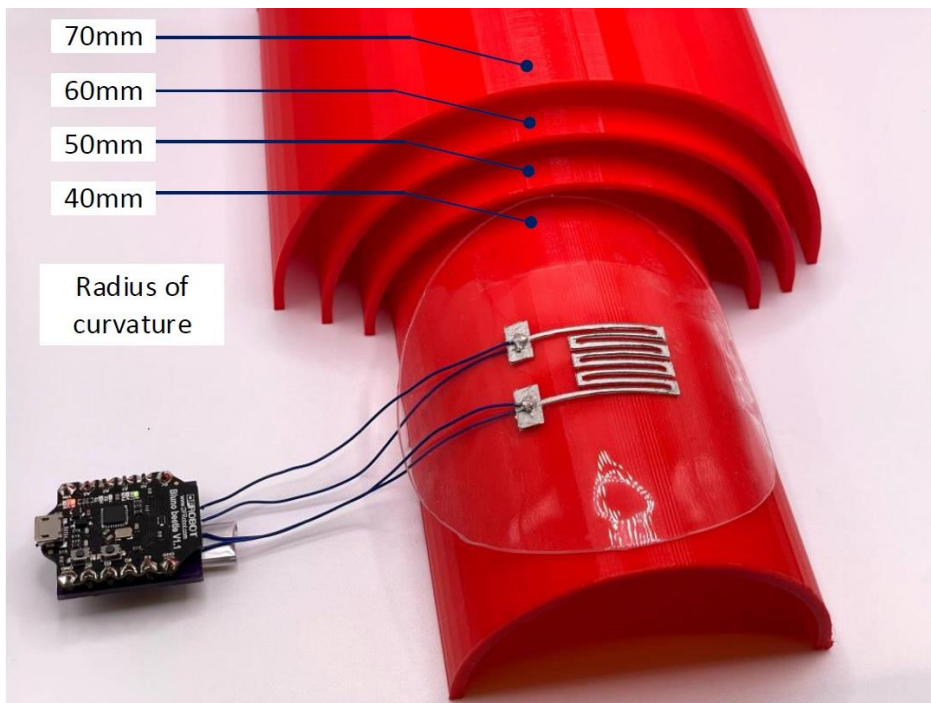
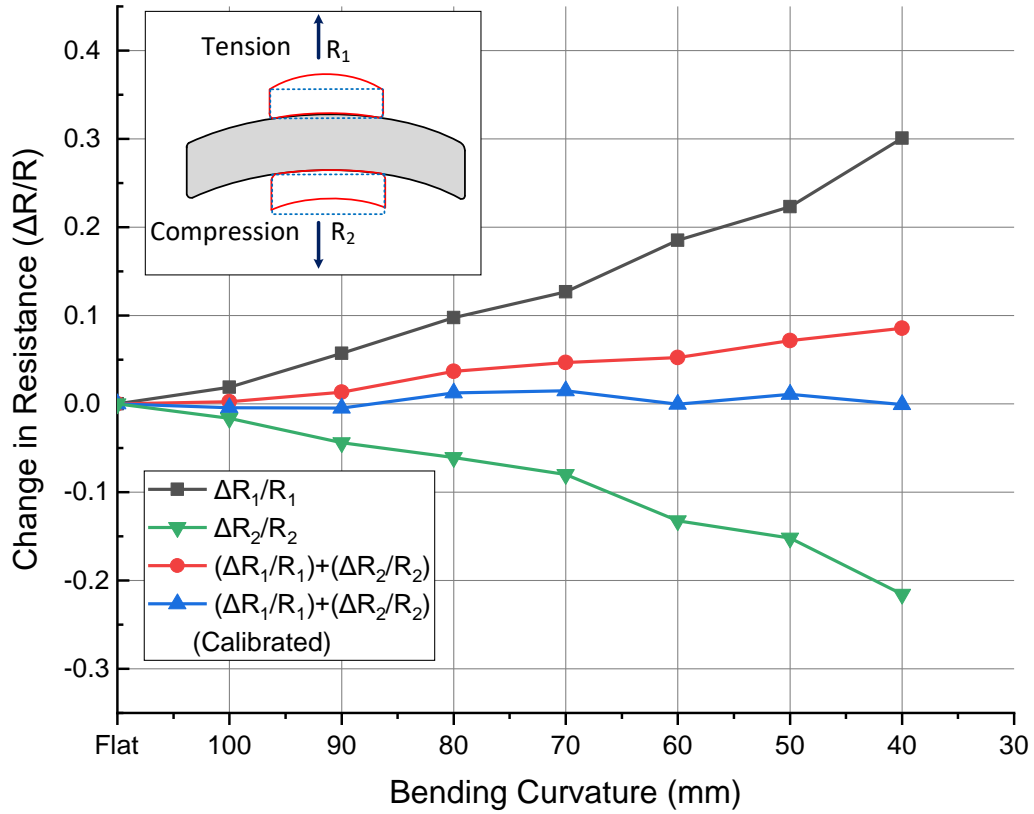


Figure 37

Analysis of Changes in Resistance While Bending the Sensor



Note. When the sensor is bent on a curved surface, the resistance of RTD₁ (black line) increases due to tension and the resistance of RTD₂ (green line) decreases due to compression. The sum of resistance (red line) can reduce the effect of bending and the remaining errors can be minimized by calibration (blue line).

The baseline temperature sensing characteristic of the RTDs is determined by heating the sensor on a flat surface. A flexible heater (by ICSTATION) is used to control the temperature applied to the sensor from 20°C to 40°C with increments of 5°C. Each

set temperature was maintained for 10 min to allow the heated environment to reach thermal equilibrium before RTD resistances are recorded. A reference temperature sensor SEN-13314 (by SparkFun) is used to confirm the temperature reading of the heater. Fig. 38 shows the baseline resistive response of the flexible RTDs as a function of temperature. As the temperature increases, the resistances of both RTDs become higher, demonstrating the temperature dependence of electrical resistance characteristic of a metal in the deposited silver epoxy. When the temperature is increased to more than 40°C, the PDMS substrate experiences significant thermal expansion which disturbs the linearity of the resistance vs. temperature curve. Therefore, the temperature range is limited between 20°C to 40°C, which is sufficient for most wearable applications of temperature sensing on human skin.

The sensitivity of the 2-RTD-based sensor within this given temperature range is defined by the temperature coefficient of resistance (TCR_{sum}) using the equation [176]:

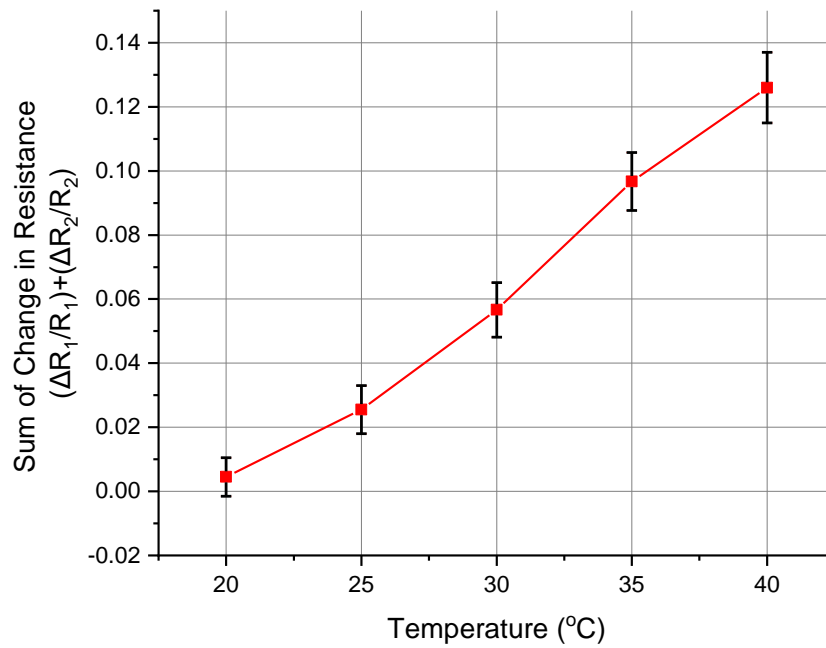
$$TCR_{sum} = \frac{R_{sum(40^{\circ}C)} - R_{sum(20^{\circ}C)}}{\Delta T} = 5.9 \times 10^{-3} /^{\circ}C \quad (16)$$

where $R_{sum(40^{\circ}C)}$ is the sum of change in resistance at 40°C, $R_{sum(20^{\circ}C)}$ is the sum of change in resistance at 20°C, and ΔT is the difference between the final and initial temperatures, i.e., 20°C. The TCR of the designed RTD is measured to be higher than that of the pure Ag metal because the sensor is developed on a PDMS substrate. PDMS exhibits a large coefficient of thermal expansion of about 310 ppm/°C. Therefore, PDMS is sensitive to the temperature changes during the measurement. In a heated environment,

the thermal expansion of the PDMS substrate contributes towards the increase in resistance [177, 178], in addition to the silver pattern's own resistance change, leading to the higher TCR.

Figure 38

Sum of Change in Resistance of the Sensor Versus Temperature from 20°C to 40°C



Note. The TCR is calculated as $5.9 \times 10^{-3} / ^\circ\text{C}$ by using linear curve fitting.

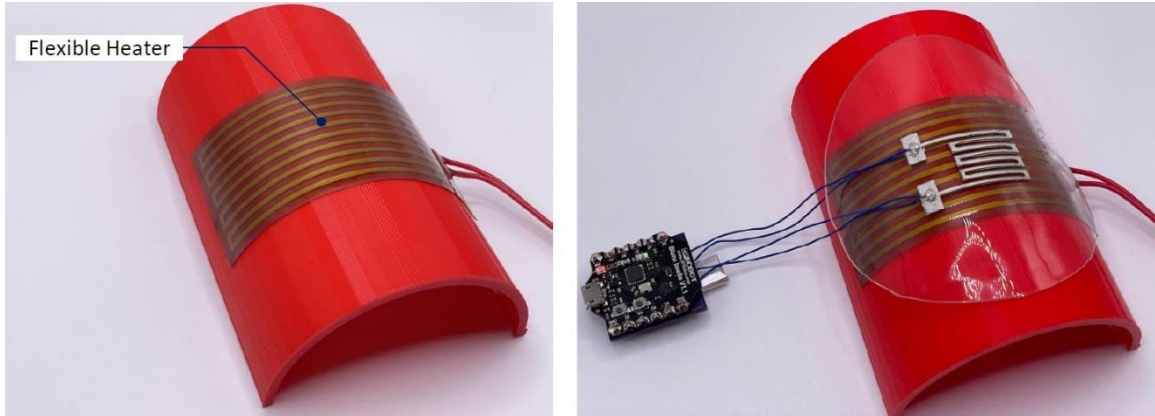
The resistive response of the flexible sensor against temperature is then investigated by varying the temperature while bending the sensor. Fig. 39 shows the experimental setup, where the heater is placed between the sensor and the 3D printed

curvature such that the RTD₂ comes in direct contact with the heater. During the measurement, the heater is placed on all the half cylinders one by one, and for each cylinder, the temperature is changed from 20°C to 40°C with a temperature increment of 5°C with the RTDs' resistances recorded at each point.

Fig. 40 shows the analysis of the sensor performance when both heating and bending are considered. The z-axis represents the overall measurement error, which is calculated by comparing the recorded resistance against the theoretical value using TCR_{sum} , at a specific combination of temperature and bending radius. If the measurements are performed using only a single RTD (e.g., RTD₁), the resistance will increase due to the mechanical stress as well as heating (red plane). A maximum error of 32% is observed when the RTD is tested at a temperature of 40°C with a bending radius of 40 mm. When both RTDs are used and the bending compensation methodology is applied, the maximum error is reduced to 9.6% (cyan plane). After post-data calibration to accommodate the variations from devices and testing is implemented, the measurement errors are further minimized (blue plane) with a maximum error of approximately 2%.

Figure 39

Experimental Setup for Heating and Bending the Sensor



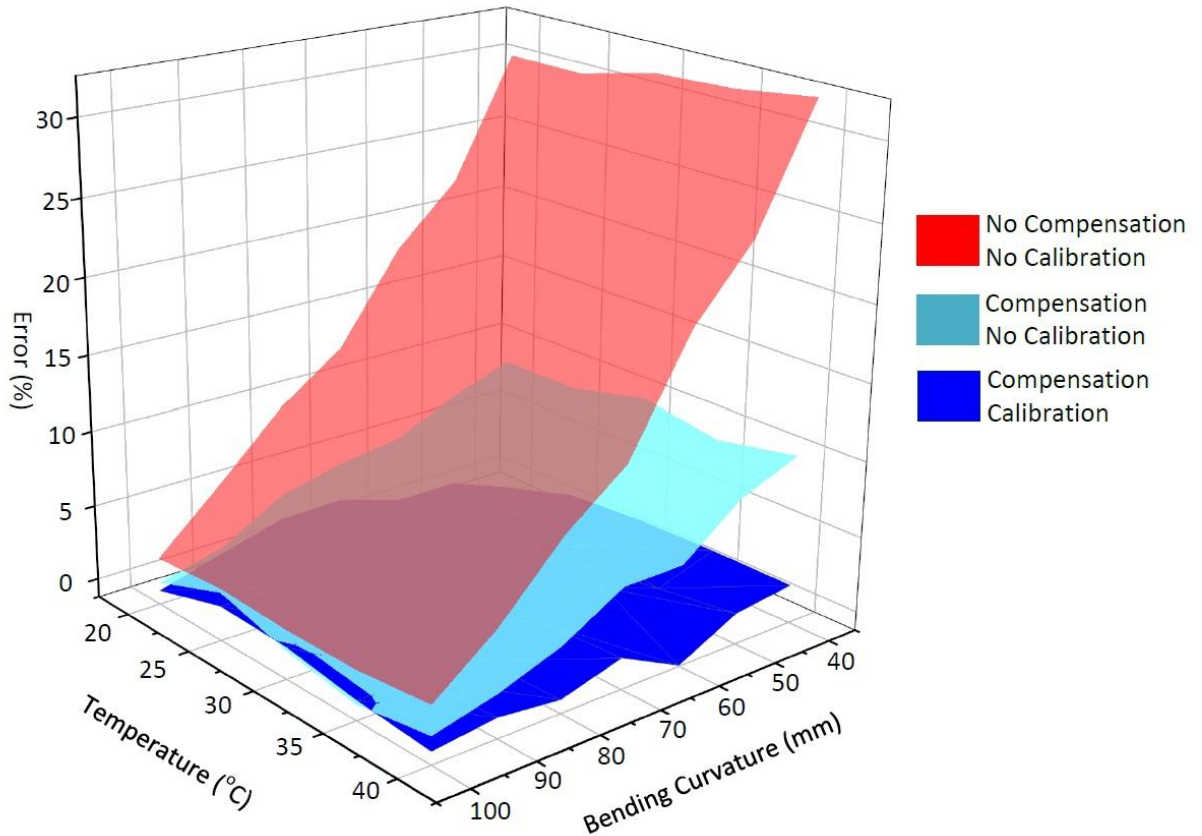
(a)

(b)

Note. (a) Flexible heater placed on the 3D printed half cylinder. (b) Sensor device placed on the heater such that the RTD_2 comes in contact with the heater and RTD_1 is exposed to air.

Figure 40

Analysis of Resistance Measurement Errors When the Sensor is Under Heating and Bending at the Same Time



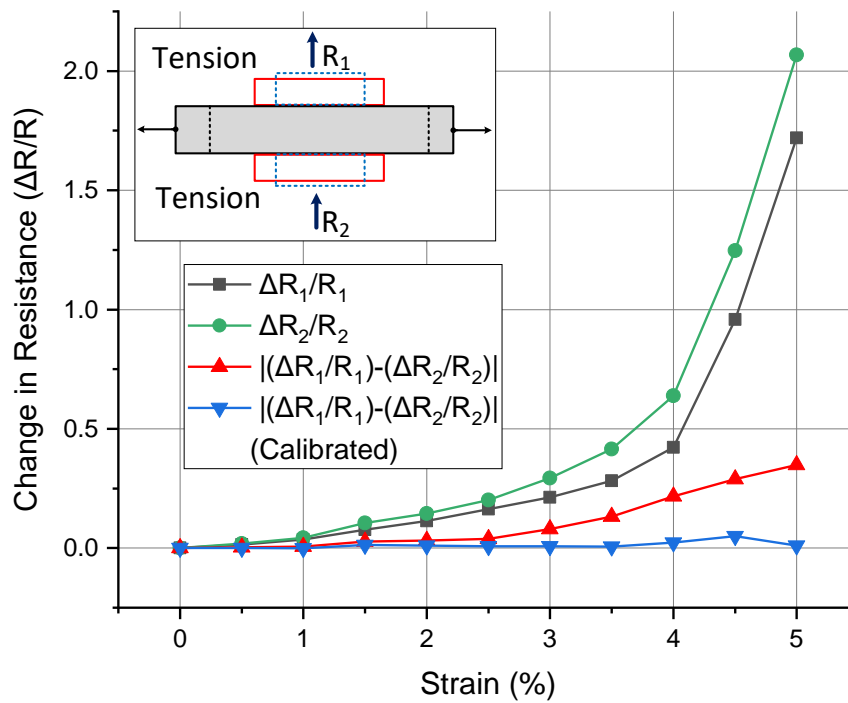
4.5.2 Temperature Quantification while Stretching the Sensor

In order to evaluate the influence of stretching, a tensile testing machine (from SHIMADZU) is used. In the tensile testing instrument, the sensor is clamped at both ends and stretched uniaxially with increments of 1 mm. At each increment, the resistance changes of both RTDs are measured using the microcontroller module.

When the sensor is stretched, both RTDs experience tension which increases their resistances, as shown in Fig. 41. The maximum resistance changes of RTD₁ and RTD₂ are measured as 172% (black line) and 206% (green line), respectively. These errors can be reduced to 34% by using the linear compensation method (red line, R_{sub}) described in Section 4.2. With the calibration applied, the measurement errors can be further minimized (blue line). In addition, after calibration, the sensor demonstrates very low errors when the strain is under 3%.

Figure 41

Analysis of Resistance Changes While Stretching the Sensors



Note. When the sensors are stretched, the resistances R₁ (black line) and R₂ (green line)

increase as both RTD₁ and RTD₂ face tension. Compensation (red line) and calibration (blue line) are performed to reduce the reading errors.

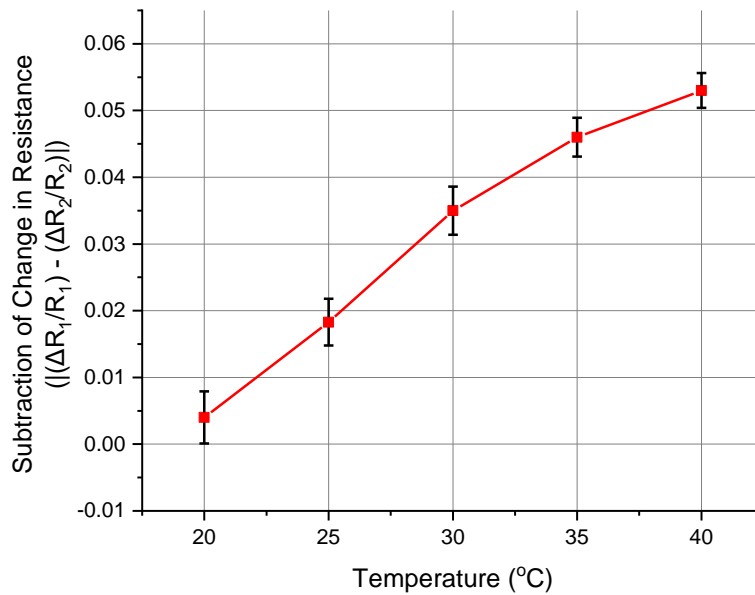
For the 2-RTD-based sensor, the subtracted values of the change in resistance as a function of temperature is shown in Fig. 42. The TCR_{sub} is calculated using the equation:

$$TCR_{sub} = \frac{R_{sub(40^{\circ}C)} - R_{sub(20^{\circ}C)}}{\Delta T} = 2.5 \times 10^{-3} /^{\circ}C \quad (17)$$

where $R_{sub(40^{\circ}C)}$ and $R_{sub(20^{\circ}C)}$ are the measured R_{sub} values at 20°C and 40°C, respectively, and $\Delta T = 20^{\circ}C$. The value of TCR_{sub} is smaller than TCR_{sum}. This is because TCR_{sum} is calculated by the addition of both RTDs while TCR_{sub} is based on subtraction using values from the two RTDs.

Figure 42

Subtraction of Change in Resistance of the Sensor Versus Temperature from 20°C to 40°C

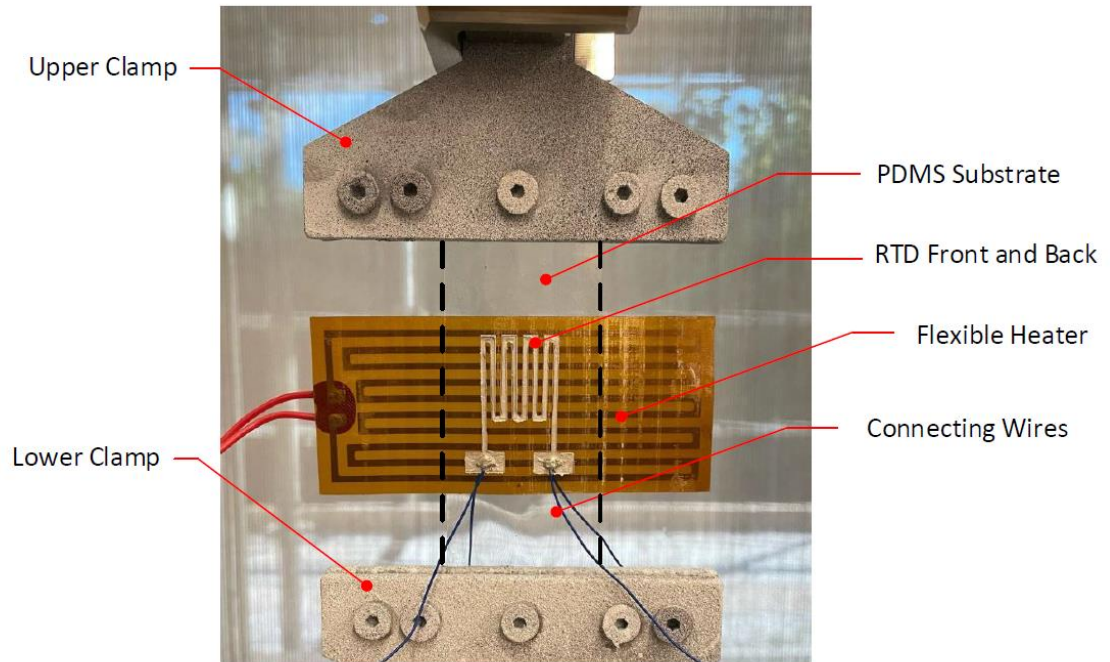


Note. The TCR is calculated as $2.5 \times 10^{-3} / ^\circ\text{C}$ by using linear curve fitting.

The sensor module is then analyzed by varying the temperature and stretching the substrate at the same time, with the experimental setup shown in Fig. 43. The sensor is heated up to 40°C as well as stretched to a 4% strain. Fig. 44 shows the analysis of the sensor performance when both heating and stretching are considered. The measurement errors of a single RTD (red plane) can be effectively reduced by the subtraction compensation method (cyan plane) and then by the calibration method (blue plane).

Figure 43

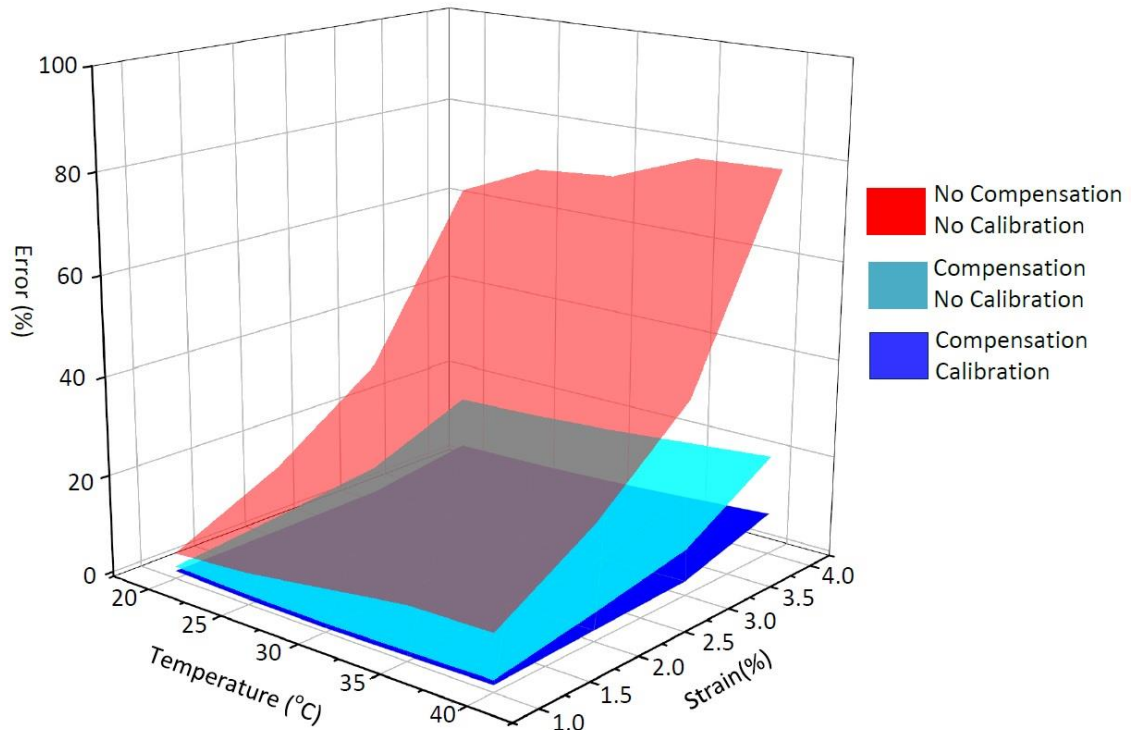
Experimental Setup for Heating and Stretching the Sensor



Note. The sensor is mounted on a tensile tester and the back pattern RTD₂ is attached to a flexible heater.

Figure 44

Analysis of Resistance Measurement Errors when the Sensor is Under Heating and Stretching at the Same Time



4.6 Physical State Determination

While performing measurements in real-time, the microcontroller needs to determine whether the sensor is being bent or stretched. This is a compulsory step since only after the determination of the physical state can the device apply the correct algorithm and result in an accurate measurement of the temperature.

Fig. 45 shows the step-by-step analysis for the microcontroller to determine the physical state of the sensor before it can apply the necessary compensation technique and

measure the temperature. When the sensor is bent upward, the resistance R_1 increases due to tension and R_2 decreases due to compression, thus, the two RTDs change differentially ($\Delta R_1 \approx -\Delta R_2$). The changes in resistance due to these tensile and compressive forces are represented by the black arrows (upward means increasing and downward means decreasing). The length of the arrow represents the amount of resistance change. Similarly, when the sensor is stretched, both R_1 and R_2 increase due to tension, thus, the two RTDs change linearly ($\Delta R_1 \approx \Delta R_2$). When heating is introduced, RTD₂ experiences an increase in R_2 as it is in direct contact with the heat source. Next, the heat propagates through the substrate and also causes an increase in R_1 . The red arrows represent the resistance increases of both RTDs due to increased thermal energy, and the length of each arrow represents the amount of resistance increase.

Step 1 (Initial Conditions): In order to determine if the sensor is undergoing bending or stretching, the trend of resistance change is used by comparing the most recent resistance value of each RTD with its previously recorded value. The resistance trends of both RTDs will be examined together to help the microcontroller determine the sensor's deformation status, e.g.,

- R_1 increasing and R_2 decreasing = Bending
- Both R_1 and R_2 increasing = Stretching

However, this comparison and its conclusions are valid only when temperature is not a factor. If temperature is considered, the situation is much more complicated because both the temperature and the mechanical deformation can change the resistance values. For example, a compressed RTD in a heated environment may show an increased ($R'_2 > R_2$) or decreased ($R'_2 < R_2$) resistance, depending on the combined effect of the two factors.

Using the initial condition alone is not sufficient to determine the actual physical state of the sensor. Therefore, another condition, a so-called comparative condition, needs to be applied.

Step 2 (Comparative Conditions): The resistance changes of the two RTDs, ΔR_1 and ΔR_2 , are compared against each other. The Step 2 graph in Fig. 45 illustrates the change in resistance (ΔR) vs. temperature (T) for the two RTDs. The resistance changes of RTD₁ and RTD₂ are represented by the blue and green dotted lines, respectively. In the scenario where bending takes place, the starting value of ΔR_1 (a positive value) will be higher than that of ΔR_2 (a negative value). As the temperature increases, both R_1 and R_2 will increase. However, the comparative condition of $\Delta R_1 > \Delta R_2$ will remain valid within a reasonable temperature range. Therefore, it can be used by the microcontroller to determine that the sensor is under both bending and heating.

Similarly, a comparative condition of $\Delta R_1 < \Delta R_2$ can be used for the scenario of stretching and heating the sensor. In this case, the thermal insulation property of the substrate, no matter how thin, is considered. Since RTD₂ is in direct contact with the heating source, its actual temperature will be higher than that of RTD₁, as there is an inevitable temperature gradient across the substrate when the outer sensor is exposed to air. Consequently, the change of resistance of R_2 , ΔR_2 , will always be greater than that of R_1 , ΔR_1 , and the condition $\Delta R_1 < \Delta R_2$ can be used by the microcontroller to determine that the sensor is under stretching deformation. It is also worth noting these comparative conditions are valid when the sensor is being cooled down.

Step 3 (Compensation): After the physical state of the sensor is determined, the next step is to apply the necessary compensation equations. If the sensor is undergoing bending, the differential compensation equation using R_{sum} should be applied; if the sensor is undergoing stretching, the linear compensation equation using R_{sub} should be applied. These compensation techniques, along with the calibration adjustment factor X , will reduce the mechanical stress-induced effects on RTDs to a small tolerable value, and any change in the value of R_{sum} and R_{sub} will only be caused by a temperature change.

Step 4 (Applying TCR): Once the stress effects are removed, the sensor can then be used to quantify the temperature by using the appropriate TCR for each condition. In particular, the actual temperature can be calculated using one of the two equations:

$$T = \frac{R_{sum(T)} - R_{sum(20^{\circ}C)}}{TCR_{sum}} + 20^{\circ}C \quad (18)$$

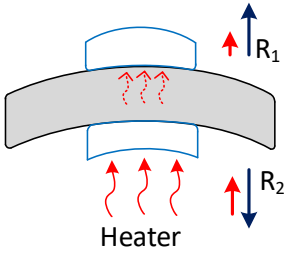
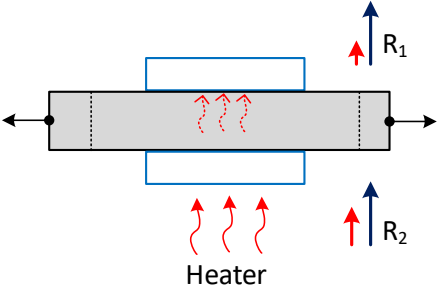
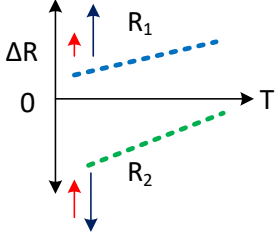
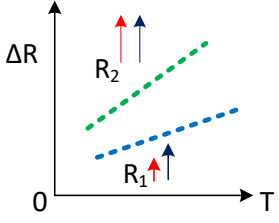
$$T = \frac{R_{sub(T)} - R_{sub(20^{\circ}C)}}{TCR_{sub}} + 20^{\circ}C \quad (19)$$

The designed temperature sensor is tested to provide compensation against bending and stretching effects. However, the sensor is only tested under a controlled environment in a clean research space. The measurement results may vary if the device is used in a harsh condition with other environmental factors such as high temperature, humidity, and pollutants. In addition, there are some measurement limitations for the current design. For example, the compensation methodology can provide reliable measurement for a maximum radius of 40 mm when the sensor is bent or a maximum

strain of 3-5% when it is stretched based on our data. The device performance under additional bending or stretching, or even more complex deformations (e.g., bending + stretching, twisting, etc.), needs to be further investigated. The developed flexible sensor can measure the temperature up to 40°C, after which the PDMS substrate expands substantially due to its high coefficient of thermal expansion and the temperature sensor demonstrates a nonlinear behavior [179, 180]. Last, the device can be used as a smart wearable sensor for body temperature measurement as the normal body temperature is 37°C (98.6°F). With a nominal operating range of 20-40°C, the current sensor can be used to detect normal fever (> 38.3°C) and hypothermia (< 35°C). However, the sensor might not be able to measure the temperature reliably during hyperpyrexia (> 40°C) [181-183]. Some of these limitations as well as their potential solutions (e.g., other polymer substrates with enhanced thermal stability) will be explored in our future research.

Figure 45

Step-By-Step Analysis to Determine the Physical State of the Sensor, Apply the Necessary Compensation Technique, and Determine the Temperature Using the Sensor

Bending + Heating	Stretching + Heating
	
$R'_1 > R_1$ $R'_2 < R_2$ (Low Temp) $R'_2 > R_2$ (High Temp)	<p style="text-align: center;">Step 1 Initial Conditions</p> $R'_1 > R_1$ $R'_2 > R_2$
<p style="text-align: center;">$\Delta R_1 > \Delta R_2$</p> 	<p style="text-align: center;">$\Delta R_1 < \Delta R_2$</p> 
$R_{sum} = (\Delta R_1 / R_1) + X \cdot (\Delta R_2 / R_2)$	<p style="text-align: center;">Step 3 Compensation Equations</p> $ R_{sub} = (\Delta R_1 / R_1) - X \cdot (\Delta R_2 / R_2) $
$TCR_{sum} = 5.9 \times 10^{-3} / ^\circ C$	<p style="text-align: center;">Step 4 Temperature Coefficient of Resistance</p> $TCR_{sub} = 2.5 \times 10^{-3} / ^\circ C$

4.7 Conclusion

In this work, a novel flexible temperature sensor that could provide compensation against mechanical deformations and measure the temperature with high accuracy was fabricated and characterized. The sensor was tested for bending by using 3D printed curvatures with radii ranging from 100 mm to 40 mm. It was observed that even before calibration, the dual RTD configuration was able to reduce the bending-induced resistance change from 30.1% (from a single RTD) to 8.5%. The bending error was further reduced to 2% after calibration was performed. To evaluate the influence of stretching, the sensor was clamped to a tensile testing machine and stretched uniaxially with increments of 1 mm up to a total of 5% strain, a value that significantly exceeds most found in wearable applications. The sensor was able to provide reliable measurements with very low errors up to a 3% strain. The temperature sensitivity of the sensor was determined by using a flexible heater. The developed sensor demonstrated a linear response within a temperature range of 20°C to 40°C. Last, the characterization of the sensor under both temperature variation and mechanical deformation demonstrated that the dual RTD configuration could effectively remove the influence from substrate bending/stretching and measure the temperature reliably. The methodology reported here is effective, novel, and easy to implement. It can be readily adopted by other flexible sensor designs to provide accurate temperature measurement. The devices that have deformation compensation in place will have great potential for a variety of wearable applications.

Chapter V

Conclusions and Future Work

5.1 Conclusions

In this work, we developed a variety of flexible electronic devices and utilized them for measuring and analyzing physiological signals for health monitoring. Flexible electronic devices are demonstrated to be lightweight and low-cost, and they do not cause any discomfort when attached to the human body for measurement. It is shown that these flexible devices can measure physiological signals with high accuracy in their natural context.

First, we introduced a novel design of a wearable ring with integrated flexible copper electrodes for bioelectrical impedance analysis. The designed system minimizes the electrode placement error and compensates for the parasitic impedance caused by small, dry copper electrodes. The performance of the flexible copper electrodes was compared with the commercial Ag/AgCl electrodes by conducting experiments on 40 healthy human subjects. The three-electrode method was used to determine the skin-electrode contact impedance. The contact impedance of the flexible dry copper electrodes ($5.18 \pm 0.66 \text{ k}\Omega$) was found to be much higher than that of the wet Ag/AgCl electrodes ($933.37 \pm 40.06 \text{ }\Omega$). This is mainly because of the absence of conductive gel and the smaller size of flexible dry electrodes ($26 \text{ mm} \times 10 \text{ mm}$) as compared to the wet electrodes ($40.6 \text{ mm} \times 33.02 \text{ mm}$). The four-electrode method was used to eliminate the skin-electrode contact impedance. This technique removed the electrode impedance from the body impedance, given that the input impedance of the measurement circuit is

sufficiently high. Electric current constriction was another factor that caused higher impedance in small flexible electrodes. This higher impedance due to the current-constricting geometry could not be eliminated using the four-electrode method. The average impedance in flexible electrodes was calculated to be $R_p = 25.37 \Omega$ and $X_p = -15.8 \Omega$. Furthermore, the hand and fingers imposed a great amount of impedance even though they only constituted a small part of the human body. The average wrist-to-finger impedance was calculated as $R_{hand} = 71.8 \Omega$ and $X_{hand} = -29.62 \Omega$. The microcontroller was programmed to compensate for these higher impedances caused by the hand/fingers and the current constriction of small flexible electrodes. The designed ring analyzer was then compared with the commercial analyzer OMRON HBF 306C for body fat estimation. The linear regression demonstrated a strong correlation ($r = 0.9$) between the designed ring-based analyzer and the reference monitor for body fat estimation. Furthermore, the Bland-Altman plot demonstrated that only 2 out of the 40 subjects lied outside the 95% limit of agreement.

Afterward, we developed two highly flexible multi-frequency BIA systems, one on paper and the other on a plastic substrate, and compared their electrical and mechanical performances. Conductive silver ink (Alfa Aesar 45661) was used to develop interconnects by using a fluid dispensing machine (Voltera V-one). Failure analysis was performed to determine the maximum bending angle at which the electrical bond between the electronic component and the substrates broke. The failure angle for the paper was found to be $53^\circ \pm 4^\circ$, while, for plastic, the failure angle was $42^\circ \pm 3^\circ$. The fibrous porous structure of the paper absorbed the silver, which strengthened the bond between the two materials. By comparison, the plastic substrate was a non-porous material and all the

printed silver traces were coated on the surface without providing additional adhesion. The power consumption was also measured for the BIA systems developed on both substrates. The power consumption of the system developed on the paper substrate during active mode (83.3 mW) was higher than that of the system developed on the plastic substrate (65.7 mW). In addition, the system developed on conventional rigid PCB consumed the least amount of power (53.4 mW). The difference in power consumption came from the properties of silver traces on the flexible substrates. For example, a silver trace on plastic had a resistance of $0.3 \Omega/\text{cm}$ while on paper it was increased to $0.5 \Omega/\text{cm}$. This is because the silver ink sinks into the fibers of the paper, hence decreasing the uniformity, thickness, and eventually the conductivity of the silver trace. The performance of the flexible paper and plastic-based electrodes were compared with the commercial Ag/AgCl electrodes. The experiment was conducted on 12 healthy subjects, following an approved protocol by Rowan University Institutional Review Board. The results demonstrated that the skin-electrode contact impedance of flexible dry electrodes was much smaller than that of the wet electrodes throughout the frequency spectrum. This is due to the larger size of flexible electrodes ($85 \text{ mm} \times 50 \text{ mm}$) as compared to Ag/AgCl electrodes ($40.6 \text{ mm} \times 33.02 \text{ mm}$). The large surface area provides a wider path for the electric current to go through the body, thus even though the flexible electrodes lack the presence of conductive gel, their electrode impedance is lower. Between the two flexible substrates, the contact impedance of plastic-based electrodes was lower because the silver layer on plastic possessed higher electrical conductivity than that on the paper substrate. Finally, the bioimpedance data of 12 subjects were measured using the 4-electrode method to eliminate the electrode contact impedance. The results demonstrated

that after the calibration, all the subjects showed a similar trend of bioimpedance throughout the frequency spectrum of both paper and plastic sensor modules.

Last, we investigated a novel methodology to provide compensation against mechanical deformation for flexible resistive temperature detectors (RTDs). Two RTDs were fabricated back-to-back on a PDMS substrate through stencil printing using a silver paste. When the sensor was bent on a curved surface, the RTD on the top side faced tension. This caused an increase in the electrical resistance of the RTD. Meanwhile, the RTD on the bottom side faced compression which decreased the electrical resistance. Since both RTDs were fabricated back-to-back, their resistance changed differentially, and the sum of resistance remained almost a constant. Therefore, the resistance variation caused by bending was canceled out. Similarly, when the sensor was stretched, both RTDs were stretched equally, and they experienced a comparable amount of tension which increased their resistance equally. Therefore, the subtraction of resistances of the two RTDs was almost zero under stretching. The bending experiment was conducted using 3D printed curvatures with varying radii ranging from 100 mm to 40 mm. The results demonstrated that, after calibration, the sum of change of resistance of dual RTDs ($2 \pm 0.7\%$) was very small as compared to the variation of a single RTD (30.1% and -22.5% for the two individual RTDs). The baseline temperature sensing characteristics of the RTDs were determined by heating the sensor on a flat surface. A flexible heater was used and the temperature was varied from 20°C to 40°C with increments of 5°C. The temperature coefficient of resistance (TCR) for the sum of resistance was calculated to be $5.9 \times 10^{-3}/^{\circ}\text{C}$. The sensor performance was then analyzed by considering both bending and heating. A maximum error of 32% was observed when a single RTD was tested at a

temperature of 40°C with a bending radius of 40 mm. When both RTDs were used and the bending compensation methodology was applied, the maximum error after calibration was reduced to 2.3%. The stretching experiment was conducted using a tensile testing machine. The TCR for the subtraction of resistance was calculated to be $2.5 \times 10^{-3}/^{\circ}\text{C}$. Finally, the sensor was tested for simultaneous stretching and heating, and the measurement error of a single RTD was found to be effectively reduced by using the compensation method. Table 6 shows the comparison of our designed device with other strain gauges reported in recent publications.

Table 5

Comparison of the Designed RTD with Similar Systems

Source	Substrate	Deposited Material	Fabrication Methodology	Notes	Temperature Sensitivity
[154]	PET	Reduced graphene oxide	Air spray coating	Compressed layer structure	$6.34 \times 10^{-3}/^{\circ}\text{C}$
[171]	PI	Silver ink	Ink jet printing	N/A	$2.19 \times 10^{-3}/^{\circ}\text{C}$
[173]	PI and PU	Gold and chromium (10:1)	Photolithography	Very small gauge factor	$2.7 \times 10^{-3}/^{\circ}\text{C}$

Source	Substrate	Deposited Material	Fabrication Methodology	Notes	Temperature Sensitivity
[184]	PI	Silver-carbon composite	Screen printing	N/A	$2.6 \times 10^{-3}/^{\circ}\text{C}$
[185]	PI	Platinum and indium oxide	Photolithography	Temperature based Electromotive force	$0.8 \times 10^{-4}/^{\circ}\text{C}$
[177]	PDMS	Ligand-treated silver nanocrystal	Coating and deposition	N/A	$0.5/^{\circ}\text{C}$
[174]	PET	Silver ink	Ink jet printing	Dual sensor (only for bending)	$1.076 \times 10^{-3}/^{\circ}\text{C}$
This Work	PDMS	Silver adhesive	Stencil printing	Dual sensor (bending and stretching)	$5.9 \times 10^{-3}/^{\circ}\text{C}$ $2.5 \times 10^{-3}/^{\circ}\text{C}$

An algorithm was also developed to determine the physical state of the sensor. The compensation-implemented flexible sensor demonstrated promising results and can be used to measure temperature accurately under mechanically deformed conditions. This provided the sensor the ability to adapt to curved or irregular surfaces and perform long-term temperature measurements as compared to conventional temperature sensors that are fabricated using silicon technology. The compensation method enhanced the competence of flexible temperature sensors and increases their potential for applications in wearable electronics.

5.2 Recommendations and Future Work

Several research efforts are likely still required in the future to make the designed wearable devices available on a commercial scale and utilize them in a daily home-based environment. Initially, a more compact design is needed that will allow for the potential integration of the wearable ring with an integrated circuit on a flexible substrate-based impedance analyzer for design improvement. This would allow us to further miniaturize the hardware so that the entire device can be encapsulated on the ring. Furthermore, data needs to be collected from additional subjects in order to develop a new, but fully validated equation for body fat estimation. The device-specific equation for the determination of body fat will provide higher accuracy with more subjects involved. The complete equation will include compensating factors for wrists, fingers, and the current constriction due to small dry electrodes, in addition to the height, weight, age, and gender information for the specific subject. The next iteration of this device also needs to include capabilities for body hydration content, skeletal mass, and muscle mass estimation. This

will allow the flexible wearable device to determine the complete composition of the human body and provide a bigger, more detailed picture for health analysis.

Additional functionalities and capabilities are also required in the designed flexible temperature sensor. The next iteration of the device can include real-time strain monitoring ability, which can be achieved using the Wheatstone bridge configuration, along with the temperature measurement. New fabrication methodologies such as nano inkjet printing and photolithography should be evaluated in order to develop sensors on a smaller scale. In addition, using application-specific integrated circuit (ASIC) designs will allow the integration of the controller module on the PDMS substrate along with the sensor module. A fully integrated and miniaturized temperature sensor system will allow real-time measurements with high accuracy. Furthermore, artificial intelligence and machine learning algorithms can be developed and applied to help the device determine the physical state of the RTD even when the ambient temperature is changing. Last, these algorithms can significantly improve the overall system design, eventually leading to the production of smart wearable systems for healthcare applications.

References

- [1] K. D. Harris, A. L. Elias, and H. J. Chung, "Flexible Electronics under Strain: A Review of Mechanical Characterization and Durability Enhancement Strategies," *Journal of Materials Science*, vol. 51, no. 6, pp. 2771-2805, 2016.
- [2] D. Baran, D. Corzo, and G. Blazquez, "Flexible Electronics: Status, Challenges and Opportunities," *Frontiers in Electronics*, Specialty Grand Challenge vol. 1, 2020.
- [3] J. Kang *et al.*, "Tough and Water-Insensitive Self-Healing Elastomer for Robust Electronic Skin," *Advanced Materials*, vol. 30, no. 13, p. 1706846, 2018.
- [4] J. Y. Oh *et al.*, "Intrinsically Stretchable and Healable Semiconducting Polymer for Organic Transistors," *Nature*, vol. 539, no. 7629, pp. 411-415, 2016.
- [5] C. J. Bettinger and Z. Bao, "Biomaterials-Based Organic Electronic Devices," *Polymer International*, vol. 59, no. 5, pp. 563-567, 2010.
- [6] S. Kim, C. Laschi, and B. Trimmer, "Soft Robotics: A Bioinspired Evolution in Robotics," *Trends in Biotechnology*, vol. 31, no. 5, pp. 287-294, 2013.
- [7] H. Liu, L. Wang, G. Lin, and Y. Feng, "Recent Progress in the Fabrication of Flexible Materials for Wearable Sensor," *Biomaterials Science*, 2021.
- [8] S. Moreno *et al.*, "Biocompatible Collagen Films as Substrates for Flexible Implantable Electronics," *Advanced Electronic Materials*, vol. 1, no. 9, p. 1500154, 2015.
- [9] F. R. Fan, W. Tang, and Z. L. Wang, "Flexible Nanogenerators for Energy Harvesting and Self-Powered Electronics," *Advanced Materials*, vol. 28, no. 22, pp. 4283-4305, 2016.
- [10] H. L. Park, Y. Lee, N. Kim, D. G. Seo, G. T. Go, and T. W. Lee, "Flexible Neuromorphic Electronics for Computing, Soft Robotics, and Neuroprosthetics," *Advanced Materials*, vol. 32, no. 15, p. 1903558, 2020.

- [11] B. Arman Kuzubasoglu and S. Kursun Bahadir, "Flexible Temperature Sensors: A Review," *Sensors and Actuators A: Physical*, vol. 315, p. 112282, 2020.
- [12] Y. Ma *et al.*, "Flexible Hybrid Electronics for Digital Healthcare," *Advanced Materials*, vol. 32, no. 15, p. 1902062, 2020.
- [13] C. Dagdeviren *et al.*, "Conformal Piezoelectric Energy Harvesting and Storage from Motions of the Heart, Lung, and Diaphragm," *Proceedings of the National Academy of Sciences*, vol. 111, no. 5, pp. 1927-1932, 2014.
- [14] S. Xu *et al.*, "Soft Microfluidic Assemblies of Sensors, Circuits, and Radios for the Skin," *Science*, vol. 344, no. 6179, pp. 70-74, 2014.
- [15] L. Wang *et al.*, "Application Challenges in Fiber and Textile Electronics," *Advanced Materials*, vol. 32, no. 5, p. 1901971, 2020.
- [16] K. Harris, A. Elias, and H.-J. Chung, "Flexible Electronics under Strain: A Review of Mechanical Characterization and Durability Enhancement Strategies," *Journal of Materials Science*, vol. 51, no. 6, pp. 2771-2805, 2016.
- [17] V. Zardetto, T. M. Brown, A. Reale, and A. Di Carlo, "Substrates for Flexible Electronics: A Practical Investigation on the Electrical, Film Flexibility, Optical, Temperature, and Solvent Resistance Properties," *Journal of Polymer Science Part B: Polymer Physics*, vol. 49, no. 9, pp. 638-648, 2011.
- [18] G. Fortunato, A. Pecora, and L. Maiolo, "Polysilicon Thin-Film Transistors on Polymer Substrates," *Materials Science in Semiconductor Processing*, vol. 15, no. 6, pp. 627-641, 2012.
- [19] A. Nathan *et al.*, "Flexible Electronics: The Next Ubiquitous Platform," *Proceedings of the IEEE*, vol. 100, no. Special Centennial Issue, pp. 1486-1517, 2012.
- [20] W. MacDonald, M. Looney, D. MacKerron, R. Eveson, and K. Rakos, "Designing and Manufacturing Substrates for Flexible Electronics," *Journal of Plastic, Rubber, and Composites*, vol. 37, no. 2-4, pp. 41-45, 2008.

- [21] L. Wang, R. Zhu, and G. Li, "Temperature and Strain Compensation for Flexible Sensors Based on Thermosensation," *ACS Applied Materials & Interfaces*, vol. 12, no. 1, pp. 1953-1961, 2019.
- [22] J. A. Spechler, T. W. Koh, J. T. Herb, B. P. Rand, and C. B. Arnold, "A Transparent, Smooth, Thermally Robust, Conductive Polyimide for Flexible Electronics," *Advanced Functional Materials*, vol. 25, no. 48, pp. 7428-7434, 2015.
- [23] A. Serkov, H. Snelling, S. Heusing, and T. M. Amaral, "Laser Sintering of Gravure Printed Indium Tin Oxide Films on Polyethylene Terephthalate for Flexible Electronics," *Scientific Reports*, vol. 9, no. 1, pp. 1-8, 2019.
- [24] Y. Xu, Y. Yang, D.-X. Yan, H. Duan, G. Zhao, and Y. Liu, "Flexible and Conductive Polyurethane Composites for Electromagnetic Shielding and Printable Circuit," *Chemical Engineering Journal*, vol. 360, pp. 1427-1436, 2019.
- [25] S. H. Jeong, S. Zhang, K. Hjort, J. Hilborn, and Z. Wu, "Pdms-Based Elastomer Tuned Soft, Stretchable, and Sticky for Epidermal Electronics," *Advanced Materials*, vol. 28, no. 28, pp. 5830-5836, 2016.
- [26] Z. Wang, A. A. Volinsky, and N. D. Gallant, "Crosslinking Effect on Polydimethylsiloxane Elastic Modulus Measured by Custom-Built Compression Instrument," *Journal of Applied Polymer Science*, vol. 131, no. 22, 2014.
- [27] M. N. Troccoli, A. J. Roudbari, T.-K. Chuang, and M. K. Hatalis, "Polysilicon Tft Circuits on Flexible Stainless Steel Foils," *Solid-State Electronics*, vol. 50, no. 6, pp. 1080-1087, 2006.
- [28] Z. Xie, L.-S. Hung, and F. Zhu, "A Flexible Top-Emitting Organic Light-Emitting Diode on Steel Foil," *Chemical Physics Letters*, vol. 381, no. 5-6, pp. 691-696, 2003.
- [29] K. Onoda, S. Ngamsinlapasathian, T. Fujieda, and S. Yoshikawa, "The Superiority of Ti Plate as the Substrate of Dye-Sensitized Solar Cells," *Solar Energy Materials and Solar Cells*, vol. 91, no. 13, pp. 1176-1181, 2007.

- [30] B. W. D'Andrade, A. Z. Kattamis, and P. F. Murphy, "13 - Flexible Organic Electronic Devices on Metal Foil Substrates for Lighting, Photovoltaic, And other Applications," in *Handbook of Flexible Organic Electronics*, S. Logothetidis, Ed. Oxford: Woodhead Publishing, 2015, pp. 315-341.
- [31] T. Ding *et al.*, "Scalable Thermoelectric Fibers for Multifunctional Textile-Electronics," *Nature Communications*, vol. 11, no. 1, pp. 1-8, 2020.
- [32] L. Nyholm, G. Nyström, A. Mihranyan, and M. Strømme, "Toward Flexible Polymer and Paper-Based Energy Storage Devices," *Advanced Materials*, vol. 23, no. 33, pp. 3751-3769, 2011.
- [33] D. Tobjörk and R. Österbacka, "Paper Electronics," *Advanced Materials*, vol. 23, no. 17, pp. 1935-1961, 2011.
- [34] W. Zeng, L. Shu, Q. Li, S. Chen, F. Wang, and X. M. Tao, "Fiber-Based Wearable Electronics: A Review of Materials, Fabrication, Devices, and Applications," *Advanced Materials*, vol. 26, no. 31, pp. 5310-5336, 2014.
- [35] C. A. Norstebo, "Intelligent Textiles, Soft Products," *Journal of Future Materials*, pp. 1-14, 2003.
- [36] D. S. Hecht, L. Hu, and G. Irvin, "Emerging Transparent Electrodes Based on Thin Films of Carbon Nanotubes, Graphene, and Metallic Nanostructures," *Advanced Materials*, vol. 23, no. 13, pp. 1482-1513, 2011.
- [37] S. Naghdi, K. Y. Rhee, D. Hui, and S. J. Park, "A Review of Conductive Metal Nanomaterials as Conductive, Transparent, and Flexible Coatings, Thin Films, and Conductive Fillers: Different Deposition Methods and Applications," *Coatings*, vol. 8, no. 8, p. 278, 2018.
- [38] Q. Huang and Y. Zhu, "Printing Conductive Nanomaterials for Flexible and Stretchable Electronics: A Review of Materials, Processes, and Applications," *Advanced Materials Technologies*, vol. 4, no. 5, p. 1800546, 2019.
- [39] D. Li, D. Sutton, A. Burgess, D. Graham, and P. D. Calvert, "Conductive Copper and Nickel Lines Via Reactive Inkjet Printing," *Journal of Materials Chemistry*, vol. 19, no. 22, pp. 3719-3724, 2009.

- [40] S. Jang *et al.*, "Sintering of Inkjet Printed Copper Nanoparticles for Flexible Electronics," *Scripta Materialia*, vol. 62, no. 5, pp. 258-261, 2010.
- [41] D. Huang, F. Liao, S. Molesa, D. Redinger, and V. Subramanian, "Plastic-Compatible Low Resistance Printable Gold Nanoparticle Conductors for Flexible Electronics," *Journal of the Electrochemical Society*, vol. 150, no. 7, p. G412, 2003.
- [42] Y. Li, O. Dahhan, C. D. Filipe, J. D. Brennan, and R. H. Pelton, "Deposited Nanoparticles Can Promote Air Clogging of Piezoelectric Inkjet Printhead Nozzles," *Langmuir*, vol. 35, no. 16, pp. 5517-5524, 2019.
- [43] I. V. Zaporotskova, N. P. Boroznina, Y. N. Parkhomenko, and L. V. Kozhitov, "Carbon Nanotubes: Sensor Properties. A Review," *Modern Electronic Materials*, vol. 2, no. 4, pp. 95-105, 2016.
- [44] L. F. Pereira and M. S. Ferreira, "Electronic Transport on Carbon Nanotube Networks: A Multiscale Computational Approach," *Nano Communication Networks*, vol. 2, no. 1, pp. 25-38, 2011.
- [45] R. P. Tortorich, E. Song, and J.-W. Choi, "Inkjet-Printed Carbon Nanotube Electrodes with Low Sheet Resistance for Electrochemical Sensor Applications," *Journal of the Electrochemical Society*, vol. 161, no. 2, p. B3044, 2013.
- [46] T. M. Seeberg, A. Røyset, S. Jähren, and F. Strisland, "Printed Organic Conductive Polymers Thermocouples in Textile and Smart Clothing Applications," presented at the 2011 Annual International Conference of the IEEE Engineering in Medicine and Biology Society, 30 Aug.-3 Sept. 2011, 2011.
- [47] G. Cummins and M. P. Desmulliez, "Inkjet Printing of Conductive Materials: A Review," *Circuit World*, vol. 38, no. 4, pp. 193-213, 2012.
- [48] W. Gao *et al.*, "Fully Integrated Wearable Sensor Arrays for Multiplexed in Situ Perspiration Analysis," *Nature*, vol. 529, no. 7587, pp. 509-514, 2016.
- [49] D. E. Schwartz *et al.*, "Flexible Hybrid Electronic Circuits and Systems," *IEEE Journal on Emerging Selected topics in Circuits Systems*, vol. 7, no. 1, pp. 27-37, 2016.

- [50] R. L. Chaney, D. G. Wilson, D. R. Hackler, K. J. DeGregorio, and D. E. Leber, "New Silicon Frontiers: Physically Flexible System-on-a-Chip," presented at the 2017 IEEE Workshop on Microelectronics and Electron Devices (WMED), 2017.
- [51] C. Ye, B. G. Stewart, and S. K. Sitaraman, "Stretchability of Serpentine Interconnect on Polymer Substrate for Flexible Electronics: A Geometry and Material Sensitivity Analysis," presented at the 2020 IEEE 70th Electronic Components and Technology Conference (ECTC), 2020.
- [52] D.-H. Kim *et al.*, "Materials and Noncoplanar Mesh Designs for Integrated Circuits with Linear Elastic Responses to Extreme Mechanical Deformations," *Proceedings of the National Academy of Sciences*, vol. 105, no. 48, pp. 18675-18680, 2008.
- [53] P. Descent, R. Izquierdo, and C. Fayomi, "Printing of Temperature and Humidity Sensors on Flexible Substrates for Biomedical Applications," presented at the 2018 IEEE International Symposium on Circuits and Systems (ISCAS), 2018.
- [54] L. Nayak, S. Mohanty, S. K. Nayak, and A. Ramadoss, "A Review on Inkjet Printing of Nanoparticle Inks for Flexible Electronics," *Journal of Materials Chemistry C*, vol. 7, no. 29, pp. 8771-8795, 2019.
- [55] E. B. Secor, S. Lim, H. Zhang, C. D. Frisbie, L. F. Francis, and M. C. Hersam, "Gravure Printing of Graphene for Large-Area Flexible Electronics," *Advanced Materials*, vol. 26, no. 26, pp. 4533-4538, 2014.
- [56] W. J. Hyun, E. B. Secor, M. C. Hersam, C. D. Frisbie, and L. F. Francis, "High-Resolution Patterning of Graphene by Screen Printing with a Silicon Stencil for Highly Flexible Printed Electronics," *Advanced Materials*, vol. 27, no. 1, pp. 109-115, 2015.
- [57] X. Cao *et al.*, "Screen Printing as a Scalable and Low-Cost Approach for Rigid and Flexible Thin-Film Transistors Using Separated Carbon Nanotubes," *ACS Nano*, vol. 8, no. 12, pp. 12769-12776, 2014.
- [58] S. Khan, L. Lorenzelli, and R. S. Dahiya, "Technologies for Printing Sensors and Electronics over Large Flexible Substrates: A Review," *IEEE Sensors Journal*, vol. 15, no. 6, pp. 3164-3185, 2014.

- [59] P. F. Moonen, I. Yakimets, and J. Huskens, "Fabrication of Transistors on Flexible Substrates: From Mass-Printing to High-Resolution Alternative Lithography Strategies," *Advanced Materials*, vol. 24, no. 41, pp. 5526-5541, 2012.
- [60] K. J. Baeg, M. Caironi, and Y. Y. Noh, "Toward Printed Integrated Circuits Based on Unipolar or Ambipolar Polymer Semiconductors," *Advanced Materials*, vol. 25, no. 31, pp. 4210-4244, 2013.
- [61] R. Kay and M. Desmulliez, "A Review of Stencil Printing for Microelectronic Packaging," *Soldering Surface Mount Technology*, 2012.
- [62] S. Kongkaew *et al.*, "A Fabrication of Multichannel Graphite Electrode Using Low-Cost Stencil-Printing Technique," *Sensors*, vol. 22, no. 8, p. 3034, 2022.
- [63] W. Wu, "Stretchable Electronics: Functional Materials, Fabrication Strategies and Applications," *Science and Technology of Advanced Materials*, vol. 20, no. 1, pp. 187-224, 2019.
- [64] D. Wu *et al.*, "A Percolation Network Model to Predict the Electrical Property of Flexible Cnt/Pdms Composite Films Fabricated by Spin Coating Technique," *Composites Part B: Engineering*, vol. 174, p. 107034, 2019.
- [65] M. G. Say *et al.*, "Spray-Coated Paper Supercapacitors," *npj Flexible Electronics*, vol. 4, no. 1, pp. 1-7, 2020.
- [66] C. Zuo, A. D. Scully, and M. Gao, "Drop-Casting Method to Screen Ruddlesden-Popper Perovskite Formulations for Use in Solar Cells," *ACS Applied Materials Interfaces*, vol. 13, no. 47, pp. 56217-56225, 2021.
- [67] R. Ahmad, O. S. Wolfbeis, Y.-B. Hahn, H. N. Alshareef, L. Torsi, and K. N. Salama, "Deposition of Nanomaterials: A Crucial Step in Biosensor Fabrication," *Langmuir*, vol. 17, pp. 289-321, 2018.
- [68] J.-O. Carlsson and P. M. Martin, "Chapter 7 - Chemical Vapor Deposition," in *Handbook of Deposition Technologies for Films and Coatings (Third Edition)*, P. M. Martin, Ed. Boston: William Andrew Publishing, 2010, pp. 314-363.

- [69] A. V. Rane, K. Kanny, V. K. Abitha, and S. Thomas, "Chapter 5 - Methods for Synthesis of Nanoparticles and Fabrication of Nanocomposites," in *Synthesis of Inorganic Nanomaterials*, S. Mohan Bhagyaraj, O. S. Oluwafemi, N. Kalarikkal, and S. Thomas, Eds.: Woodhead Publishing, 2018, pp. 121-139.
- [70] M. D. Husain, R. Kennon, and T. Dias, "Design and Fabrication of Temperature Sensing Fabric," *Journal of Industrial Textiles*, vol. 44, no. 3, pp. 398-417, 2014.
- [71] T.-C. Codau, E. Onofrei, G. Bedek, D. Dupont, and C. Cochrane, "Embedded Textile Heat Flow Sensor Characterization and Application," *Sensors Actuators A: Physical*, vol. 235, pp. 131-139, 2015.
- [72] P. Lugoda, T. Dias, T. Hughes-Riley, and R. Morris, "Refinement of Temperature Sensing Yarns," *Multidisciplinary Digital Publishing Institute Proceedings*, vol. 2, no. 3, p. 123, 2017.
- [73] T. Hughes-Riley, P. Lugoda, T. Dias, C. L. Trabi, and R. H. Morris, "A Study of Thermistor Performance within a Textile Structure," *Sensors*, vol. 17, no. 8, p. 1804, 2017.
- [74] C. Pang *et al.*, "Highly Skin-Conformal Microhairy Sensor for Pulse Signal Amplification," *Advanced Materials*, vol. 27, no. 4, pp. 634-640, 2015.
- [75] N. Luo *et al.*, "Flexible Piezoresistive Sensor Patch Enabling Ultralow Power Cuffless Blood Pressure Measurement," *Advanced Functional Materials*, vol. 26, no. 8, pp. 1178-1187, 2016.
- [76] T. Borisova *et al.*, "An Amperometric Glutamate Biosensor for Monitoring Glutamate Release from Brain Nerve Terminals and in Blood Plasma," *Analytica Chimica Acta*, vol. 1022, pp. 113-123, 2018.
- [77] L. Maiolo, D. Polese, and A. Convertino, "The Rise of Flexible Electronics in Neuroscience, from Materials Selection to in Vitro and in Vivo Applications," *Advances in Physics: X*, vol. 4, no. 1, p. 1664319, 2019.
- [78] Y. Chen, Y. Zhang, Z. Liang, Y. Cao, Z. Han, and X. Feng, "Flexible Inorganic Bioelectronics," *npj Flexible Electronics*, vol. 4, no. 1, pp. 1-20, 2020.

- [79] B. G. Lapatki, J. P. Van Dijk, I. E. Jonas, M. J. Zwarts, and D. F. Stegeman, "A Thin, Flexible Multielectrode Grid for High-Density Surface Emg," *Journal of Applied Physiology*, vol. 96, no. 1, pp. 327-336, 2004.
- [80] B. Nie, S. Liu, Q. Qu, Y. Zhang, M. Zhao, and J. Liu, "Bio-Inspired Flexible Electronics for Smart E-Skin," *Acta Biomaterialia*, 2021.
- [81] J. Engel, J. Chen, Z. Fan, and C. Liu, "Polymer Micromachined Multimodal Tactile Sensors," *Sensors Actuators A: Physical*, vol. 117, no. 1, pp. 50-61, 2005.
- [82] L. Chen, X. Chang, H. Wang, J. Chen, and Y. Zhu, "Stretchable and Transparent Multimodal Electronic-Skin Sensors in Detecting Strain, Temperature, and Humidity," *Nano Energy*, vol. 96, p. 107077, 2022.
- [83] T. Yamaguchi, T. Kashiwagi, T. Arie, S. Akita, and K. Takei, "Human-Like Electronic Skin-Integrated Soft Robotic Hand," *Advanced Intelligent Systems*, vol. 1, no. 2, p. 1900018, 2019.
- [84] B. Oh *et al.*, "Untethered Soft Robotics with Fully Integrated Wireless Sensing and Actuating Systems for Somatosensory and Respiratory Functions," *Soft Robotics*, vol. 7, no. 5, pp. 564-573, 2020.
- [85] Z. Shi *et al.*, "Wearable Battery-Free Theranostic Dental Patch for Wireless Intraoral Sensing and Drug Delivery," *npj Flexible Electronics*, vol. 6, no. 1, pp. 1-11, 2022.
- [86] H. Joo *et al.*, "Soft Implantable Drug Delivery Device Integrated Wirelessly with Wearable Devices to Treat Fatal Seizures," *Science advances*, vol. 7, no. 1, p. eabd4639, 2021.
- [87] J. Lee *et al.*, "Flexible, Sticky, and Biodegradable Wireless Device for Drug Delivery to Brain Tumors," *Nature Communications*, vol. 10, no. 1, pp. 1-9, 2019.
- [88] T. K. Bera, "Bioelectrical Impedance Methods for Noninvasive Health Monitoring: A Review," *Journal of medical engineering*, vol. 2014, 2014.
- [89] J. J. Ackmann, "Complex Bioelectric Impedance Measurement System for the Frequency Range from 5 Hz to 1 Mhz," *Annals of Biomedical Engineering*, vol. 21, no. 2, pp. 135-146, 1993.

- [90] J. J. Ackmann and M. A. Seitz, "Methods of Complex Impedance Measurements in Biologic Tissue," *Critical Reviews in Biomedical Engineering*, vol. 11, no. 4, pp. 281-311, 1984.
- [91] K. Cha, G. M. Chertow, J. Gonzalez, J. M. Lazarus, and D. W. Wilmore, "Multifrequency Bioelectrical Impedance Estimates the Distribution of Body Water," *Journal of Applied Physiology*, vol. 79, no. 4, pp. 1316-1319, 1995.
- [92] J. Nyboer, M. M. Kreider, and L. Hannapel, "Electrical Impedance Plethysmography: A Physical and Physiologic Approach to Peripheral Vascular Study," *Circulation*, vol. 2, no. 6, pp. 811-821, 1950.
- [93] T. K. Bera, "Bioelectrical Impedance and the Frequency Dependent Current Conduction through Biological Tissues: A Short Review," presented at the IOP Conference Series: Materials Science and Engineering, 2018.
- [94] U. G. Kyle *et al.*, "Bioelectrical Impedance Analysis—Part I: Review of Principles and Methods," vol. 23, no. 5, pp. 1226-1243, 2004.
- [95] C. H. Ling *et al.*, "Accuracy of Direct Segmental Multi-Frequency Bioimpedance Analysis in the Assessment of Total Body and Segmental Body Composition in Middle-Aged Adult Population," vol. 30, no. 5, pp. 610-615, 2011.
- [96] X. Xie, N. Kolthoff, O. Bärenholt, and S. Nielsen, "Validation of a Leg-to-Leg Bioimpedance Analysis System in Assessing Body Composition in Postmenopausal Women," *International Journal of Obesity*, vol. 23, no. 10, pp. 1079-1084, 1999.
- [97] T. K. Bera and J. Nagaraju, "Electrical Impedance Spectroscopic Studies on Broiler Chicken Tissue Suitable for the Development of Practical Phantoms in Multifrequency Eit," *Journal of Electrical Bioimpedance*, vol. 2, no. 1, pp. 48-63, 2011.
- [98] A. D. Bauchot, F. R. Harker, and W. M. Arnold, "The Use of Electrical Impedance Spectroscopy to Assess the Physiological Condition of Kiwifruit," *Postharvest Biology*, vol. 18, no. 1, pp. 9-18, 2000.

- [99] P. Kassanos, "Bioimpedance Sensors: A Tutorial," *IEEE Sensors Journal*, 2021.
- [100] K. R. Foster and H. C. Lukaski, "Whole-Body Impedance--What Does It Measure?," *The American Journal of Clinical Nutrition*, vol. 64, no. 3, pp. 388S-396S, 1996.
- [101] E. Barsoukov and J. R. Macdonald, *Impedance Spectroscopy Theory, Experiment, And*. John Wiley & Sons, 2018.
- [102] S. F. Yalin *et al.*, "Single-Frequency and Multi-Frequency Bioimpedance Analysis: What Is the Difference?," *Nephrology*, vol. 23, no. 5, pp. 438-445, 2018.
- [103] B. Cornish, B. Thomas, and L. Ward, "Improved Prediction of Extracellular and Total Body Water Using Impedance Loci Generated by Multiple Frequency Bioelectrical Impedance Analysis," *Physics in Medicine*, vol. 38, no. 3, p. 337, 1993.
- [104] U. G. Kyle, L. Genton, D. O. Slosman, and C. Pichard, "Fat-Free and Fat Mass Percentiles in 5225 Healthy Subjects Aged 15 to 98 Years," *Nutrition*, vol. 17, no. 7, pp. 534-541, 2001.
- [105] S.-B. Kim, N.-R. Lee, T.-M. Shin, and Y.-H. Lee, "Development and Evaluation of a Multi-Frequency Bioelectrical Impedance Analysis Analyzer for Estimating Acupoint Composition," *Journal of Acupuncture Meridian Studies*, vol. 7, no. 1, pp. 33-43, 2014.
- [106] K. Ain, R. A. Wibowo, S. Soelistiono, L. Muniroh, and B. Ariwanto, "Design and Development of a Low-Cost Arduino-Based Electrical Bioimpedance Spectrometer," *Journal of Medical Signals*, vol. 10, no. 2, p. 125, 2020.
- [107] W. Hannan, S. Cowen, C. Plester, and K. Fearon, "Comparison of Bio-Impedance Spectroscopy and Multi-Frequency Bio-Impedance Analysis for the Assessment of Extracellular and Total Body Water in Surgical Patients," *Clinical Science*, vol. 89, no. 6, pp. 651-658, 1995.
- [108] U. G. Kyle, L. Genton, L. Karsegard, D. O. Slosman, and C. Pichard, "Single Prediction Equation for Bioelectrical Impedance Analysis in Adults Aged 20-94 Years," *Nutrition*, vol. 17, no. 3, pp. 248-253, 2001.

- [109] R. Buendia, "Improvements in Bioimpedance Spectroscopy data Analysis: Artefact Correction, Cole parameters, and Body Fluid Estimation," KTH Royal Institute of Technology, 2013.
- [110] M. I. Pribyl, J. D. Smith, and G. R. Grimes, "Accuracy of the Omron Hbf-500 Body Composition Monitor in Male and Female College Students," *International journal of exercise science*, vol. 4, no. 2, p. 2, 2011.
- [111] J. Ferreira, I. Pau, K. Lindecrantz, and F. Seoane, "A Handheld and Textile-Enabled Bioimpedance System for Ubiquitous Body Composition Analysis. An Initial Functional Validation," *IEEE Journal of Biomedical Health Informatics*, vol. 21, no. 5, pp. 1224-1232, 2016.
- [112] A. Choi *et al.*, "Smartphone-Based Bioelectrical Impedance Analysis Devices for Daily Obesity Management," *Sensors*, vol. 15, no. 9, pp. 22151-22166, 2015.
- [113] S. Hersek *et al.*, "Wearable Vector Electrical Bioimpedance System to Assess Knee Joint Health," *IEEE Transactions on Biomedical Engineering*, vol. 64, no. 10, pp. 2353-2360, 2016.
- [114] M. Konijnenburg *et al.*, "A Multi (Bio) Sensor Acquisition System with Integrated Processor, Power Management, $\times 8$ Led Drivers, and Simultaneously Synchronized Ecg, Bio-Z, Gsr, and Two Ppg Readouts," *IEEE Journal of Solid-State Circuits*, vol. 51, no. 11, pp. 2584-2595, 2016.
- [115] J. Ramos, J. L. Ausín, G. Torelli, and J. F. Duque-Carrillo, "A Wireless Bioimpedance Device for Abdominal Fatness Monitoring," *Procedia Chemistry*, vol. 1, no. 1, pp. 1259-1262, 2009.
- [116] P. Divall, J. Camosso-Stefinovic, and R. Baker, "The Use of Personal Digital Assistants in Clinical Decision Making by Health Care Professionals: A Systematic Review," *Health Informatics Journal*, vol. 19, no. 1, pp. 16-28, 2013.
- [117] A. Bosity-Westphal, B. Schautz, W. Later, J. Kehayias, D. Gallagher, and M. Müller, "What Makes a Bia Equation Unique? Validity of Eight-Electrode Multifrequency Bia to Estimate Body Composition in a Healthy Adult Population," *European Journal of Clinical Nutrition*, vol. 67, no. 1, pp. S14-S21, 2013.

- [118] Seca. (2011). *Seca Mbca 514 Medical Body Composition Analyzer Product Information. Technical Product Data and Support*. Available: https://www.seca.com/fileadmin/documents/product_sheet/seca_pst_514_en_us.pdf
- [119] S. H. Ridner, C. M. Bonner, J. K. Doersam, B. A. Rhoten, B. Schultze, and M. S. Dietrich, "Bioelectrical Impedance Self-Measurement Protocol Development and Daily Variation between Healthy Volunteers and Breast Cancer Survivors with Lymphedema," *Lymphatic Research Biology*, vol. 12, no. 1, pp. 2-9, 2014.
- [120] S. L. Jones *et al.*, "Bioelectrical Impedance Vector Analysis in Critically Ill Patients: A Prospective, Clinician-Blinded Investigation," *Critical Care*, vol. 19, no. 1, pp. 1-11, 2015.
- [121] M. Usman, A. K. Gupta, and W. Xue, "Wearable Ring Bioelectrical Impedance Analyzer for Estimation and Monitoring of Body Fat," *Smart Health*, vol. 24, p. 100275, 2022.
- [122] M. Usman, A. K. Gupta, and W. Xue, "Analyzing Dry Electrodes for Wearable Bioelectrical Impedance Analyzers," presented at the 2019 IEEE Signal Processing in Medicine and Biology Symposium (SPMB), 2019.
- [123] M. Usman, S. Thapa, A. K. Gupta, and W. Xue, "Ring Based Wearable Bioelectrical Impedance Analyzer for Body Fat Estimation," presented at the 2018 IEEE International Symposium on Signal Processing and Information Technology (ISSPIT), 2018.
- [124] P. Deurenberg, R. Leenen, J. Weststrate, and J. Seidell, "Sex and Age Specific Prediction Formulas for Estimating Body Composition from Bioelectrical Impedance: A Cross-Validation Study," *International journal of obesity*, vol. 15, no. 1, pp. 17-25, 1991.
- [125] B. Heitmann, "Prediction of Body Water and Fat in Adult Danes from Measurement of Electrical Impedance. A Validation Study," *International Journal of Obesity*, vol. 14, no. 9, pp. 789-802, 1990.
- [126] T. G. Lohman, "Advances in Body Composition Assessment," *Human Kinetics*, pp. 1-23, 1992.

- [127] R. Buendia *et al.*, "Bioimpedance Technology for Detection of Thoracic Injury," *Physiological Measurement*, vol. 38, no. 11, p. 2000, 2017.
- [128] R. Buendia *et al.*, "Robustness Study of the Different Immittance Spectra and Frequency Ranges in Bioimpedance Spectroscopy Analysis for Assessment of Total Body Composition," *Physiological Measurement*, vol. 35, no. 7, p. 1373, 2014.
- [129] A. Adler and D. Holder, *Electrical Impedance Tomography: Methods, History and Applications*. CRC Press, 2021.
- [130] S. B. Heymsfield, Z. Wang, R. N. Baumgartner, and R. Ross, "Human Body Composition: Advances in Models and Methods," *Annual Review of Nutrition*, vol. 17, no. 1, pp. 527-558, 1997.
- [131] H. Hong, M. Rahal, A. Demosthenous, and R. H. Bayford, "Comparison of a New Integrated Current Source with the Modified Howland Circuit for Eit Applications," *Physiological Measurement*, vol. 30, no. 10, p. 999, 2009.
- [132] P. Bogóñez-Franco *et al.*, "Effect of Electrode Contact Impedance Mismatch on 4-Electrode Measurements of Small Body Segments Using Commercial Bia Devices," presented at the 20th IMEKO TC4 International Symposium and 18th International Workshop on ADC Modelling and Testing Research on Electric and Electronic Measurement for the Economic Upturn, Benevento, Italy, 2014.
- [133] R. F. Kushner, "Bioelectrical Impedance Analysis: A Review of Principles and Applications," *Journal of the American college of nutrition*, vol. 11, no. 2, pp. 199-209, 1992.
- [134] E. C. Hoffer, C. K. Meador, and D. C. Simpson, "Correlation of Whole-Body Impedance with Total Body Water Volume," *Journal of Applied Physiology*, vol. 27, no. 4, pp. 531-534, 1969.
- [135] M. S. Spach, R. C. Barr, J. W. Havstad, and E. C. Long, "Skin-Electrode Impedance and Its Effect on Recording Cardiac Potentials," *Circulation*, vol. 34, no. 4, pp. 649-656, 1966.
- [136] S. Grimnes and O. G. Martinsen, *Bioimpedance and Bioelectricity Basics*. Academic press, 2011.

- [137] M. H. Jung *et al.*, "Wrist-Wearable Bioelectrical Impedance Analyzer with Contact Resistance Compensation Function," presented at the 2016 IEEE SENSORS, 2016.
- [138] P. Deurenberg, K. Van der Kooy, R. Leenen, J. Weststrate, and J. Seidell, "Sex and Age Specific Prediction Formulas for Estimating Body Composition from Bioelectrical Impedance: A Cross-Validation Study," *International Journal of Obesity*, vol. 15, no. 1, pp. 17-25, 1991.
- [139] J. Ramos, J. Ausín, A. Lorido, F. Redondo, and J. Duque-Carrillo, "A Wireless, Compact, and Scalable Bioimpedance Measurement System for Energy-Efficient Multichannel Body Sensor Solutions," presented at the Journal of Physics: Conference Series, 2013.
- [140] A. Nag, S. C. Mukhopadhyay, and J. Kosel, "Wearable Flexible Sensors: A Review," vol. 17, no. 13, pp. 3949-3960, 2017.
- [141] M. Torculas, J. Medina, W. Xue, and X. Hu, "Protein-Based Bioelectronics," *ACS Biomaterials Science*, vol. 2, no. 8, pp. 1211-1223, 2016.
- [142] P. Lall, H. Jang, B. Leever, and S. Miller, "Method for Assessment of Folding-Reliability of Flexible Electronics in Wearable Applications," presented at the 2019 18th IEEE Intersociety Conference on Thermal and Thermomechanical Phenomena in Electronic Systems (ITherm), 2019.
- [143] W.-Y. Chang, T.-H. Fang, and Y.-C. Lin, "Characterization and Fabrication of Wireless Flexible Physiological Monitor Sensor," *Sensors Actuators A: Physical*, vol. 143, no. 2, pp. 196-203, 2008.
- [144] K.-J. Baeg and J. Lee, "Flexible Electronic Systems on Plastic Substrates and Textiles for Smart Wearable Technologies," *Advanced Materials Technologies*, vol. 5, no. 7, p. 2000071, 2020.
- [145] Y. Xu *et al.*, "Paper-Based Wearable Electronics," *iScience*, vol. 24, no. 7, p. 102736, 2021/07/23/ 2021.
- [146] M. Usman, M. Leone, A. K. Gupta, and W. Xue, "Fabrication and Analysis of Wearable Bioimpedance Analyzers on Paper and Plastic Substrates," *IEEE Sensors Letters*, vol. 4, no. 3, pp. 1-4, 2020.

- [147] Y. Yang, J. Wang, G. Yu, F. Niu, and P. He, "Design and Preliminary Evaluation of a Portable Device for the Measurement of Bioimpedance Spectroscopy," *Physiological Measurement*, vol. 27, no. 12, p. 1293, 2006.
- [148] C. Tan *et al.*, "A High Performance Wearable Strain Sensor with Advanced Thermal Management for Motion Monitoring," *Nature Communications*, vol. 11, no. 1, p. 3530, 2020.
- [149] J. Ferreira, F. Seoane, A. Ansele, and R. Bragos, "Ad5933-Based Spectrometer for Electrical Bioimpedance Applications," vol. 224, p. 012011: IOP Publishing.
- [150] L. C. Vieira, "Book Review: Bioimpedance and Bioelectricity Basics, by Sverre Grimnes and Orjan G. Martinsen," vol. 30, no. 2, p. 282, 2002.
- [151] Y. Khan, A. E. Ostfeld, C. M. Lochner, A. Pierre, and A. C. Arias, "Monitoring of Vital Signs with Flexible and Wearable Medical Devices," (in eng), *Adv Mater*, vol. 28, no. 22, pp. 4373-95, Jun 2016.
- [152] A. P. D. M. Abdulrazaq, N. Istiqomah, S. Al-Zubaidi, S. Karim, S. Mustapha, and E. Yusuf, "Toward a Novel Design for Coronavirus Detection and Diagnosis System Using Iot Based Drone Technology," *International Journal of Psychosocial Rehabilitation*, vol. 24, pp. 2287-2295, 03/29 2020.
- [153] A. Ahmed *et al.*, "Decreasing Body Temperature Predicts Early Rehospitalization in Congestive Heart Failure," *Journal of cardiac failure*, vol. 14, no. 6, pp. 489-496, 2008.
- [154] G. Liu *et al.*, "A Flexible Temperature Sensor Based on Reduced Graphene Oxide for Robot Skin Used in Internet of Things," *Sensors*, vol. 18, no. 5, 2018.
- [155] L. C. Tsao *et al.*, "Flexible Temperature Sensor Array Using Electro-Resistive Polymer Forhumanoid Artificial Skin," presented at the TRANSDUCERS 2007 - 2007 International Solid-State Sensors, Actuators and Microsystems Conference, 10-14 June 2007, 2007.
- [156] K. Kanao *et al.*, "Highly Selective Flexible Tactile Strain and Temperature Sensors against Substrate Bending for an Artificial Skin," *RSC Adv.*, vol. 5, 2015.

- [157] C. Wang, K. Xia, M. Zhang, M. Jian, and Y. Zhang, "An All Silk-Derived Dual-Mode E-Skin for Simultaneous Temperature-Pressure Detection," *ACS Applied Materials & Interfaces*, vol. 9, 10/24 2017.
- [158] Y. Su *et al.*, "Printable, Highly Sensitive Flexible Temperature Sensors for Human Body Temperature Monitoring: A Review," *Nanoscale Research Letters*, vol. 15, no. 1, p. 200, 2020.
- [159] N. Ibrahim, J. O. Akindoyo, and M. Mariatti, "Recent Development in Silver-Based Ink for Flexible Electronics," *Journal of Science: Advanced Materials and Devices*, vol. 7, no. 1, p. 100395, 2022.
- [160] S. Yoon, J. K. Sim, and Y.-H. Cho, "A Flexible and Wearable Human Stress Monitoring Patch," *Scientific Reports*, vol. 6, no. 1, p. 23468, 2016.
- [161] C.-Y. Lee, S.-J. Lee, M.-S. Tang, and P.-C. Chen, "In Situ Monitoring of Temperature inside Lithium-Ion Batteries by Flexible Micro Temperature Sensors," *Sensors*, vol. 11, no. 10, pp. 9942-9950, 2011.
- [162] T. Yang, X. Zhao, Y. He, and H. Zhu, "6 - Graphene-Based Sensors," in *Graphene*, H. Zhu, Z. Xu, D. Xie, and Y. Fang, Eds.: Academic Press, 2018, pp. 157-174.
- [163] P. Sehrawat, Abid, S. S. Islam, and P. Mishra, "Reduced Graphene Oxide Based Temperature Sensor: Extraordinary Performance Governed by Lattice Dynamics Assisted Carrier Transport," *Sensors and Actuators B: Chemical*, vol. 258, pp. 424-435, 2018.
- [164] J. Yang *et al.*, "Wearable Temperature Sensor Based on Graphene Nanowalls," *RSC Adv.*, vol. 5, 2015.
- [165] L. Wang, R. Zhu, and G. Li, "Temperature and Strain Compensation for Flexible Sensors Based on Thermosensation," *ACS Applied Materials & Interfaces*, vol. 12, no. 1, pp. 1953-1961, 2020.
- [166] F. Zhang, Y. Zang, D. Huang, C.-a. Di, and D. Zhu, "Flexible and Self-Powered Temperature-Pressure Dual-Parameter Sensors Using Microstructure-Frame-Supported Organic Thermoelectric Materials," *Nature Communications*, vol. 6, no. 1, p. 8356, 2015.

- [167] P. Lugoda *et al.*, "Flexible Temperature Sensor Integration into E-Textiles Using Different Industrial Yarn Fabrication Processes," *Sensors*, vol. 20, no. 1, 2020.
- [168] K. Takei, W. Honda, S. Harada, T. Arie, and S. Akita, "Toward Flexible and Wearable Human-Interactive Health-Monitoring Devices," *Advanced Healthcare Materials*, vol. 4, no. 4, pp. 487-500, 2015.
- [169] T. Yokota *et al.*, "Ultraflexible, Large-Area, Physiological Temperature Sensors for Multipoint Measurements," *Proceedings of the National Academy of Sciences*, vol. 112, no. 47, pp. 14533-14538, 2015.
- [170] V. S. Turkani *et al.*, "Nickel Based Rtd Fabricated Via Additive Screen Printing Process for Flexible Electronics," *IEEE Access*, vol. 7, pp. 37518-37527, 2019.
- [171] M. D. Dankoco, G. Y. Tesfay, E. Benevent, and M. Bendahan, "Temperature Sensor Realized by Inkjet Printing Process on Flexible Substrate," *Materials Science and Engineering: B*, vol. 205, pp. 1-5, 2016.
- [172] Y. Moser and M. A. M. Gijs, "Miniaturised Flexible Temperature Sensor," presented at the TRANSDUCERS 2007 - 2007 International Solid-State Sensors, Actuators and Microsystems Conference, 10-14 June 2007, 2007.
- [173] Y. Chen, B. Lu, Y. Chen, and X. Feng, "Breathable and Stretchable Temperature Sensors Inspired by Skin," *Scientific Reports*, vol. 5, no. 1, p. 11505, 2015.
- [174] S. Ali, A. Hassan, J. Bae, C. H. Lee, and J. Kim, "All-Printed Differential Temperature Sensor for the Compensation of Bending Effects," *Langmuir*, vol. 32, no. 44, pp. 11432-11439, 2016.
- [175] S. Khan, L. Lorenzelli, and R. S. Dahiya, "Technologies for Printing Sensors and Electronics over Large Flexible Substrates: A Review," *IEEE Sensors Journal*, vol. 15, no. 6, pp. 3164-3185, 2015.
- [176] M. Ahmed, M. M. Chitteboyina, D. P. Butler, and Z. Celik-Butler, "Temperature Sensor in a Flexible Substrate," *IEEE Sensors Journal*, vol. 12, no. 5, pp. 864-869, 2012.

- [177] J. Bang *et al.*, "Highly Sensitive Temperature Sensor: Ligand-Treated Ag Nanocrystal Thin Films on Pdms with Thermal Expansion Strategy," *Advanced Functional Materials*, vol. 29, no. 32, p. 1903047, 2019.
- [178] H.-S. Chuang and S. Wereley, "Design, Fabrication and Characterization of a Conducting Pdms for Microheaters and Temperature Sensors," *Journal of Micromechanics and Microengineering*, vol. 19, no. 4, p. 045010, 2009.
- [179] W.-P. Shih *et al.*, "Flexible Temperature Sensor Array Based on a Graphite-Polydimethylsiloxane Composite," *Sensors*, vol. 10, no. 4, pp. 3597-3610, 2010.
- [180] Z. Cao *et al.*, "Highly Flexible and Sensitive Temperature Sensors Based on Ti₃C₂tx (Mxene) for Electronic Skin," *Journal of Materials Chemistry A*, vol. 7, no. 44, pp. 25314-25323, 2019.
- [181] G. Rajan *et al.*, "Low Operating Voltage Carbon–Graphene Hybrid E-Textile for Temperature Sensing," *ACS Applied Materials & Interfaces*, vol. 12, no. 26, pp. 29861-29867, 2020.
- [182] Q. Li, L.-N. Zhang, X.-M. Tao, and X. Ding, "Review of Flexible Temperature Sensing Networks for Wearable Physiological Monitoring," *Advanced Healthcare Materials*, vol. 6, no. 12, p. 1601371, 2017.
- [183] R. He, H. Liu, Y. Niu, H. Zhang, G. M. Genin, and F. Xu, "Flexible Miniaturized Sensor Technologies for Long-Term Physiological Monitoring," *npj Flexible Electronics*, vol. 6, no. 1, p. 20, 2022.
- [184] A. K. Bose *et al.*, "Screen-Printed Strain Gauge for Micro-Strain Detection Applications," *IEEE Sensors Journal*, vol. 20, no. 21, pp. 12652-12660, 2020.
- [185] Z. Liu *et al.*, "A Thin-Film Temperature Sensor Based on a Flexible Electrode and Substrate," *Microsystems & Nanoengineering*, vol. 7, no. 1, p. 42, 2021.